Development of a Catalyst for Flue Gas Cleaning in Biomass Power Plants

Entwicklung eines Katalysators zur Abgasreinigung für Biomassekraftwerke

Der Technischen Fakultät

der Friedrich-Alexander -Universität

Erlangen-Nürnberg

zur

Erlangung des Doktorgrades Dr.- Ing.

vorgelegt von

Giovanny Andres Mateus Batanero

aus Chia, Kolumbien

Als Dissertation genehmigt

von der Technischen Fakultät

der Friedrich-Alexander-Universität Erlangen Nürnberg

Tag der mündlichen Prüfung: 7.10.2019

Vorsitzender des Promotionsorgans: Prof. Dr.-Ing. habil. Andreas Paul Fröba

Gutachter: **Prof. Dr. Hornung**

   **Prof. Dr. Hartmann**

Abstract

The integration of biomass based fuels is leading the way towards reliable energy supplies, but still high emission values are observed during the energy conversion (NO_x, SO_x, H_3PO_4 and soot), due to the Nitrogen, Sulphur and Phosphate contained in biomass [1]. Additionally, mineral content and heterogeneity of biofuels lead to high concentration of particles in exhaust gases, which can reach up to 60 mg/Nm^3 [2]. To address this problem, robust exhaust gas treatments can be installed at firing systems, however for small and medium systems (<10 MW) economical and fitted solutions are still needed [3].

Previous approaches are based on catalytic coating of porous bodies, i.e. [4][5]. In this technique, the external surface of a filter body is coated with a catalytic solution. This method is also called impregnation [6]. Through this process, a particle filter and catalytic material are merged into one product. Although this technique has shown efficiencies of up to 80% at over 250°C in dusty conditions like biomass combustion, the impregnation method is limited by the porosity of the support [7].

On one hand, low porosity bodies efficiently retain particles, but at the same time this property limits the impregnation method because these bodies filter most of the catalytical particles. This inhibits the deposition of the catalyst in the internal bulky structure of the porous filter. On the other hand, supports with good porosity get easily coated, which also increases the amount of deposited catalyst [8]. However, these filters are clogged later under operational conditions. For instance, pores get plugged with dust particles, which increases the pressure drop and subsequently minimizes the catalytical effect [9].

An acceptable balance between porosity of the filter and activity of the catalyst calls for alternative fabrication methods. Besides, the active material should catalyze under dusty, wet and corrosive conditions. Moreover, other parameters such size, cost, mechanical stability and chemical resistance must be kept under the standard values [10]. Therefore, a new fabrication method for catalytic filters was developed and tested in this project to satisfy the requirement of small and medium firing plants, see figure below.
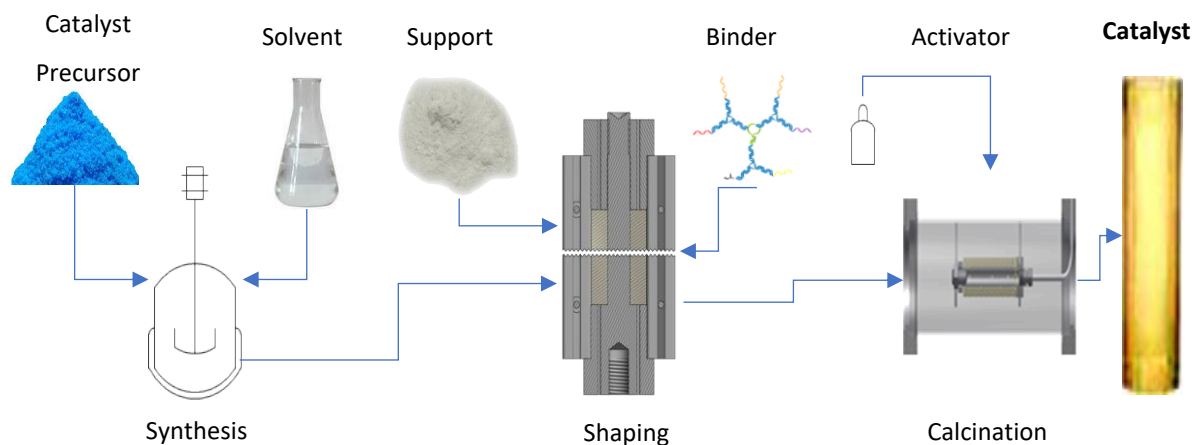
Figure. Overview Catalytic Filter Fabrication.

To achieve this, an organometallic compound based on copper was synthesized by a solvothermal process, see left side of previous figure. Stabilization of the active sites was achieved through addition of silicoaluminate precursors and an organic template as mesoporous structuring agent. This process encapsulated the catalytic material for upcoming steps. As illustrated in the middle part of the previous figure, integration of filter material and catalytic material was done by mixing and shaping the catalytic filter in a mold. Adjustment of the molding process and porosity were attained by addition of inorganic binder. Finally, the shaped body was calcinated and activated in a controlled atmosphere for the final operation in the SCR test stand.

Validation of the process was linked to the NOx reduction capacity of the catalyst. Therefore, adjustment in the formulation was done by analysis of the NO conversion, depending on temperature. Additionally, a particle filtration test was run on the catalytic filter in order to analyze the simultaneous performance during dust filtration and NOx conversion. Lastly, the optimal formulation was tested under real exhaust gas and characterized based on temperature and pressure.

Finally, to evaluate the synthesis, detailed spectroscopy measurements were implemented on the catalytic filter. By doing so, active centers and absorption sites of the catalyst were revealed by using several analytical techniques, such as STEM, XRD, TPR, TPO, EPR and NMR. Based on the analytical measurements, a catalytic mechanism is proposed.

List of contents

List of Figures

List of Schemes

List of Tables

Nomenclature

Symbol	Description	Unit
A	Hyperfine sppliting constant	[-]
$A_\parallel$	Hyperfine resonance	
$g_\parallel$	Parallel angular momentum of an electron	
$g_\perp$	Perpendicular angular momentum of an electron	
μ_i	Molar fraction of Species i	[-]
BAT	Best Available Techniques	
BImSchV	Bundes-Imissionsschutzverordnung	
CaO	Calcium oxide	
CeO_2	Ceria oxide	
CHP	Central heating unit power	
Cs_2O	Cesium oxide	
CTAB	Cetymethyl-Tetramethyl-Ammonium Bromide	
Cu_2O	Cuprous oxide	
CuO	Copper oxide	
CVD	Chemical vapor deposition	
De-NO_x	Reduction from nitrogen oxides	
DFT	Density functional theory	
DMF	Dimethyl formamide	
DMSO	Dimethyl sulfoxide	
DOC	Diesel oxidation catalyst	
DTA	Differential thermal analysis	
DTG	Differential thermogravimetric analysis	
E_a	Activation Energy	[J]
EDX	Energy dispersive X-Ray	
EPR	Electron paramagnetic resonance	
EPRI	Electrical Power Research Institute	
FAU	Zeolite based on faujasite framework	
FI	Volumetric Flow	[Liter/min]

HCN	Cyanide	
HC-SCR	NOx reduction by hydrocarbons	
HOMO	Higher occupied molecular orbital	
HPO_3	Phosphoric acid	
IC	Internal combustion	
k	Permeability	$[m^2]$
K_2O	Potassium oxide	
LNT	Lean NO_x storage trap	
LUMO	Lower unoccupied molecular orbital	
MgO	Magnesium oxide	
MO_2	Metal dioxide	
N_2	Nitrogen	
Na_2O	Sodium oxide	
Na_2SiO_3	Sodium silicate	
Na-Y	Sodium -Y zeolite	
NH_3	Ammonia	
NH_3-**SCR**	NOx reduction by ammonia	
NH_4NO_3	Ammonia nitrate	
NMR	Nuclear magnetic resonance	
NO	Nitrogen Oxide	
NO_2	Nitrogen dioxide	
NO_x	Nitrogen oxides	
O_2	Oxygen	
OSDA	Organic structural directing agent	
P	Pressure	[mBar]
P123	Pluronic 123	
P_2O_5	Potassium pentoxide	
PCDD	Polychlorinated dibenzodioxins	
PCDF	Polychlorinated dibenzofurans	
pKa	Logarithm of acid dissociation constant	
PM	Particle matter	

ppm	Parts per million	
SCR	Selective catalytic Reduction	
SN_2	Bimolecular reaction involving two steps	
STEM	Scanning transmission electron microscopy	
T	Temperature	[°C]
TEOS	Tetraethyl orthosilicate	
TiO_2	Titanium dioxide	
$T_{ligth\text{-}off}$	Temperature of light off	
TPD	Temperature programmed desorption	
TPO	Temperature programmed oxidation	
TPR	Temperature programmed reduction	
u	Face velocity	[m/s]
V_2O_5	Vanadium pentoxide	
VOC's	Volatile Organic Compounds	
XRD	X-Ray diffraction	
ZSM-5	Zeolite socony mobil-5	
β	Temperature Coefficient	[-]
ε	Porosity	[-]
ϴ	Coverage	[-]

1   Emission Control of Biofuel based Combustion

Due to environmental issues of the fossil fuels, development of sustainable energy sources is contemplated as a key policy in the economic development of European countries. Biofuels are one of the most promising renewable energy sources, because of their neutral impact on the environment [11]. In consequence, the use of biological residues to generate clean energy shows a smart and ecological way to close the sustainable energy cycle in countries such as Germany [12]. For instance, different approaches for local energy supply at biomass firing systems are currently being developed, whereby biomass residues could be incorporated into the energy generation process.

1.1   Emissions from Biomass Firing Processes

During the oxidation of biofuel, several oxidation mechanisms and intermediate molecules can be identified. Because biomass constituents already have oxygen functionalities, the emissions during combustion are difficult to predict. However, for the common case (i.e. wood) three main constituents can be formulated, Cellulose, Hemicellulose and Lignin. By following the thermal decomposition of these compounds, monomers of glucose, furans, phenyl and aromatic rings have been found (see volatilization in figure 1-1) [13].
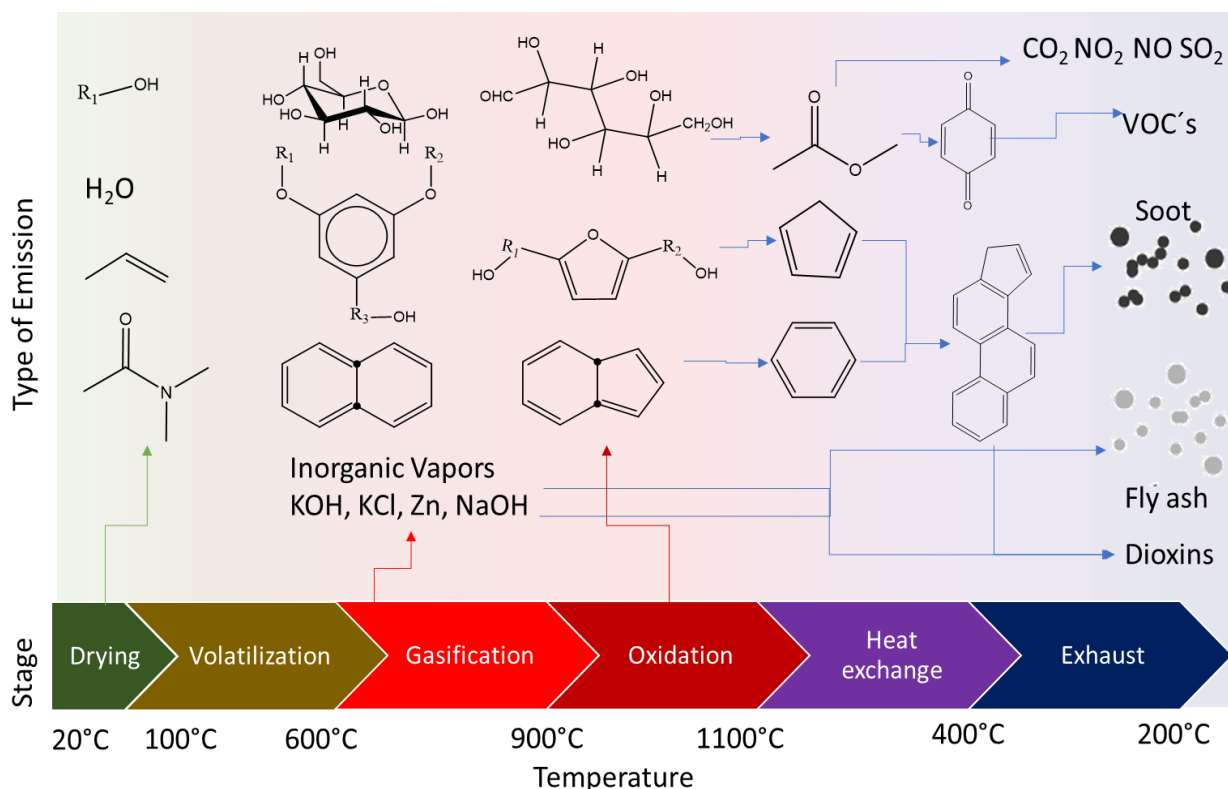
Figure 1-1. Pollutant Emission from Biomass Combustion. Diagram based on [13].

Through the increase of the temperature, emission of VOCs (Volatile Organic Compounds) with functionalities of aldehydes, ketones and esters can be traced [13]. Across the temperature increase, most of the compounds are reduced to CO_2, NO_2 and H_2O (see upper right hand corner in figure 1-1). Unfortunately, some compounds do not react, because of lack of temperature, residence time or oxygen concentration. These compounds are released as VOCs, when they don't react anymore downstream. Conversely, there are other compounds, which react afterwards in the heat exchanger and exhaust zone.

During the oxidation of the biomass, there is a vast generation of radicals from benzene and cyclopentadiene. These radicals can overcome the oxidation and the heat exchange zones, as observed in biomass firings [14]. Afterwards, these activated molecules react in the exhaust stream, creating bigger aromatic chains. This agglomeration process leads to soot formation [15].

1.1.1 Formation of VOCs

During the oxidation of Lignin and Cellulose, low molecular weight monomers (aldehydes, alcohols, ketones and esters) are released [16]. Because these compounds contain functional groups with oxygen atoms, their reactivity towards oxygen radicals is reduced at the flame zone. Hence, some aldehydes, carbonyls and polyesters don't react across the high temperature zone. Beyond the flame zone, hydrocarbons start to cool down at the heat exchanger, where some of the unreacted compounds stabilize on cyclic compounds such as furans, phenyls and cyclopentadienes [17].

1.1.2 Soot Formation

In a similar way as the VOCs, soot formation has its origins on unreacted organic monomers. As shown in figure 1-2, unreacted alkenes and alkynes form aromatic rings in the rich fuel zone. As an effect of the temperature drop in the exhaust line, aromatic rings and cyclopentadienes mostly agglomerate. This results in the formation of big polymeric aromatic rings, which grow enough to achieve micrometrical dimensions.

Some of the agglomerated aromatics precipitate in the solid residues as char, while others are light enough to be fluidized in the flue gas stream. Due to the appearance of this pollutant, some authors classify them as black carbon or unburned hydrocarbon [18], [19] and [20].
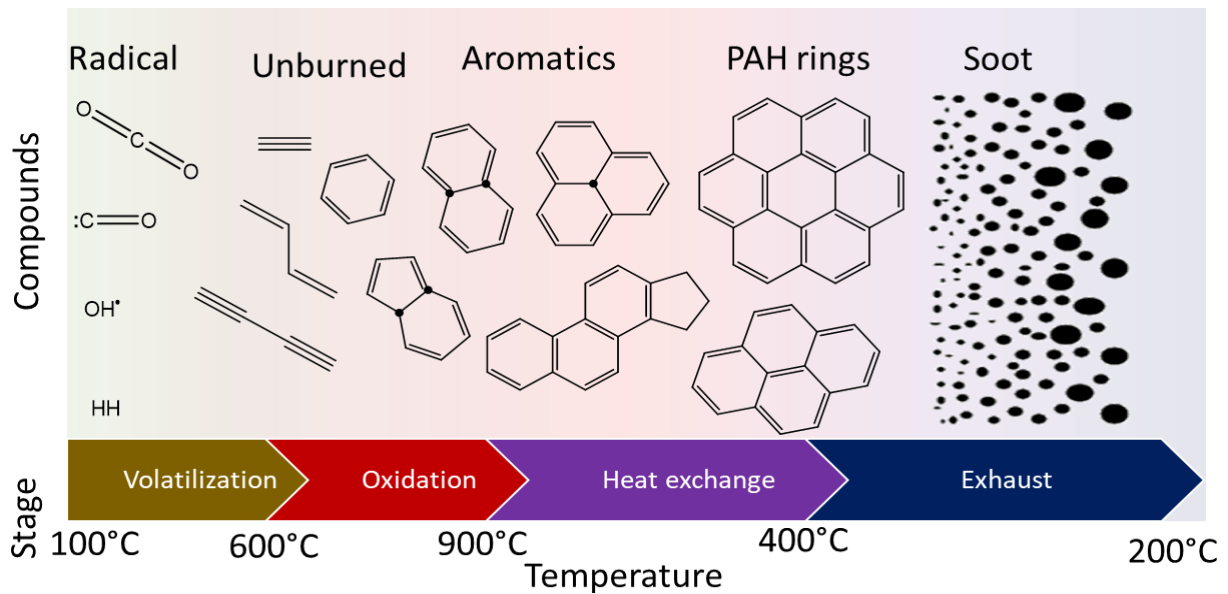
Figure 1-2. Soot Formation. Adapted from [21].

1.1.3   Fly Ash

In biomass, the inorganic content reaches up to 2% [22], because of the alkali elements, which are involved in the biological development. These inorganic compounds evaporate during the gasification phase, where they start to react with other halide species. Some of them react with halide species forming inorganic salts, which precipitate in the ash residue. On the other hand, others react with organic chains. This interaction forms low density particles, which remain volatile due to the turbulence in the combustion chamber.

Radical-anion species such as $\cdot CO^-$, $\cdot O^-$, SO_2^- and PO_3^- appear in the oxygen rich zone, also referred to as lean zone. In contact with organic vapor, these radicals become stable compounds. In consequence, organic salts such as carbonates and sulfates are formed in the oxygen rich zones. Later on, as the gases cool down, nucleation and agglomeration enhance the formation of fine particles. When these particles reach the exhaust gas system, they are called fly ash because of their volatility [23].
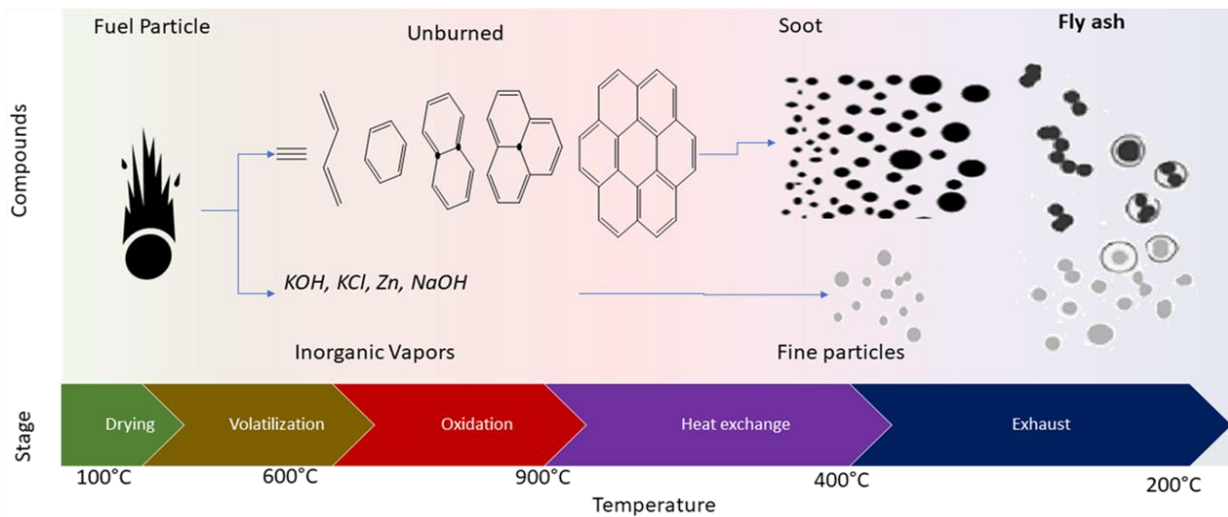
Figure 1-3. Fly Ash Formation. Adapted from [23].

1.1.4   Nitrogen Oxides Formation

Formation of VOCs, soot and fly ash can be strongly reduced by lean mixtures and high temperatures, where the excess of oxygen avoids the reformation of carbon-carbon bonds. However, at the same time, this oxygen excess promotes the formation of harmful oxides such as NO_2 and NO [24]. In the case of biomass, oxygen excess escalates NOx formation, due the nitrogen contained in the biomass. Therefore, NOx formation from biomass sources has been studied in recent years according to the feed material, as illustrated below [25].
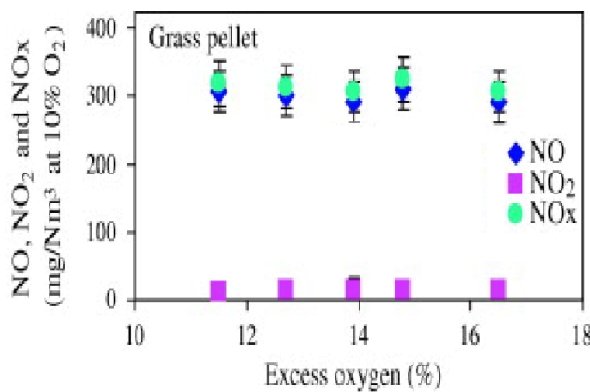
Figure 1-4. Emission of NOx at different O_2 Concentrations. Adapted from [26].
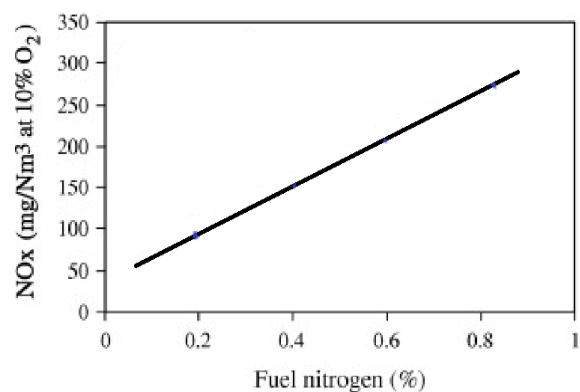
Figure 1-5. Influence of Nitrogen on Fuel at NOx Emission. Adapted from [26].

Commonly, NO_x formation is attributed to the direct reaction of oxygen with nitrogen at high temperatures. This is called Thermal NOx formation and it is one of three mechanisms of NOx formation identified nowadays. However, in biomass conversion the other two, Fuel Nitrogen and Prompt NO, account for almost the entire amount of NO emissions rather than the thermal mechanisms [27]. As the previous figure 1-4 and figure 1-5 illustrate, excess of oxygen doesn't

increase the NOx formation at defined conditions. In contrast, the nitrogen in the fuel has a direct effect on the NOx formation, because the bounded nitrogen eventually follows the oxidation pathways [28].

i.   *Thermal NOx Formation*

In this mechanism NOx is formed at a temperature of more than 1200°C, from the reaction of the nitrogen and oxygen in the air. As the temperature rises, more oxygen and nitrogen radicals are released, due to the entropy of the system. When these radicals meet other gas molecules, they form species such as nitrogen oxides following the reactions R 1.1 and R 1.2.

$$O^* + N_2 \leftrightarrow NO + N^* \qquad\qquad \textit{R 1.1}$$

$$N^* + O_2 \leftrightarrow NO + O^* \qquad\qquad \textit{R 1.2}$$

ii.   *Prompt NOx*

In rich conditions the combustion chamber contains higher concentration of fuel radicals, here represented as CH^*. These species can activate dinitrogen molecules, forming cyanide radicals (see reaction R 1.3). Subsequently, these species react with oxygen to form NO and a new fuel radical, as shown in R 1.4. The heterogeneity of the fuel and under stoichiometric combustion spots generate Prompt NOx [25]. However, biomass combustion is carried out at below 900°C under lean conditions. Therefore, contribution of Prompt NOx is expected to be minimal [29].

$$CH^* + N_2 \leftrightarrow HCN + N^* \qquad\qquad \textit{R 1.3}$$

$$HCN + O \leftrightarrow NO + CH^* \qquad\qquad \textit{R 1.4}$$

iii.   *Fuel NOx*

Biomass contains nitrogen in several structures, however the latter can be simplified to Polyamides, Proteins and N-heterocycles. Since each structure represents different organic nitrogen groups, NOx formation follows different routes in accordance to the nature of the biomass. Currently, accurate mechanisms for NOx formation from bounded nitrogen are still in the early stages.

To shed light on the N-Fuel mechanism, some authors have focused on the oxidation mechanism of representative nitrogen molecules in biomass [30]. From the studies of reaction routes of typical nitrogen groups, such as amines, amides, nitriles, pyridines and pyrroles, it

can be concluded that in combustion conditions, all of them can be simplified as amide groups. According to a recent study, nitrogen compounds in biomass can be simplified as amide chains. This simplifies the NOx formation mechanisms to amide oxidation routes, as shown in scheme 1-1 [31].
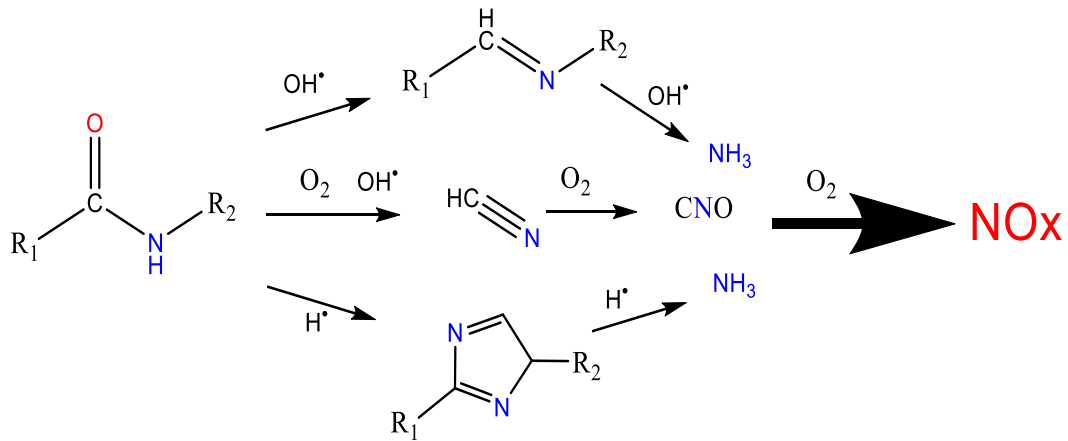
Scheme 1-1. Biofuel NOx formation.

Basically, there are three pathways, which are correlated to the oxygen and radical availability. In oxygen poor zones, fuel radical amides tend to form heterocyclic rings, which can be decomposed again when the temperature increases (see lower pathway in scheme 1-1). Conversely, as the upper part of the above scheme shows, high concentration of OH* radicals promote the formation of imides and nitriles from amides [32]. Just like heterocyclic rings, imides degrade to amines and cyanides with the increase of temperature.

Nitrogen compounds in biomass follow mostly the amine path shown in the center of the scheme. Briefly, carbon oxidation releases cyanide and amine compounds, which later oxidize to organic nitrates. Further increase of temperature and oxygen converts almost all the compounds to CO_2, NO, NO_2 and H_2O [33].

1.2   NOx Emission Control Strategies

Air quality control policies in Germany, such as 1st and 4th "Bundes-Imissionsschutzverodnung" (BImSchV), are recently being adjusted, in order to control the emission scenery of bioenergy systems [34]. This implies the development of new strategies for NOx abatement at emission sources. Additionally, to overcome this challenge, the European Union has defined a set of standard techniques in order to achieve low emission limits. In the document with the title BAT "Best Available Techniques", several techniques are carefully described in accordance to the typical emission of different industrial sectors [3].

By now, several strategies have been developed to reduce NOx emissions, which can be classified into two types. Methods to reduce the pollutant generation in the sources are named "Primary measures", while the methods to control the already generated pollutants are defined as "Secondary measures". Techniques of these two types, which relate to the biomass combustion, are shortly described below.

1.2.1   Primary Measures

On biomass combustion, the required excess of an oxidant also promotes the formation of NOx. This can be controlled primarily through a strategical distribution of the air and adequate oxygen fuel ratios. For instance, techniques such Air Staging or Low Oxygen Excess make use of this principle (see table 1-1). Despite its low NOx efficient values, these techniques show advantages for already operative systems, due to their low investment cost and quick installation [35] and [36].

Table 1-1. Comparison of Primary Techniques for NOx Reduction

Technique	Description	Advantages	Disadvantages	NO$_x$ Reduction
Low Excess Air	Reduces oxygen availability	Easy modification Useful for retrofitting	Low NO$_x$ reduction Incompletely burned out	10-44%
Air Staging	Internally staged combustion	Low operating cost	Moderately high capacity costs	25-35%
Flue Gas Recirculation	<30% flue gas recirculated	High NO$_x$ reduction	High energy consumption Flame instability	20-50%
Fuel Reburning	Inject fuel to react with NO$_x$	Moderate cost Moderate NO$_x$ removal	Extends residence time Incomplete combustion	50-60%
Oxy-fuel	Uses pure oxygen to oxidize	High NOx reduction	Equipment to handle oxygen	70-80%

Efficiency can be increased by recirculation of either flue gas or unburned fuel. These techniques are suitable for systems with a long residence time. Due to the fact that the recirculation system requires time and energy to bring back the unburned feed, systems with larger residence time show tolerable disturbances [37]. Unfortunately, the cost and complexity

of the recirculation circuit makes the inclusion of these technologies in old or small facilities difficult [38] [39].

Another more elaborate technique relies on the absence of nitrogen during the oxidation. This technique strictly warranties no NOx emissions at all, as long as the fuel is nitrogen free (i.e. rocket fuels). This technique radically eliminates the formation of NOx at the entire temperature range; however, its cost limits its application in commercial systems [40].

1.2.2 Secondary Measures

In many industrial applications, the energy conversion must be done at a limited space like automobiles or electricity generators. Air staging, also referred to as recirculation of flue gases, requires plenty of space and isolation. Hence for industrial applications, NOx emission should be reduced downstream by compacted methods, where a reduction agent is required to convert nitrogen oxides to harmless nitrogen gas and water.

In the case of biomass combustion, NOx emission values vary between 100 and 1000 mg/m^3 in relation to the feedstock, see figure 1-6. Although primary measures can be implemented to satisfy the norm, this doesn't guarantee the fulfillment of the emission limit. In consequence, for usual biomass feedstock such as wood, a secondary measure is highly recommended, because of its wide range of nitrogen content. Hence, SCR technologies are chosen for NOx control because they work effectively in a wide spectrum of biofuels, as shown below.
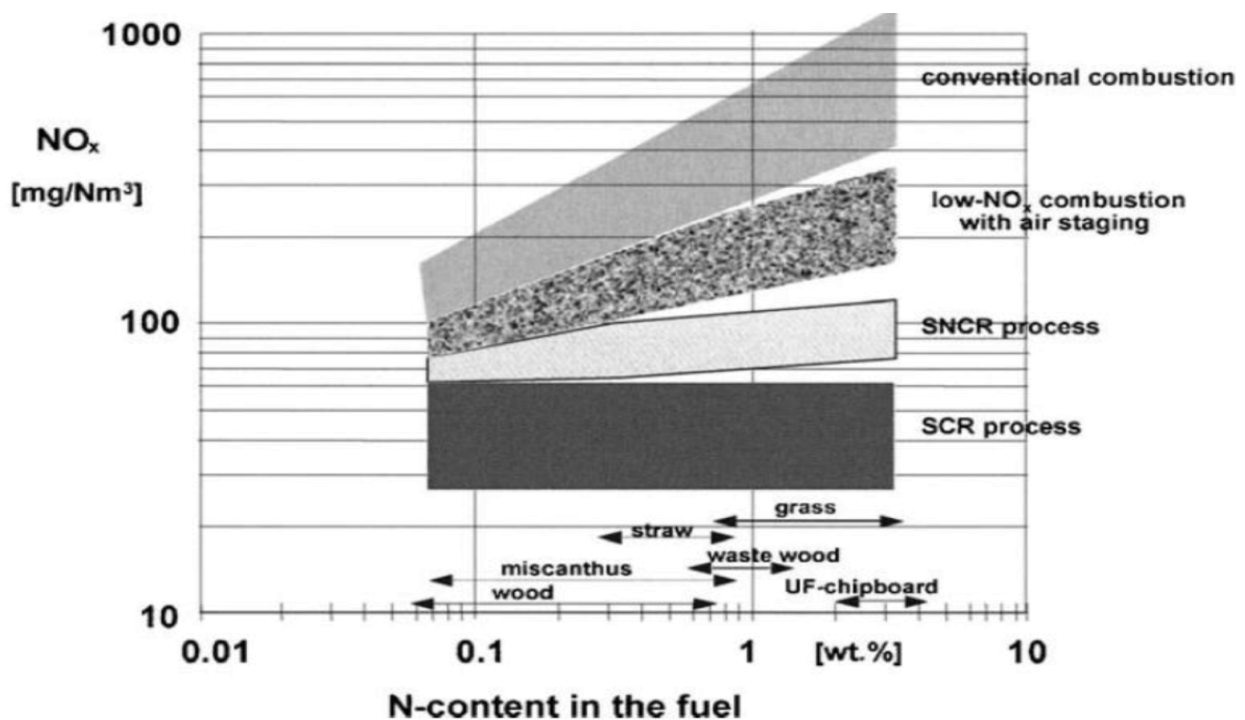
Figure 1-6. NOx Reduction Emission of Biofuels. [41].

1.2.3 Selective Catalytic Reduction

In recent years after the lowering of the NOx emission limits, the selective catalytic reduction (Selective Catalytic Reduction) SCR has become the best available technique for NOx control [42]. In this technique a reductant, mostly ammonia, is injected into the flue gas stream. To perform the reduction, a catalyst proves active areas, where the ammonia and the NOx gas react selectively. The reactions R 1.5 and R 1.6 condense the ideal global SCR mechanism, where nitrogen oxides are reduced with ammonia to produce nitrogen gas, without any interference of other gases.

$$4NH_3 + 6NO \rightarrow 5N_2 + 6H_2O \qquad\qquad \textit{R 1.5}$$

$$8NH_3 + 6NO_2 \rightarrow 7N_2 + 12H_2O \qquad\qquad \textit{R 1.6}$$

Although the reaction is selective to nitrogen oxides, in practice it is important to account for ammonia oxidation [43]. Excess of ammonia works against the NO reduction, because it can be oxidized to nitrate compounds, as indicated in reaction R 1.7. Thus, the injection of ammonia must be continuously controlled, in order to avoid additional formation of NOx or nitrous oxides [44].

$$4NH_3 + 5O_2 \leftrightarrow 4NO + 6H_2O \qquad\qquad \textit{R 1.7}$$

$$2NH_3 + 2O_2 \leftrightarrow N_2O + 3H_2O \qquad\qquad \textit{R 1.8}$$

1.2.4 De-NOx Catalyst

At temperatures below 400°C, these reactions need to be catalyzed, although they are thermodynamically favorable [45], [46]. Therefore, in a SCR system, the reactions R 1.5, R 1.6, R 1.7, R 1.8 and their possible combinations are carried out on the surface of the catalyst. Hence, the material of the catalyst plays the main role in the SCR system, because its surfaces determine the activity and selectivity of the entire system.

As illustrated in figure 1-7, the reduction of nitrogen oxide starts when the ammonia is activated at the surface of the catalyst. This indicates that materials with marked absorption towards ammonia are good candidates for SCR catalysts, because the remaining reaction steps are exothermic [47].
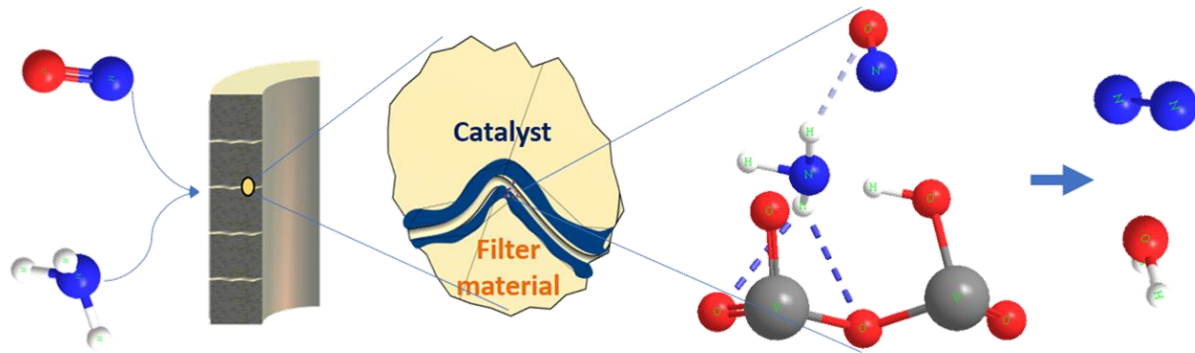
Figure 1-7. Activation of Ammonia on a V$_2$O$_5$ catalyst.

Transition metal oxides such as Vanadium pentoxides (V$_2$O$_5$) are well known to catalyze ammonia reactions. At the right side of the previous figure an active center of V$_2$O$_5$ activates an ammonium ion, which consequently reacts selectively with NO, forming an intermediate azido bond. Afterwards, the ammonium intermediate is dehydrated by NO to form N$_2$, water and other intermediate species [48].

1.3   Filtration of Particles Matter

Due to the high volume of particles in biomass combustion, the removal of PM (particle matter) is mainly performed by cyclones, electrostatic precipitators, scrubbers and filters [49]. Particularly in dusty environments, particle filters show the best efficiency-cost ratio, see figure 1-8.
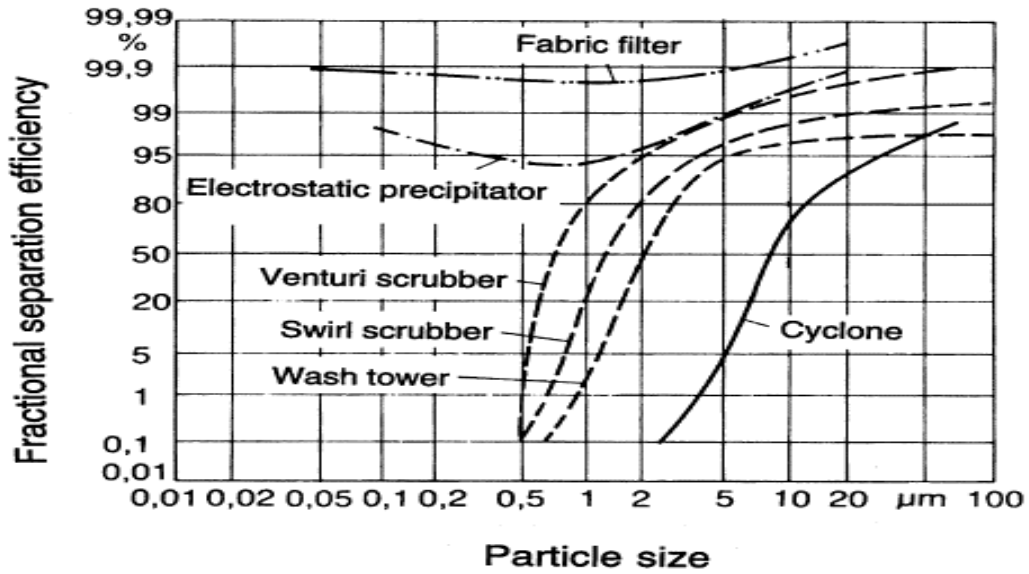
Figure 1-8. Particle Collection Efficiency. [50].

Filters use a simple physical size principle; a porous barrier retains bigger particles than the pore diameter size. As a consequence, smaller particles and gases can pass across the porous material. This principle supplies high efficiency and reliability for filtering of dusty flue gases, because the selectivity depends mainly on the characteristic of the material rather than the kinetics of the gas stream.
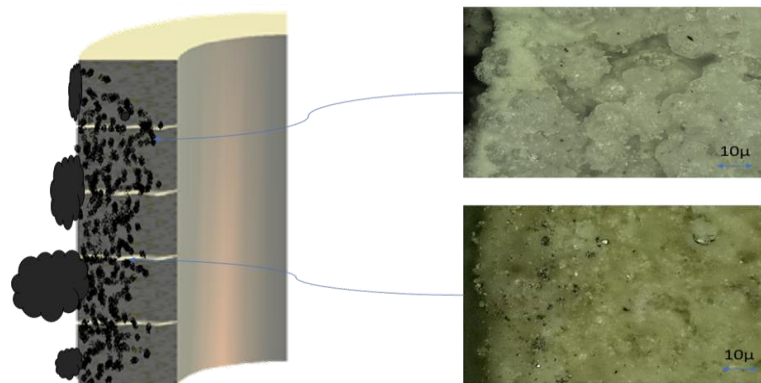
Figure 1-9. Particle Filtration.

Left: Intrusion of particles in Filter. Right: transversal view of a catalytic filter. Right up: clean pores, right down: Filtered dust particles.

Although the small porous size stands for high efficiency, it also causes early plugging of the filter in dusty environments. Integration of filters with self-cleaning systems avoids this issue. These systems consist of several filters, a pressure tank and a collector unit (see figure 1-10).

In this structure, the accumulated dust is removed by periodical air pulses, which come from a pressure tank. The pressured air pulse flows from the interior to the outside area of the filter, thus swelling the dust particles attached to the filter, see right filter in figure 1-10. The system can be regenerated continuously, when the cleaning sequence is programmed alternatively. At the bottom of the system, an additional collection bucket stores the precipitated material.
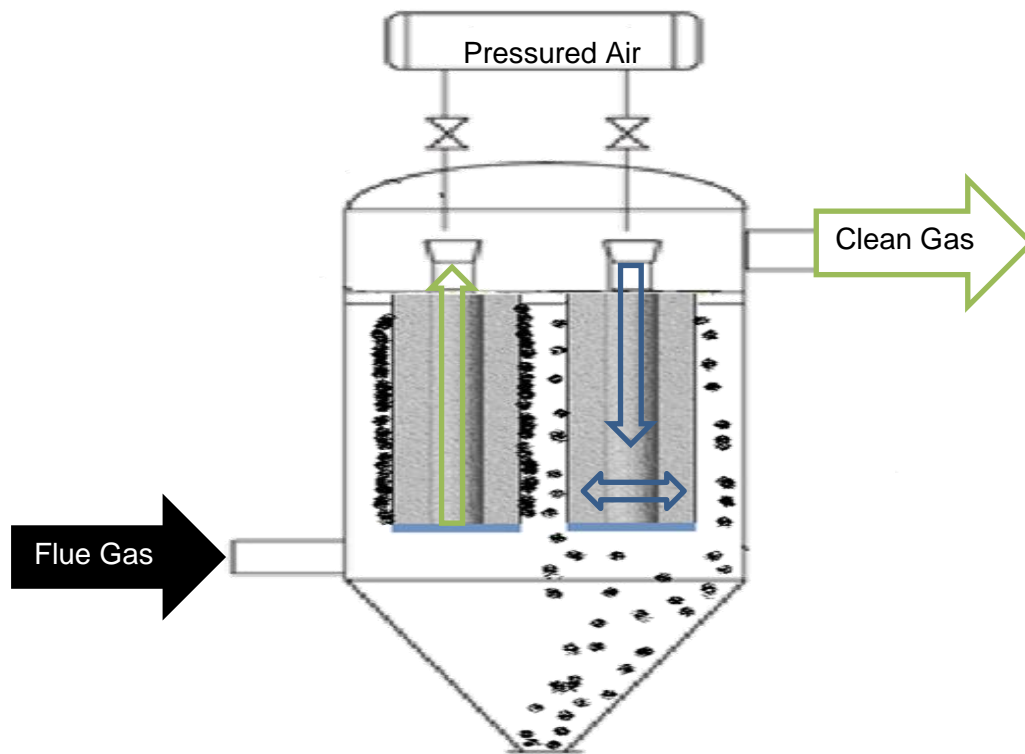
Figure 1-10. Filter System.
Green arrow: cleaning cycle. Blue arrows: filter regeneration.

1.4   Combined Particle Filtering and NOx Catalysis

Catalytic materials for SCR need to have large porosity for higher absorption capacity of ammonia and NOx. Conversely, filter materials need high porosity to transport the gas phases during filtration. Since porosity is a common parameter, a combination of a particle filter with catalytical properties seems plausible for SCR systems. Therefore, for industrial application, a combined implementation would notably reduce cost and maintenance of the SCR system [4].

1.4.1   Catalytically Activated Filter

Porous filters have recently been activated for NOx and tar reduction, as a consequence of the strengthening of the emission limits on small and medium firing systems [51][52][53]. In these

studies, porous filter materials were coated with a dissolved catalyst. After saturation of the support, the filters were dried and calcinated for removal of the solvent [5].

Activation of filter support shows promising results, when dust and vapor concentrations are below the condensation point. However, in comparison with the separated units, the combined catalytic filters generally showed less activity due to the synergy interaction of the support, the binder and the catalyst. Moreover, decrease in the permeability was also observed. This indicates that after the coating of the catalyst, the porosity is notably reduced, because the catalyst sits preferentially on the small channels. Thus, less channels are available, which accounts for high pressures on the filter [52].

1.4.2   Soot and NOx Filter

On mobile applications, additional place is required for the SCR reaction and the urea storage. These are factors which support the necessity for integrated and compact flue gas cleaning systems. The automobile industry has been taking actions concerning this issue. Therefore, a combination of a soot filter and a NOx catalyst has been successfully fabricated and tested, which indicates that substantial miniaturization of catalytic filters is possible [54]. Figure 1-11 illustrates the frontal view of the catalyst, where 80 stands for the filter, 81 for the coated side and 82 for the soot filtration side.
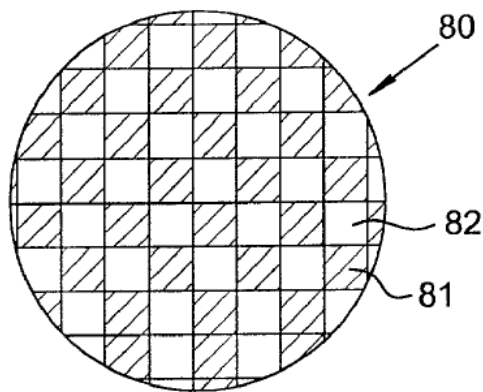
Figure 1-11. Frontal View Catalytic Filter [54].
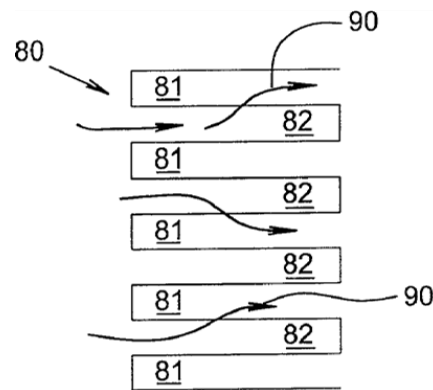
Figure 1-12. Section View [54].

In this example, the catalytic filter was achieved through a coating on one side of the filter´s surfaces (81). In that way, the non-coated surface filters soot (82), while the coated one catalyzes NOx. For the sake of better insight, figure 1-11 and figure 1-13 illustrate a frontal and a section view of this catalytic filter. When a flue gas stream (90) flows, it is firstly dedusted on the surface (82), then at the side (81) the catalyst converts NOx with CO to form N_2 and CO_2.
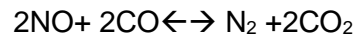
$$2NO + 2CO \leftrightarrow N_2 + 2CO_2 \qquad \textbf{\textit{R 1.9}}$$

While this concept works partially on some gasoline cars, there are currently several issues related to plugging, salts formation and deactivation of the catalyst, which need to be addressed. Nevertheless, this advance in size serves as a reliable base for the development of similar solutions in the field of power plants.

1.5 Motivation

Though the SCR technique for reduction of NOx has been established as the best available technique, the integration of a particle filter and De-NOx catalyst requires further improvements. This is visible in biomass combustion, where high dust and humidity concentration is generated. Moreover, there are other practical factors, which limit the application of these technologies in small and medium firing systems, such as cost, size and stability.

1.5.1 Problem Statement

Since biofuels show a marked heterogeneity, especially in biomass firing systems, the integration of particle filter and catalyst expose new technical challenges. Moreover, identification of new harmful pollutants from these processes demands specialized flue gas cleaning systems [55].

i.   Cost of the Flue Gas cleaning System

For incinerators and furnaces of biogenic residues, which operate occasionally, the capital and operation cost of the aftertreatment system accounts for at least 26% of the total investment [56]. Basically, the problem starts at the combustion step itself. Compact and coordinated chemical compounds are oxidized, which leads to formation of pollutants, such as Carbon Monoxide (CO), Volatile Organic Compounds (VOCs), Nitrogen Oxides (NOx), Sulfates (SOx), Phosphoesters (PO_4^{3-}), Dioxins (PCDD/F), to mention just the most common ones [13]. At this point, these compounds could be up to 1000 times bigger in volume than their original chemical source. For this reason, the exhaust cleaning system has a size of up to 100 times the size of the combustion chamber [57]. This technical issue demands plenty of place and infrastructure to keep the contaminated gases enclosed during their treatment.

Figure 1-13. Clean Harbor Waste Incinerator. Adapted from [58].

1)   *Rotary Kiln. 2) Spray drier. 3) First baghouse. 4) Second Baghouse. 5) SCR and stack.*

ii.   Size of the SCR-Catalyst

The size of the catalyst doesn't only depend on the activity and efficiency, but it also depends on the pressure at the input. Low pressure flows require a catalyst with low resistance, in which flue gas can pass through the catalyst. Hence in systems with low operation pressure, such as furnaces, the catalyst must avoid losses due to friction.

Figure 1-14. SCR Honeycomb [59].

Figure 1-15. De-NOx System [58].

To achieve this, honeycombs with straight channels are arranged in rectangular cassettes, as figure 1-14 illustrates. Then these cassettes are stocked in big structures for docking at exhaust gas treatment facilities. To accomplish NOx requirements, industries need to use

oversized catalyst systems to cope with different emission scenarios. This leads to an enormous De-NOx system comparable with the size of the stack, see figure 1-15.

iii.   Poisoning

Poisoning of the catalyst has strong effects on the operating system, because reactivation, also known as regeneration of the catalyst, is time and cost demanding. Therefore there are several studies attempting to understand the poisoning mechanism [60][61]. After detailed studies of SCR catalysts, two main causes have been identified. On the one hand, halogen compounds, such as SO_2, PO_3 and HCl in the flue gas, deactivate the catalyst by reacting with the active center, to form more stable compounds. On the other hand, alkali compounds, such as K_2O, Cs_2O, Na_2O, CaO, P_2O_5, react on the active center of the catalyst and then occupy the active sides. This is evident at low temperatures, when these Alkali crystallize and block the pores of the catalyst as depicted in figure 1-16 [62].

iv.   Plugging

There are several sources of plugging, also called fouling or clogging, depending on the porous geometry. In a dust-free flow gas, clogging comes from the growth of mineral salts or oxides in the pores. As previously mentioned, chemical poisons sit on active centers and grow until the pore is clogged.
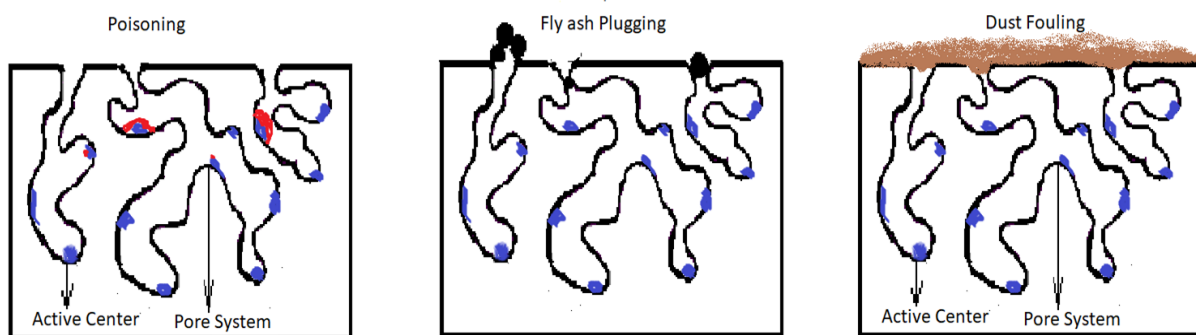
Figure 1-16. Deactivation Mechanism.

During the plugging process, fly ash or soot particles settle down on the entrance of the pores (see center graph of figure 1-16). On these sites particles find mechanical stability against the gas flow, therefore they occupy these spots endlessly. When temperature drops, either fly ash or soot crystallize in the pores, leading to plugging.

In biomass flue gases, the amount of fly ash and soot can be considerably high, so that plugging of internal pores is not observed. Even worse, the particles agglomerate on the

external surface, which inhibits any catalytical activity, see right side in figure 1-16. Not only does this affect the efficiency of the catalyst, but also the permeability of the filter, because the channels are continuously narrowed (right-hand graph of figure 1-16).

v.   *Catalyst Fabrication*

Deposition methods (coating, impregnation) are heavily used in the industry, because of their simplicity and commercial flexibility. In this method, the support and the catalyst can be manufactured differently, which results in commercial benefits for handling big stocks. However, these methods lack in efficiency, because the deposition methods depend on the diffusion forces. These diffusion flows are directly linked to the concentrations at both sides. Therefore, it is necessary to have higher catalyst concentration in the mixture to have a representative catalyst deposition at the support. In consequence, this technique always has big residues of the used catalyst, because at some point the support is saturated and the deposition stops [63][64].

In practical terms, the residues could be up to 80% of the catalyst, which requires a noticeable amount of additional work in the process. Some processes can reuse these residues in a serial production of filters, however the nature of the process will always have a residual quantity and an uneven catalyst distribution. These catalytical residues represent serious problems in the process, not only due to the material loss but also to the costly waste management of these hazardous residues [65].

1.6   Objectives

These previous issues on SCR catalysis motivate the development of a compact, efficient and reliable catalytic filter. Hence a catalytic filter was developed as a complementary solution for small and medium biomass firing systems. That catalytic filter is expected to have a small size and affordable cost, both of which make it appropriate for several firing or thermal plants. This aim sets the objectives of this doctoral thesis as follows.

1.6.1   Principal Objective

The main objective of this work is to study and plan the fabrication of a catalytic filter, which can simultaneously perform particle filtration and catalytic reduction of NOx from a flue gas stream. To achieve this goal, the following objectives were gradually accomplished throughout this work.
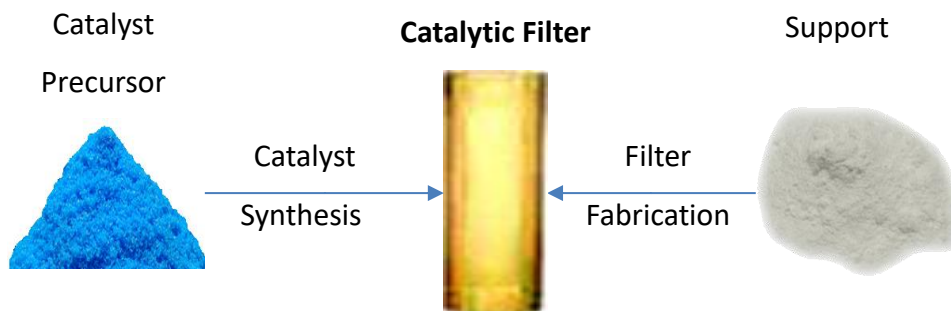
Figure 1-17. Catalytic Filter Fabrication.

1.6.2   Milestones

To achieve this goal, seven milestones were defined for the planning and scheduling of related tasks in this project:

- Developing a porous structure as a filter material, which can be catalytically activated
- Synthesis of the catalytic material for the integration in the filter
- Fabrication process for the coupling between filter and catalytic material
- Characterization of the material
- Testing of the integrated catalytic filter
- Analysis of the results
- Study of the material structure

The complexity of the material used during the development of the catalyst requires an exhaustive analysis and characterization. Thanks to this study, it is possible to find the

determining parameters for upcoming studies. Therefore, characterization, analysis and mechanism elucidation are further goals of this work.

1.7 Methodology

Since the main goal of this work includes several points, a variety of methodologies is applied to achieve those. For instance, the three first objectives use standard material synthesis techniques. The sol-gel technique, in combination with calcination, facilitates the fabrication of porous structures, which are required for the filter. Moreover, chemical synthesis by precipitation, impregnation and a solvothermal process enable the coordination and stabilization of the catalytic substances. A detailed description of the synthesis method will be given in chapter 3.

1.7.1 Catalytic Filter Fabrication

The fabrication process can be divided into three steps. Firstly, the active catalyst material is synthesized by use of organometallic synthesis techniques. Through this technique, the catalyst centers are chemically coordinated, which generates properties, such as activity and selectivity. Thus, a metastable catalyst substance is attained, which serves as a core of the catalytic filter afterwards.

In the second step, the catalyst is integrated with the filter material. On the one hand, the catalytic substance is dissolved to achieve higher distribution. On the other hand, the support material is chemically treated to create the anchoring points, where a binder will bind the catalyst. Next, in accordance to the technique, the diluted catalyst reacts with the binder. After mixing, the catalyst settles at the support by a solvothermal technique. In this step, the geometry and porosity of the catalytic filter are also defined by molding a ceramic structure.

Finally, the molded body is thermally treated. The calcination process removes excess of solvent and binder. Additionally, absorption properties are adjusted by modification of the calcination atmosphere. Further details are disclosed in chapter 3.

1.7.2 Catalyst Testing

To validate the operability of the catalyst at real conditions, a catalyst test was set up as shown in figure 1-18. On the left top a CHP motor is fed with modified fuel to generate exaggerated emission values of NO_x, SO_x and VOCs. The measurements are done online by an infrared Gas Analyzer (see bottom left), which works in combination with a valve system. Through the oriented operation of the reactor (middle right), the valves and the gas analyzer, NO_x, SO_x, and CO are measured. Conversion performance vs. the temperature and reduction agent are

evaluated by changing the heater configuration on the reactor and the feeding rate at the ammonia controller (top right). The test specifications were set in accordance to the standard protocol from EPRI institute (Electrical Power Research Institute), which is recommended for automotive catalyst testing [66]. This test is explained in detail in chapter 4.
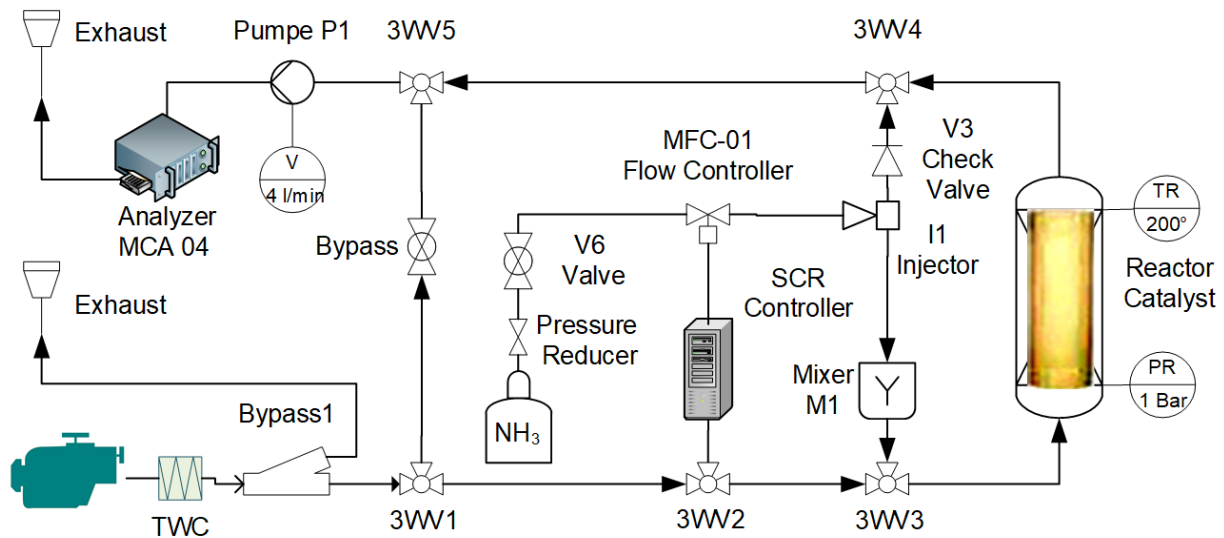
Figure 1-18. Flue Gas Cleaning Test.

1.7.3   Catalyst Characterization

The material characterization requires more elaborated spectroscopy in order to figure out the interaction between the material and the flue gases.   A first approach is gained by implementation of the absorption experiment. Among the most useful were TPR (Temperature Programmed Reduction) and TPO (Temperature Programed Oxidation), which react on the surface of the catalyst with reductant and oxidative agents, such as NH_3 and NO [67][38].

Additionally, NMR (Nuclear Magnetic Resonance) and EPR (Electron Paramagnetic Resonance) techniques were implemented to explore the material structures and the coordination of the active material (copper ions) in the filter structure [68], [69]. Further analyses of the catalyst are explained in chapter 6.

2   Design of Catalytic Filters

Due to the growing environmental consciousness around the world, the fabrication methods for filtering pollutants has been on the rise as well. In the field of catalytic filters, the most common in the automotive industry are the impregnated branch because of its simplicity. When this method is used, the catalyst and the support are treated separately, then the active catalyst is coated on the support [70]. As figure 2-1 shows, the availability for filter coating methods has increased by almost six times over the last 20 years [71]. A wide range of methods from practical wash coating, sol-gel, Chemical or Physical Vapor Deposition (CVD PVD), electrostatical absorption, flame coating as well as sophisticated plasma sputtering, among other techniques, show the importance of efficient and economical catalytic filters these days [72], [73], [74], [75].
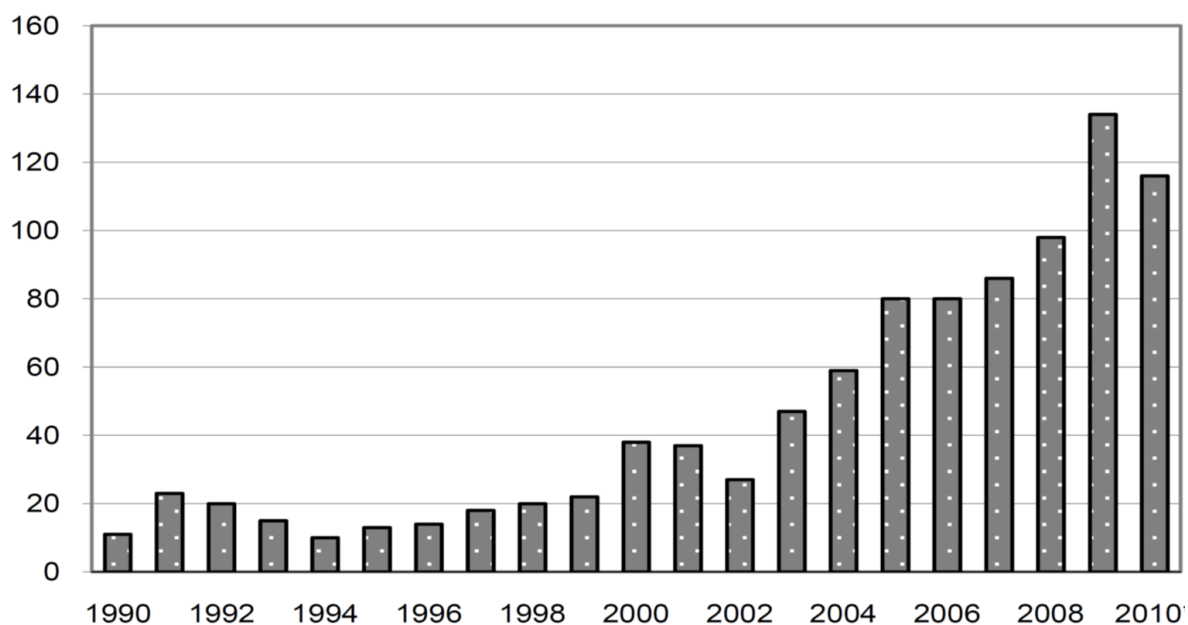
Figure 2-1. Total Number of Patents Publication on Catalytic Coating from the year 1990 until 2010. [71]

The next part of the chapter explains in detail the techniques, which have to be implemented in catalytic filter development. Three subchapters briefly display the theory and standard techniques needed for filter casting, catalyst synthesis and catalytic filter fabrication.

2.1   Fabrication of the Filter

In the field of catalysis, the filter is considered the support, on which the catalyst is deposited. Additionally to housing the catalyst, the support also influences the mass transfer and charge distribution along the catalyst. Recently, this fact has influenced the fabrication of supports,

also referred to as monoliths, honeycombs, or cordierites by other authors. The first supports in catalysis consisted of small pellets, which supply a specifically wide surface [76]. With the implementation of the auto converter, the well-known honeycomb - a 2D structure - invaded the automotive market, because its extrudate channels have the low-pressure drop needed for this application.

Particle filters can be summarized as porous bodies with a porous distribution range. Subsequently, the fabrication of filters is focused on generating an interconnected void structure with a narrow diameter distribution. Basically, there are two ways to generate and control porosity. In the first approach, the material is selected in accordance to their particle size to create a defined pore distribution, which is called non-template. The second and most frequently used method requires the use of templates (temporal porous makers), which are removed during the sintering process.

2.1.1   Non-Template Casting

Numerous approaches to fabricate porous bodies with a grade of connectivity have been developed up to now. The formation of pores without templating offers appreciable benefits concerning the serial production of catalysts, because of its simplicity and low waste production. Powder compacting, extrusion and 3D printing are the most common techniques which are used in industrial applications like water filtering, automotive catalyst, and petrochemical refinery respectively.

Porous structures made from powder compacting strongly depend on a defined particle size distribution, in order to keep the connectivity of the free space between particles. After the agglomeration of particles and the binder, the mix is pressed to increase the effect of the binder, which will later melt and connect all the particles during sintering.

This technique produces low porosities and a high drop of pressure. Therefore, for applications with low pressure drop, bigger channels are required. To achieve this, usually extrusion processes are used. However, the homogeneity and interconnectivity of these pores are reduced by the sintering of the particles by the binder.
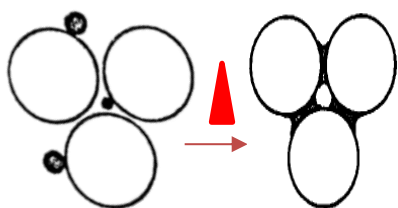
Figure 2-2. Powder Compacting. [254]
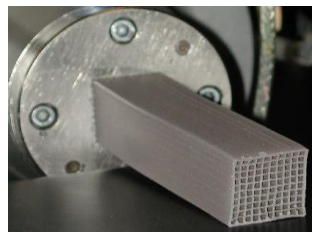
Figure 2-3. Honeycomb extrusion. [77]

Figure 2-4. 3D Printed Honeycomb. [78]

Currently, with the incorporation of 3D printing technologies, tailored porosity and complex channels can be fabricated at modest cost (see figure 2-4). On the one hand, customized geometries lead to fabricating monoliths for applications on intricate spaces, typically on mobile reactors [79]. On the other hand, complex channels notoriously increase the mass and energy transfer between the reactants and the catalyst. This fact makes printed honeycombs an ideal filter support for energy intensive reactions [80], [81].

2.1.2   Porous Material Synthesis by Templating

The use of templates avoids typical issues from the previous techniques, such as fouling and void formation. Moreover, chemical characteristics can be printed on the pores by using active organic templates (OSDA, Organic Structural Directing Agents), as in the case of zeolites. Once the porous network is defined for the template, as illustrated in figure 2-5, the support material undergoes a thermal treatment for hardening of the material. By doing this on ceramic filters, the organic template is removed through the oxidation of the polymer chains, whereby the filter material becomes strong due to the formation of silicate bonds [80].
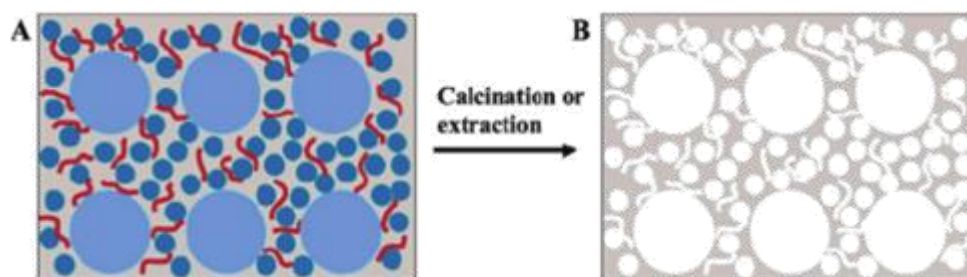
Figure 2-5. General Template Approach.

2.1.3   Template Driven Porosity

Organic templates are the starting point for mesoporous structures, which are eventually used as filters. A vast range of porosity diameters and shapes can be produced due to the infinite spectrum of organic molecules. For instance, hierarchical structures can be tailored with interconnected slim channels and large voids, as illustrated in figure 2-5, figure 2-6 and figure 2-7.
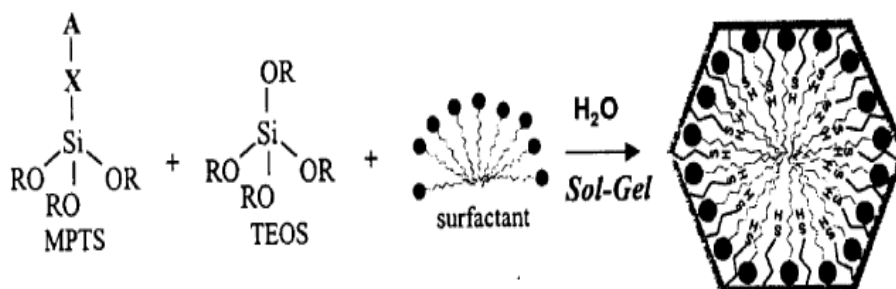
Figure 2-6. Polar Templating. [82]

Templating   of   polar   channels   by   using   dipolar   surfactant   with   silica   sources   of   mercaptopropyltrimethoxysilane and tetraethyl orthosilicate.

On addition to geometry, properties such as polarity and hydrophobicity are also transmitted to porous structures by mirroring the similar features on the template. For instance, acidity of the pores can be controlled through polarity of the template, as shown in figure 2-6 [82]. Other applications require selectivity of the pores, that means, preferential groups of molecules can travel freely across the pores (i.e. hydrophobicity). To deal with this, many researchers use large alkene chains with dipolar ions, i.e. polychain blocks as illustrated in figure 2-7. By using these organic chains, polar channels attract water, allowing the free flow of other compounds [83]. These templates are also called surfactants or ionic templates [84].
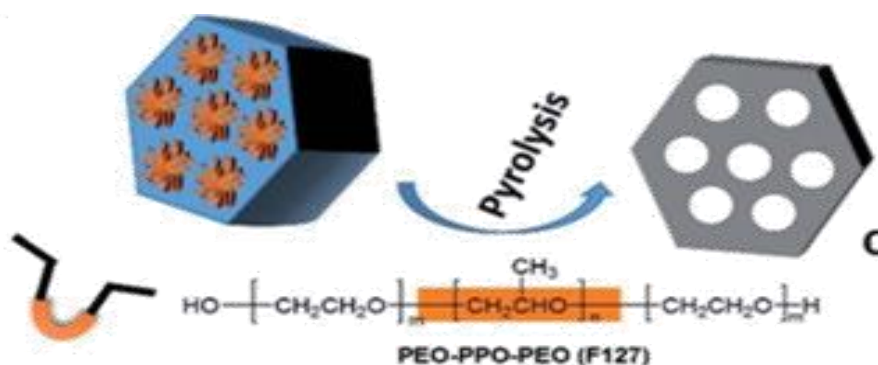
Figure 2-7. Hydrophilic Templating. [83]

Organic templating of long channels by using polymeric chains of block copolymer surfactant F127 (Polyethylenoxide-Polypropyloxide-Polyethylenoxide).

2.1.4   Molding of Porous Structures

The construction of a filter with a desired geometry requires the combination of powder, template and binder. Consequently, the mixture is homogenized under specified conditions, which evenly distribute the material components. To give a defined geometry, the desired mix is poured into a mold, where it is pressed to remove the void space in the body [85]. Finally, the monolith or green body is slowly dried and calcinated in order to give mechanical and thermal stability. These properties are required for the final application [86].

| Combination | Homogenization | Deairing | Molding | Drying | Sintering |
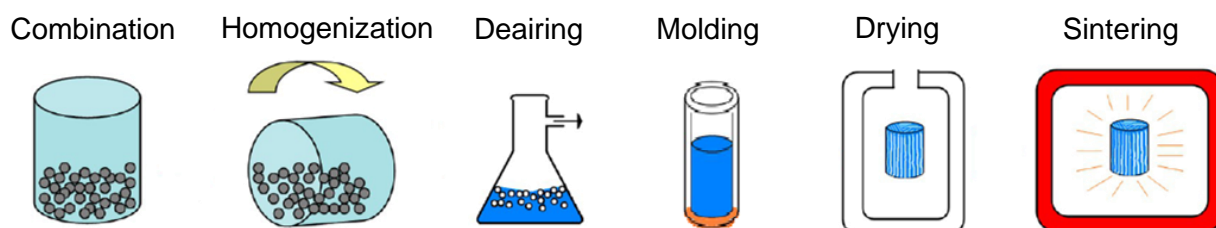
Figure 2-8. Monolith Molding. [87]

The final thermal treatment defines the chemical stability of the monolith. As the temperature increases, stronger chemical bonds start to balance the energy in the monolith and on the outside. Therefore, higher temperatures lead to more stable filters. However, side effects, such as surface relaxation and expansion, reduce the specific area and generate unwanted cracks [88].

2.2   Catalyst Synthesis

Before a catalytic material is synthesized, it is necessary to identify the critical steps, which define the reaction rate. Reaction mechanism, absorption, transition and surface energy are descriptors, which help to identify the key points of the catalyst synthesis. For instance, the catalysis synthesis aims to fabricate materials, whereby the energy of the reaction is minimized. To achieve this, a deep knowledge of the reaction pathway gives insight into the important parameters, which are needed in order to attain optimal conditions for a specified reaction [89].

Following this concept, the SCR reaction is thoroughly analyzed in this work. Through this study, the determining step is identified and used to design the active centers of the catalyst. Consequently, the catalyst synthesis is planned to stabilize these active centers.

2.2.1   NOx Reduction Mechanism

Nitrogen oxides reduction by ammonia is the most common reduction technique around the world, therefore this is widely used in cars, power plants, incinerators and boilers among others. For the sake of understanding, here only the reduction of NO by NH_3 is analyzed, because a complete reaction scenario includes several reactants, such as H_2O, O_2, NO_2, CO, CH_mO_m, which would mislead the reader. As shown in the reactions R 2.1 und R 2.2, nitrogen oxides are cleaved by deprotonation of ammonia, thus producing water and nitrogen gas.

$$6NO + 4NH_3 \rightarrow 5N_2 + 6H_2O$$ *R 2.1*

$$6NO_2 + 8NH_3 \rightarrow 7N_2 + 12H_2O$$ *R 2.2*

The accomplishment of these reactions requires several steps because of discrete electron transfer between atoms. Theoretically, a transference of 10 and 12 electrons is the minimum needed to complete the reactions R 2.1 and R 2.2, respectively. This suggests the formation of intermediate species that carry these charges. Currently, with the advancement on spectroscopy, more than eight intermediate species have been identified, which confirms the complexity of this basic reaction [90] [91].

To cope with the complexities of these temporal molecules, several researchers have elucidated mechanisms and reaction energies by using the Density Functional Theory (DFT) [92][93][94][95]. Detailed studies of the SCR mechanism indicate that there are even more steps because of effects, such as absorption, desorption and recombination [93]. Nevertheless, the combination of experimental evidence and computational chemistry calculations unravel the key steps of the reaction pathways [92].

Across the reaction pathway of NO several intermediate compounds appear, as is shown in the bottom line of figure 2-9. At the beginning an energy kick of 0,9 eV is required, which represents the energy supplied to oxidize the catalyst from $NOCu^+O_2$ to $Cu^{2+}NO^-_3$. This unstable configuration of the catalyst makes the reduction with ammonia easier, because of its high free energy value (see middle part of figure 2-9). When ammonia interacts with the activated copper center, intermediate species such NH_4^+ and HONO coordinate around the center. As a consequence, the copper center is reduced, thus enabling an exothermic reaction. Finally, the copper center returns to its initial state, releasing H_2O and N_2 as illustrated on the right side.
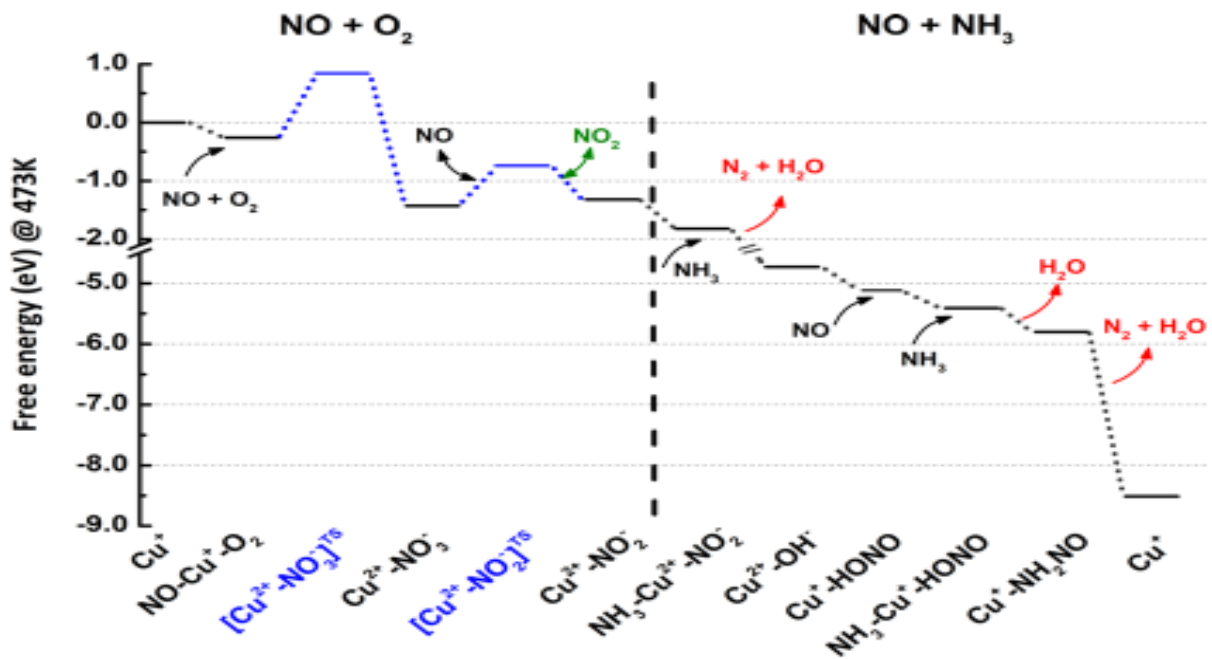
Figure 2-9. Free energy diagram for the NO activation over a copper catalyst. [92]

This detailed reaction pathway helps to understand, how the catalytical cycles could be optimized in the praxis. For instance, knowing the key step of the reaction allows focusing on the suitable structure for this state. After all, for designing the catalyst, the activation energy takes priority over all the intermediate exothermic steps, because this step determines the activation energy of the catalyst. Therefore, in several works as well as here, the catalyst is designed to reduce the activation energy [96]. In other words, the synthesis process must be focused on preparing surfaces with available Cu^{+1} ions, which react selectively with NO and NH_3.

2.2.2   Chemistry of the SCR Catalyst

As previously explained, the reduction of NO requires several steps, which are directly defined for the structure of the catalyst. Therefore, a study of the interaction between the gas phase and the solid material is fundamental for synthesizing the suitable material. In the past, the material selection was achieved by experimental screening of material [97]. However, as soon the material becomes heterogeneous (i.e. dopants, promoters, inhibitors), cost and time grow exponentially for experimental screening.

Fortunately, due to the advancement of computational capacity nowadays, theoretical models can be applied to small clusters of atoms. These models use DFT algorithms (Density Functional Theory), which come from the simplification of quantum physics for material science. Through these simulation tools, surfaces, absorption and desorption energies are

calculated at molecular level. Additionally, other important parameters for catalysis, such as activation energy and transition state, can be estimated in detail. With these energy states and complementary experimental data, it is possible to build a reaction path for catalytic material as exemplified in figure 2-9 and Figure 2-10.
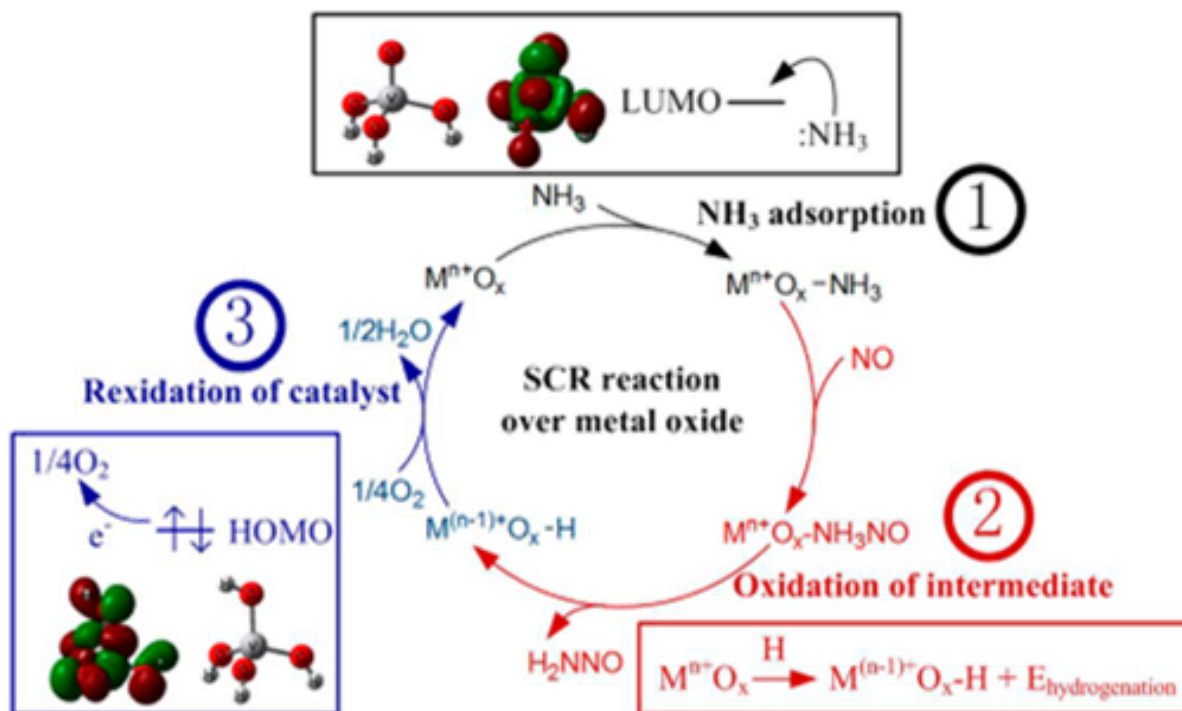
Figure 2-10. Energy states of a SCR cycle. [98]

These tools are also strategically used for catalyst designing [96], [99] [100]. For instance, NO oxidation and ammonia reduction effects were calculated for several supported metal oxides by DFT methods [98]. That study shows comparable results between theory and experiments that validate previous material screenings.

From simulations, the highest activation energy occurs on the transition from the LUMO (Lower Unoccupied Molecular Orbital) to the HOMO (Higher Occupied Molecular Orbital), see figure 2-10 and it also corresponds with the oxidation of the metal center due to NO. Consequently, materials with low surface energies between these two stages facilitate the transition of the reagents, as shown in figure 2-11. Therefore, materials with short arrows are good candidates for NOx, because they require less absorption for NO uptake.
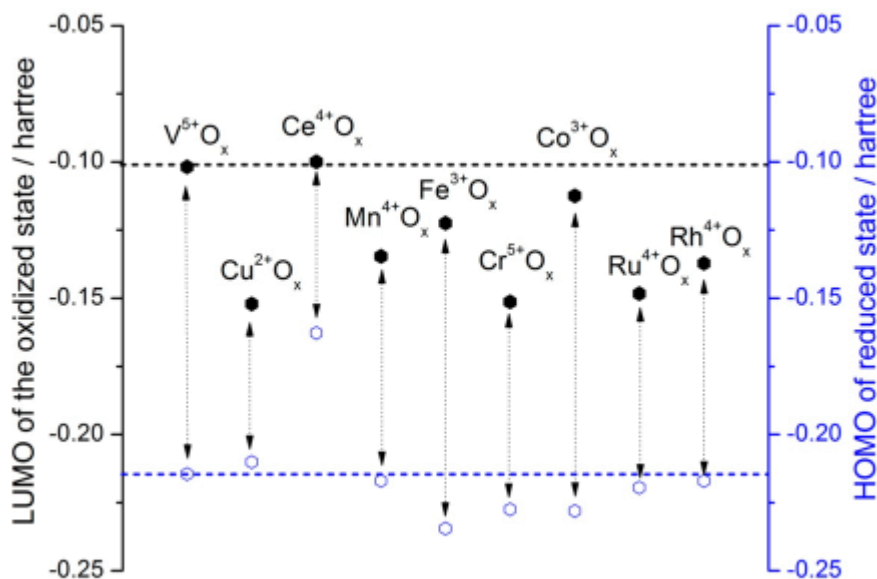
Figure 2-11. LUMO and HOMO energy on metal oxides at SCR conditions. [98]

For the sake of simplicity, LUMO energy can be seen as the energy in the reduced state and the HOMO as the energy in the oxidized state respectively. Figure 2-11 shows the energy change during SCR catalysis for several metal oxides. Therefore, the shorter the arrow band, the lower the activation energy.

In a catalyst, lower activation energies are crucial, but the absorption and/or desorption energies are even more important. These energies indicate the barriers for absorption of reactants and desorption of products, which are represented with black and blue dots respectively in figure 2-11. That means, lower blue dots represent strong absorption of NO, while black ones indicate strong absorption of NH_3. This fact makes elements such as Copper, Chrome and Ruthenium theoretically good candidates for a SCR.

2.2.3   Preparation of Active Centers

In catalytic materials, the preparation of the active center is the core task. As shown in the previous example, an active center could be a simple metallic cation (see Cu^+ in figure 2-9) [101]. However, on real materials, metallic cation must be stabilized so that it can be used as a catalyst. An approach to stabilizing a metal center is based on the foundations of organometallic chemistry and more specifically on C-C bond chemistry. There, organocopper complexes are used most frequently [102].
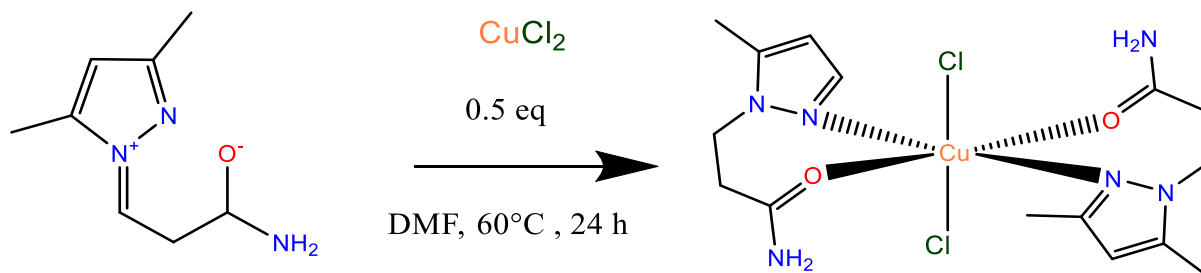
Scheme 2-1. Synthesis Copper Complex. Adapted from [103].

The synthesis starts with the dissolution of a copper halide in an organic solvent. This polarizes the halide toward the nucleophilic part of the solvent. To activate the metallic center, an organic ligand is added. By doing so, the halide reacts with the amine tail of the ligand, which reduces the copper salt to organocopper (see right side in scheme 2-1). Following the substitution mechanism, ammonium salts precipitate, which releases the organic copper complex in the solvent. To finish the synthesis, the solution is filtered, which allows to remove the ammonium salts [102].

2.2.4   Stabilization of Catalytic Centers

Organocoppers do not tend to be stable, thus they oxidize upon contact with air or other electron donors, due to the tendency of organocoppers to form halides. This fact implies the uses of solvent media with controlled pK_a (acid dissociation constant) values over 10, in order to keep these compounds catalytically active [104]. This technique is widely used in Ullman reactions, because liquid reagents are preferred in homogenous catalysis of carbanions, alkyl, alkenyl and aryl substrates [105].

However, regarding heterogenous catalysis, a robust approach is required. The use of organosilicas is becoming popular, because they could be arranged strategically to provide selective environments during reaction. By using these housing structures, it is also possible to get molecular sieving [106]. In other words, only the molecules, which energetically fit on the host structure of the catalytic center, can react with the active center. Additionally, selectivity effects could be tuned through reacting groups, such as ammines or carboxylic acid, which control the transit of polar molecules, like water or proteins [107].
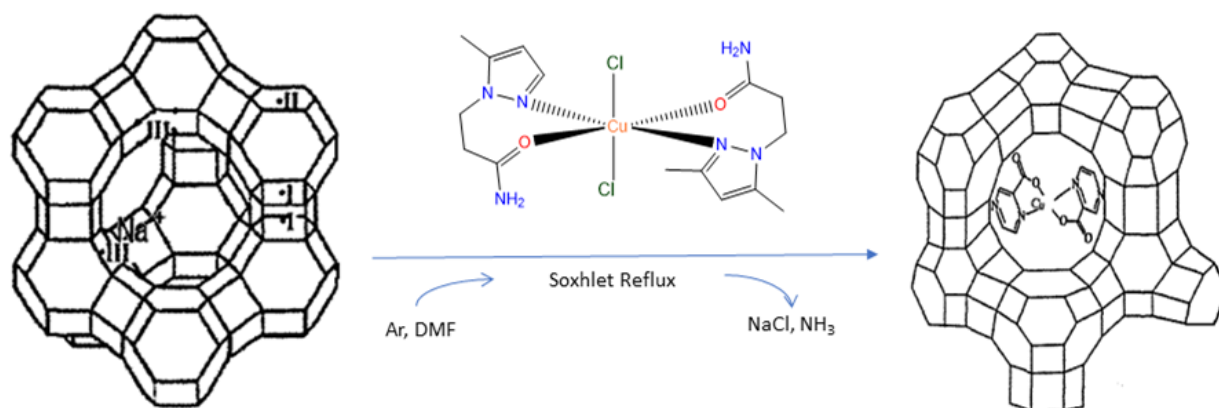
Figure 2-12. Ion exchange of Copper Complexes. Adapted from [108].
Na-Y zeolite is exchanged under DMF solvent, using Soxhlet recirculation. Reflux of Copper complex in the
zeolite forces the reaction of Na with Chloride leading to an encapsulated compound.

In accordance to the enclosing grade, the techniques vary from grafting across anchoring in zeolite structure until encapsulation. All these methods use the acidic properties of silica compounds to anchor organometallic complexes. For instance, porous structures with active sites, such Na-Y zeolites, are used for exchange with organometallic complexes, as is shown in figure 2-12.

During the exchange of complexes in Na-Y zeolites, the zeolite cation (sodium cation) reacts with the electrophilic group of the complex by means of a Soxhlet process. In this reaction the sodium reacts with the electrophilic part of the copper complex. Simultaneously, the nucleophilic amine group attacks the acidic center of the Y-zeolite, which promotes the attachment of the complex to the zeolitic structure by covalent bonding at the aluminum atom [108].

2.3   Catalytic Filter Integration

Catalyst coating is the typical industrial way to combine the catalyst and the filter, but, as discussed previously (see chapter 1.7.1), this technique generates considerable waste. Moreover, other effects, such as lack of uniformity [109], leaching [110] and sintering [111], appear when the pore diameters decrease [112]. Due to the fact that deposition methods need a liquid solution to disperse the catalyst on the support, the capillary forces in the pores increase exponentially when the pore size decreases. This phenomenon limits the catalyst transport across dense materials, because capillary forces limit deposition of the catalyst on the pores [113].

To have a reliable process for the integration of the catalyst and the filter, an encapsulation of the catalyst was developed in this work. This enables catalyst deposition in small pores, as is explained in subchapter 2.2.4. In the following paragraphs, the integration of the previously illustrated catalyst with a support will be explained.

2.3.1   Hard Templating

The use of sacrificial organic templates is also known as hard templating. This method consists of coordinating organic templates, such as CTAB (Cetymethyl-Tetramethyl-Ammonium Bromide) with catalytic material in order to protect the catalyst during the casting of the filter structure (left side of figure 2-13). To summarize the process, an organic template binds on the acidic site of the zeolitic structure, producing micelles as illustrated below. These organometallic core shell particles protect the catalyst during the upcoming step. In the final step, after calcination, organic matter is removed, whereby free space is provided to access the catalytic centers [114].
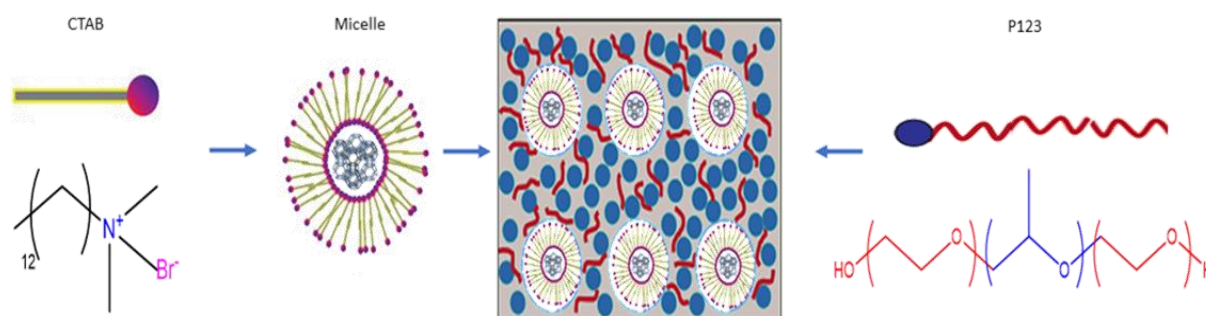
Figure 2-13. Hard templating on hierarchical structures. Adapted from [115].
Left: encapsulation of catalyst by CTAB. Middle: Matrix of templated catalyst with support material. Right: block copolymer for macro porosity formation.

To connect the active centers with the pores of the filter, a block copolymer template is used. Due to the size and functionality of these polymers, complex porous networks are shaped in the filter. On the left of figure 2-13 there is a representation of a polymer template. P123 (Pluronic 123) is a polymeric chain with two hydrophilic branches, marked in red, and one hydrophobic one in blue [116]. This feature leads the polymeric chain to organize with the micelle surfactant in the presence of a non-polar solvent. By doing so, the hydrophobic chains unroll towards the place without a catalyst, whereby it forms a hierarchical network porosity.

2.3.2   Filter Shaping

A deeper contact between the binder and the support material is fundamental during the thermal treatment of a filter. To assure that property, the binder and the support material are

joined by a pressing process. Similarly, as explained in paragraph 2.1.1, the substrate powder and the binder are mixed and, subsequently, mechanically pressured in a mold.
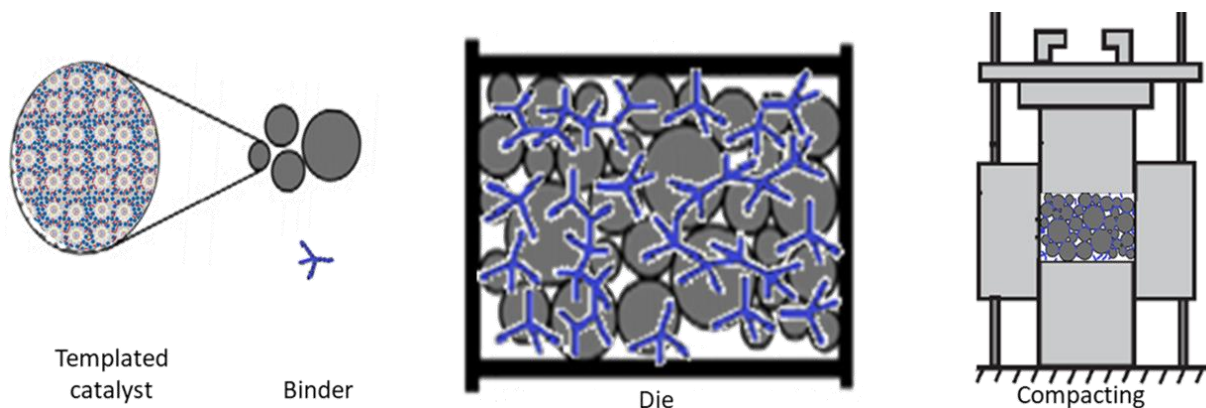
Figure 2-14. Powder pressing.
Left: Previous template catalyst is mixed with an inorganic binder and the filter material. Middle: mixed material is filled in a die. Right: Pressing process delivers a compact monolithic catalyst.

A finer contact could be tailored with excess of binder, however, this excess forms cracks in the monolithic filter afterwards [117]. To deal with this, high punch pressures of around 20MPa improve the efficiency of the binder. Furthermore, air pockets are flushed out of the body [118].

Additionally, to join the particle in the compressed body, the binder facilitates the flow of the powder across the mold. For instance, the remaining air on the corners of the mold is normally evacuated, when the compacting is done stepwise.

Higher plasticity of binder improves the flowability of the material during compacting, which reduces the formation of air pockets in the body. But low elasticity is required at the same time in order to increase the density of the final product. For this reason, an inorganic binder is preferred for powder compacting methods, when mechanically stable filters are wanted [119].

2.4   Thermal Treatment

The calcination of the catalytic filter involves several chemical reactions, depending on temperature and gas atmosphere. Along the temperature increase, several chemical compounds begin to overcome their chemical potential, leading to reactions, such as organic template combustion and aluminosilicate oxidation. These chemical transformations directly influence the properties of the catalytic filter. Hence, parameters, such as thermal stability, porosity and catalytical activity, can be tailored in this last step [120].

In most of the cases, the calcination atmosphere is air that results in the formation of oxides. However, changes in the chemical composition of the calcination atmosphere can drive the chemical composition and consequently the activity of the catalyst. In consequence, modification of the calcination atmosphere plays a crucial role in the activation of the catalyst [121].

2.4.1 Temperature Programming

In a molded catalyst, there are different components, which also have different thermally behavior. Therefore, during the temperature increase, several reactions are activated gradually. When the critical temperature of the organic template is passed, the soft component of the catalyst is entirely removed. This template removal produces a thermally and mechanically stable solid monolith.

High calcination temperatures result in more stable monoliths. Unfortunately, at the same time, catalytic centers are deactivated, because under these conditions the catalyst centers become stable as well. This fact makes the catalyst less active. Hence, the thermal treatment should be set in order to reach the right balance between stability and activity.

This can be attained through a careful analysis of the template decomposition. To study this in more detail, some authors have used DTG characterization (Differential Thermal Gravimetric analysis) in order to trace the temperature and energy released along the temperature profiles [122].

As the following figure illustrates, during calcination of templated structures, usually two peaks are found. The first one indicates the release of polymeric chains and organic monomers, while the second one corresponds to the release of more stable organic structures, such as heterocyclic rings. In practice, for the design of the temperature profile, the first exothermic peak is taken, because it promotes the decomposition of the next components.
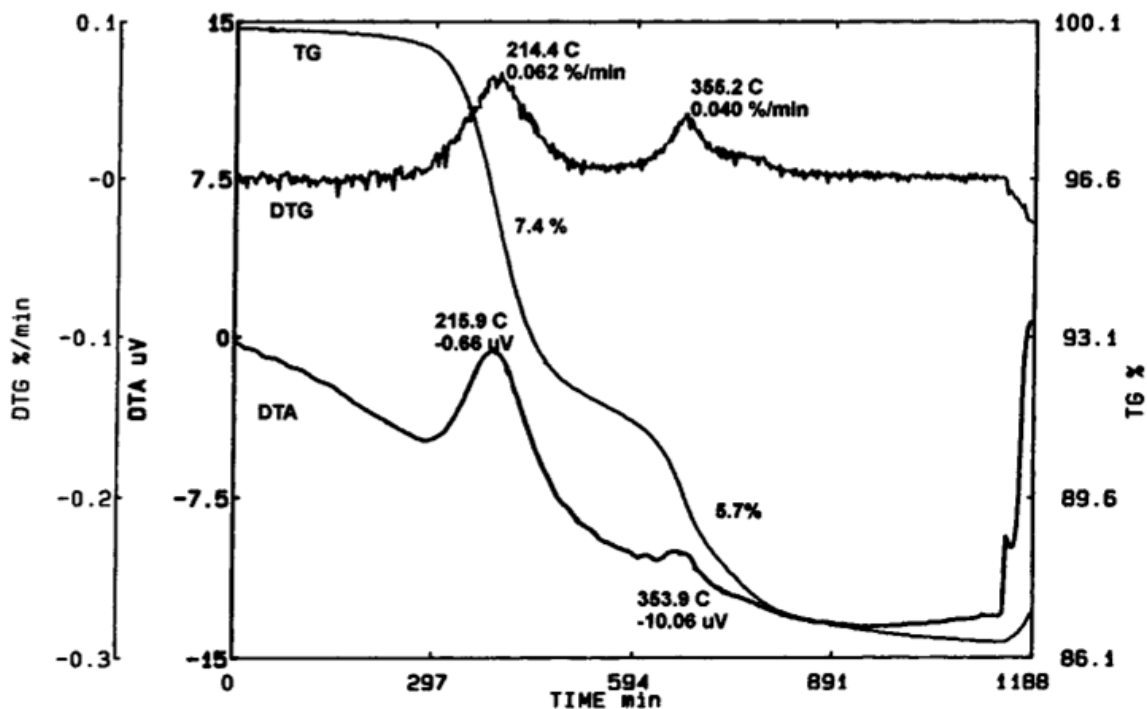
Figure 2-15. DTG study for template decomposition on zsm-5 [123].
TG: percentual weight of the sample. DTG: Percentual loss of weight per minute. DTA: change in
temperature. Heating rate: 0.5 °C/min.

On the other hand, exothermic energy releases are also seriously taken into consideration, because of their damaging potential. Hence, the energy release in the calcination chamber is controlled by the heating rate, see DTA line in figure 2-15. For instance, the effects of an exothermic release can be downsized by increasing the calcination time. In other words, exothermic peaks can be flattened easily be decreasing or even neutralizing the heating rate at the critical temperatures.

2.4.2   Influence of the Calcination Atmosphere

High calcination temperatures (over 700°C) assure thermal stability of the monolithic catalyst. However, high temperatures play against the catalytical activity of the system because metal active centers start to join [124]. Hence, for synthesis of catalytic materials, a lower calcination temperature is preferred. For instance, calcination temperatures can be reduced by adding an oxidant without affecting the active center [125].

One way to reduce the calcination temperature relies on speeding up the oxidation of the template. Hence, changes in the oxidant can remove the template at low temperature stages. This idea motivated the modification of the calcination conditions. For instance, an addition of ozone has been successfully tested for the synthesis of zeolites [126].

Calcination with ozone reduces the calcination step by 100°C, as shown in green and violet in figure 2-16. Furthermore, the release of the template proceeds more smoothly on ozone than in air. This can be observed on the wide band of the DTG lines, grey and brown, for ozone and air respectively. These improvements influence operation costs of industrial zeolite production. Moreover, shortening of the calcination time is reported [127].
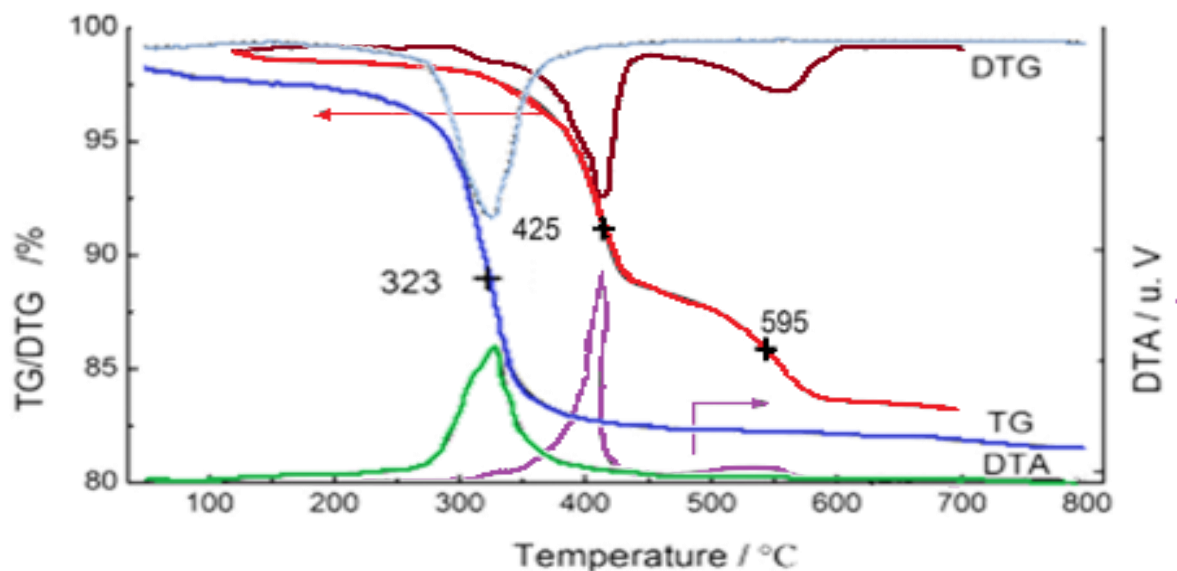
Figure 2-16. DTG analysis of template decomposition with and without ozone. Adapted from [125].

Violet, red and brown lines stand for DTA, TG and DTG experiments with air respectively. Green, blue and grey lines stand for experiments with ozone addition.

Regarding catalysis, modification of the calcination atmosphere also positively influences the activity of the catalyst. This was discovered in the synthesis of a De-NOx catalyst by solid ion exchange [128]. In this example, a mixture of NH_3, NO and air was used in the calcination process for treatment of the support. After the thermal treatment, the catalyst particularly increased its performance. According to this study, this thermal treatment condition increased the diffusion of metal cations in the structure, as figure 2-17 illustrates.
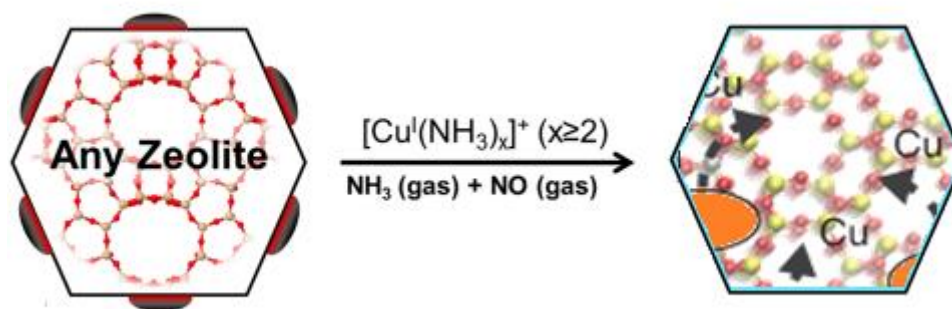
Figure 2-17. Solid state copper exchange. Adapted from [129].

After an exhaustive spectroscopy and catalytic test, it was found that the redox conditions reduce the copper particles to an atomic scale, which notably increases NOx conversion of this catalyst [130]. This finding clearly shows that catalyst activity can be driven more selectively by a suitable atmosphere during thermal treatment.

2.5   Overview of the Fabrication Process

At this point, the techniques for fabricating a catalytical filter have been explained chronologically. Several diverse fabrication steps, from organometallic synthesis to thermal reduction, are involved in the fabrication of the catalyst. Despite of the variety of these techniques, most of them point towards to the stabilization of the active centers and their integration into a porous material.

Catalytical performance depends on the active center, but this is only one part on the process. Absorption and mass transfer properties of the monolith also need to be engineered. For instance, the addition of absorbers in commercial catalysts is a common practice [131]. Following this standard procedure, the addition of the absorber is done during the casting of the porous body, see section 2.3.2.

During casting of the monolith, catalyst, filter, binder and promoter are involved. In consequence, the heterogeneity of the catalytic filter becomes unpredictable at this point. To find an optimal ratio between catalyst, filter support and absorber, a material screening was planned. The De-NOx performance of the catalyst was used as an evaluation parameter. In that way, the final composition of the catalyst was estimated in accordance to practical results. Further details are found in section 5.1.2.

3 Process Development

In the previous chapter the foundations for the design and fabrication of the catalytic filter were explained. Thus, the experimental parameters for the fabrication of the catalytic filter will be described now. To complement the theoretical concepts, experimental data and empirical findings from similar works are used to complement the fabrication method.

The fabrication method consists of several steps. Briefly, the active catalyst is synthetized initially. Then, the catalyst material is integrated in a support. Next, the supported catalyst is mixed with a porous template and shaped into a monolithic filter. To finish the fabrication, the monolith is calcinated.

3.1 Active Centers Synthesis

In this work, the catalytic materials were synthesized by organometallic chemistry according to chapter 2.2.3. As previously explained, the synthesis of the active centers aimed at performing the reactions R 3.1 and R 3.2. Fortunately, there are several materials, here simplified as M^+, which can perform these redox cycles. Particularly transition metals are well-known by their catalytical properties.

$$NH_3 + M^+ \leftrightarrow NH_4^+ \cdots M \qquad\qquad \textbf{\textit{R 3.1}}$$

$$NO + M^+ \rightarrow NO^- \cdots M^{2+} \qquad\qquad \textbf{\textit{R 3.2}}$$

Transition metal oxides, such as copper-, iron- or zinc oxide, can activate ammonium molecules, because they behave as Bronsted acids [97]. This property enables the formation of ammonium cations as shown in R 3.1. Furthermore, these metal oxides can also be oxidized by nitrates, which is an advantage for the NOx reduction (see R 3.2). As a consequence, these materials can be used for the synthesis because these two reactions can simultaneously occur on the surface of these oxides.

3.1.1 Materials

vi. Active Center Material

NOx emission reduction has been an object of intense study for more than 30 years [132]. This extensive research provides a good screening of the suitable materials for reduction of NO with NH_3 nowadays [133] [134] [135]. Below, figure 3-1 summarizes many of the results, where

numerous materials were tested and classified regarding temperature of activation, NOx conversion, cost and environmental impact.
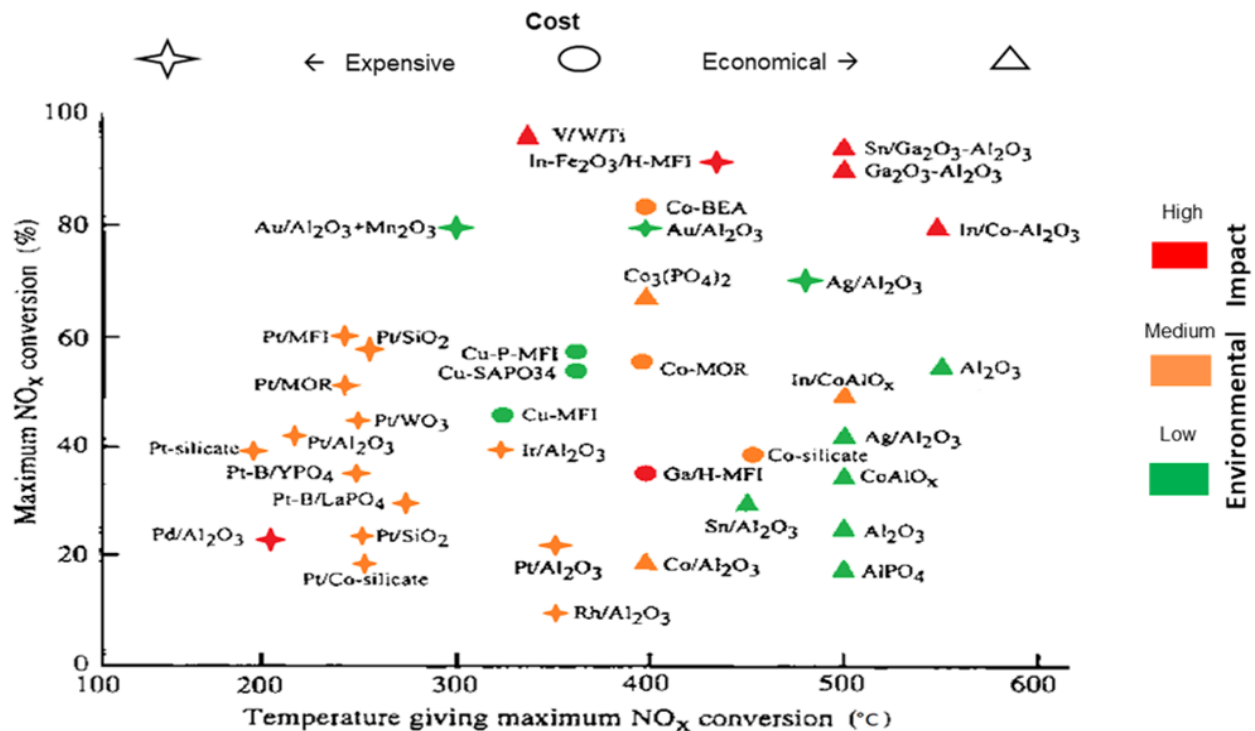
Figure 3-1. Review of NOx Conversion vs. Temperature from several materials. Adapted from [134].

Reported NOx conversion of several materials in relation to temperature. Environmental impact during the fabrication, operation and material life-cycle are highlighted with colors, green, orange and red. Availability and cost of the raw materials are illustrated with triangles, circles and stars. Costly raw materials are marked with stars, while economical ones have triangles. See upper legend.

Maximum performance and low temperature operation seem to be the ideal target when searching for suitable materials. This ideal area is located at the upper left side of figure 3-1 and is also dominated by noble metals, such as palladium, platinum and indium. But for industrial application, these materials are expensive not only because of their prices but also because of their poor availability and environmental impacts [136].

Some economical options appear in the middle upper part. Nevertheless, these metal oxides of vanadium, gallium and indium are strictly controlled because of their toxicity. Unfortunately, this fact limits their application for air cleaning.

On the right side of figure 3-1, there are more economical options, which conversely provide low emission reduction. Low NOx conversions can be compensated easily by increasing the amount of the catalyst. Hence, for stationary emission sources, these large quantities of catalysts can be readily accommodated because of the availability of space.

Alternatively, when space and energy efficiency are demanded, more efficient and economical catalysts are needed.

The mixture of transition metals and mesoporous supports offers an advantageous trade-off between cost and efficiency. This fact oriented the research in the direction of metal exchanged porous materials. As a result, structured combinations of transition elements, such as copper, iron and manganese with zeolites have brought successful results in several applications, which is illustrated in the center of figure 1-13.

Based on these results and the calculation of Xuesen [98] - as explained in 2.2.3 - copper oxides are the optimal candidates, when parameters, such as efficiency, cost and sustainability must be balanced [137]. Hence, a copper salt is used as a starting precursor for the synthesis of the active center.

vii.   Template

Incorporation of the active center in a ceramic support requires preparation of stable copper compounds, which remain isolated during the sintering of the monolith. Halogen copper salts, such as CuCl, CuBr and CuI, are typical examples of stable compounds. However, in the synthesis of the catalytic filter, the removal of these halogen elements would be extremely corrosive, if they stayed at the core of the catalyst. Hence, a metastable copper complex is preferred in organometallic synthesis, because it can later be removed easily by thermal treatments.

Organometallic complexes with copper have been widely developed because of their application in the textile and pharmaceutical industries [102]. Hence, the selection of a suitable complex was based on organocopper compounds, which show stability under air at under 300°C. A good candidate was found in synthetic enzymes, such as Tyrosinase. There, copper is coordinated with pyrimidine and pyrazole ligands for catalyzing dioxygen splitting, as shown in figure 3-2 [138] [139] . Moreover, copper pyrazole complexes show high stability at mild temperature, because the affinity between copper and nitrogen [140].Therefore, in this work, these azole compounds were also used, because of their affinity to form copper complexes and also their commercial availability.
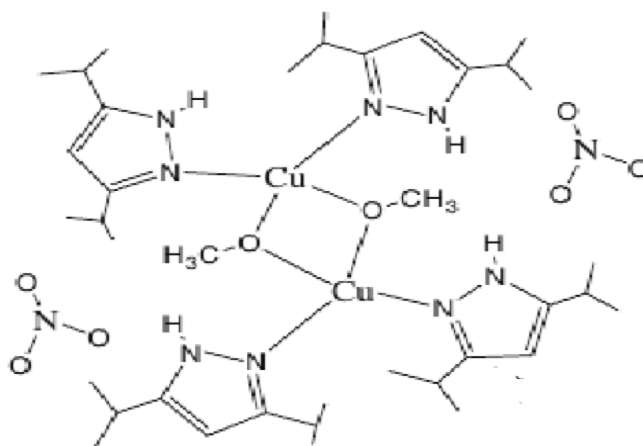
Figure 3-2. Tyrosinase mimic base on Cu-Complex. [141].

Dimeric Copper bis(Dimethylpyrazole) nitrate for cleaving oxo-bonds on DNA.

viii.   Solvent

Once the starting catalyst precursor is defined, a solvent is used to facilitate the dissolution of the metal cation. In the case of copper nitrate, several solvents are able to dissolve nitrate salts [142]. However, only a few solvents were tested, due to compatibility properties with copper nitrate. In table 1-1, these properties are shown, i.e. boiling point and water solubility [143]. In a controlled experiment, the solvents were tested with the catalyst precursor and the template in order to evaluate the stability of the catalyst in this solution.

Table 3-1. Properties of tested solvents.

Solvent	Formula	MW	Boiling point (°C)	Melting point (°C)	Density (g/mL)	Solubility in water (g/100g)
Dimethyl-formamide (DMF)	**C_3H_7NO**	**73.09**	**153**	**-60.48**	**0.9445**	**Miscible**
Dimethyl sulfoxide (DMSO)	C_2H_6OS	78.13	189	18.4	1.092	25.3
Pyridine	C_5H_5N	79.10	115.2	-41.6	0.982	Miscible

In this experiment, the copper salt, the template and each of the solvents from table 3-1 were mixed in mild conditions. Then the temperature was increased to 120°C under stirring condition to remove the water without reducing the copper particles in the solution. After 24 hours of reaction time, the solution was inspected for signs of precipitated copper. This indicates the stability of the active center in the solution.

The lower precipitation of reduced copper was observed in the solution prepared with DMF. A reasonable explanation resides in the polar aprotic properties of the solvent, which enables the stabilization of nitrates during the water migration [144].

3.1.2 Preparation of Metal Complexes

i. Synthesis of Template

Usually templates are also stable molecules, which need to be prepared for the coordination with the meta cation. An effective way of creating organic azole compounds with relative stability in mild conditions is founded on the preparation of pharmaceutical and special antiseptical compounds. In this chemical process, ligands, such as pyrazole, can be coordinated through their ammine branches. Recently, these synthesis methods have also been used for battery materials because of their acid-base properties [145] [146].
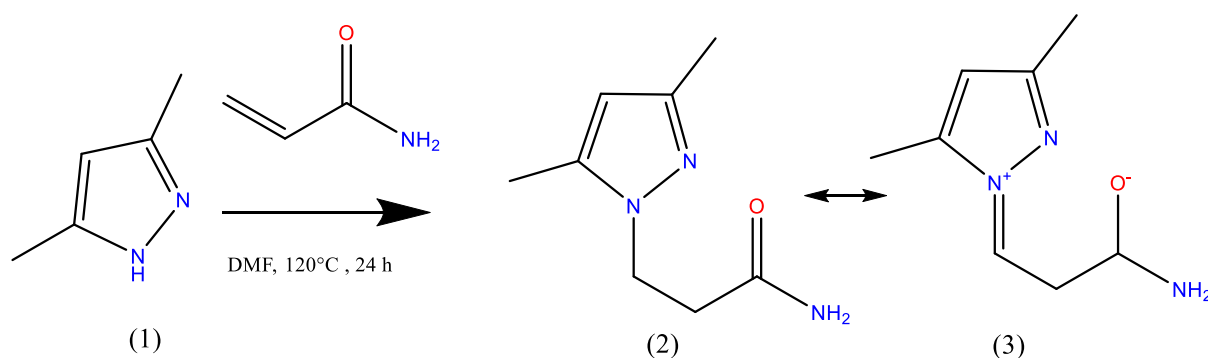
Scheme 3-1. Synthesis of N-Pyrazolpropamide. Adapted from [147].

For the reaction with diluted copper, the template needs to be functionalized with an acid group [105]. Briefly, a Michael addition of pyrazole to an amide is prepared as illustrated in scheme 3-1. Commercial sources were used for the preparation without additional purification steps. The reaction was carried out under mild conditions overnight with Dimethylpyrazole and Acrylamide. The product consists of a mixture of Dimethylpyrazole, and tautomeric bidentate ligands, where the latter can be coordinated with a metal ion.

ii. Copper Complex

The preparation of the complex is carried out in a closed glass reactor equipped with operating valves and a thermostat. 140 mL solvent DMF and 0.1 mol of $Cu(NO_3)_2$ are mixed at 60°C for 8 hours to completely dissolve the metal ions. A second mixture of 0.2 mol of pyrazole ligand is diluted on butanol at 60°C. Butanol is added to the latter mixture until the pyrazole compound is completely dissolved. Next, the second mixture is added dropwise to the first one under a nitrogen atmosphere.

In this state, the copper cations preferentially coordinate with these nitroso bonds (N-O), when the temperature slightly rises, as shown in scheme 3-2. This leads to the formation of Cu bipyrazoles nitrate, as analyzed by Barszcz [148]. Because of the hydrogen bonding between the amide group and the nitrate ions, a closed octahedral structure is formed, which was verified by use of X-ray measurement in [149]. This structure shows stability until 150°C, which is an adequate temperature for the upcoming synthesis in DMF media.
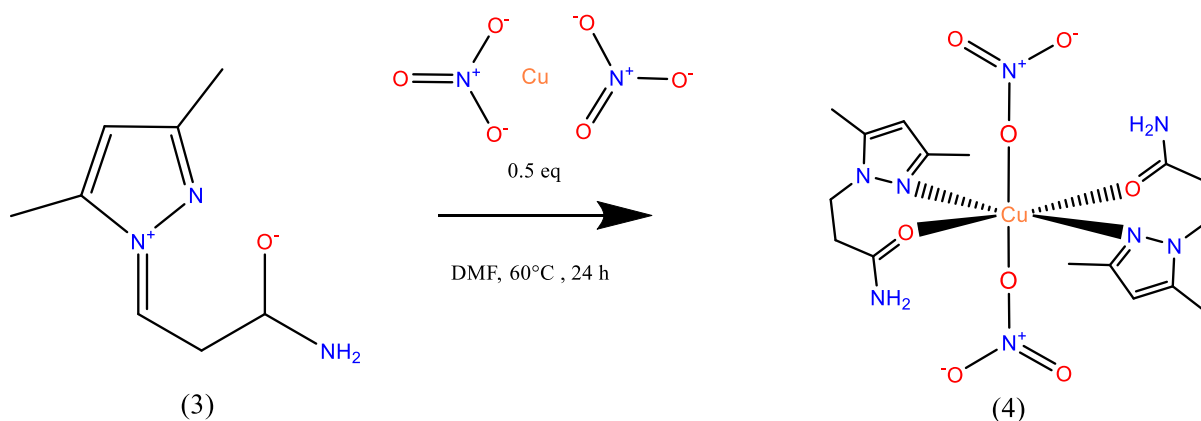
Scheme 3-2. Synthesis of Cu bipyrazoles nitrate. Adapted from [148].

Finally, for safety reasons, the blue pale mixture is continuously stirred under isolation from air until the solution is ready for the next step [150]. Moreover, the temperature must be carefully controlled because the complex tends to crystallize as an effect of dipolar solvent, when the temperature cools under 50°C. On the contrary, if the temperature increases to over 120°C, the nitrate ions react with the amine groups of the pyrazole ligand. That reaction releases a high amount of energy, which evolves into evaporation of the solvent and reduction of the copper to a metallic state (Cu^0). For this reason, the process is scheduled to continuously run with temperature control.

3.1.3 Stabilization of the Copper Complex

To stabilize the complex in a more solid structure, it can be exchanged in a zeolitic structure. This process requires the use of a zeolite with big porosity able to host complex molecules. In accordance to the size and polarity of the synthesized complex, a zeolite from the family faujasite, in some sources referred to as FAU, was chosen because of its large porous and Bronsted acidity [151]. For this reason, FAU zeolites and particularly Na-Y zeolites are widely used for hosting of Salen complexes [152].

Na-Y zeolite exhibits a low ratio of Si/Al, which facilitates the exchange of organometallic complexes due to their Bronsted acidity on the aluminum bond. However, these bonds are already occupied by sodium moieties, thus these moieties need to be exchanged for more

suitable cations (see (5) in scheme 3-3). This is carried out by a pretreatment in aqueous ammonia solution at low temperature. Since ammonium hydroxide evaporates easily at low temperature, this treatment is done at 30°C by dropwise addition of ammonia. When the pH values reach stable values of approximately 9, the process can be stopped. To remove the sodium salt (NaOH), which converts into ammonium form Zeolite (6), the precipitate is filtered three times until the washing water reaches a neutral pH value.
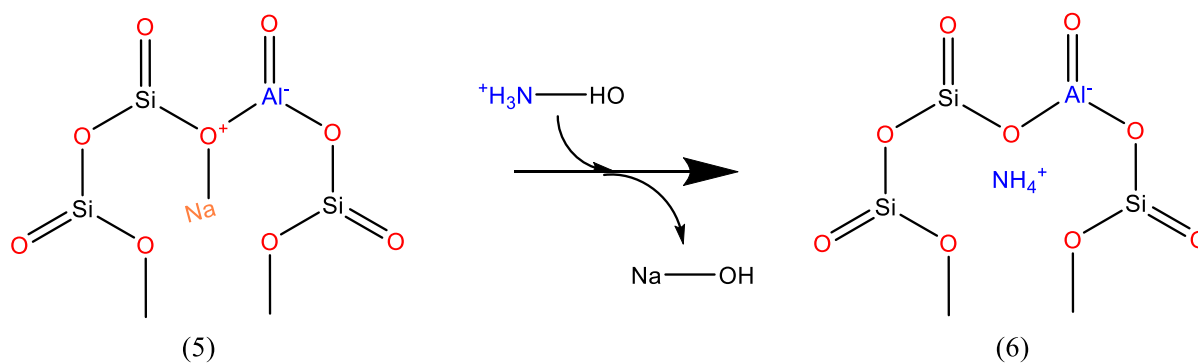
Scheme 3-3. Ammonia exchange of Na-Y zeolite.

In a following step, the complex (4, see scheme 3-2) is exchanged by an electrophilic attack of the nitrosonium ion NO^-, which is present in the previously prepared catalytic solution [153]. During the complex exchange, the reaction of the nitro group with the primary ammine in (6) produces nitrogen gas and water, as illustrated in scheme 3-4. Following an iminium mechanism, an iminium ion is temporarily activated on one of the two branches of (7), as shown in scheme 3-4. This unstable imine activation can result in the reduction of the copper atom from Cu^{2+} to Cu^+, which finally compensates the acidity in the zeolite cage [154].
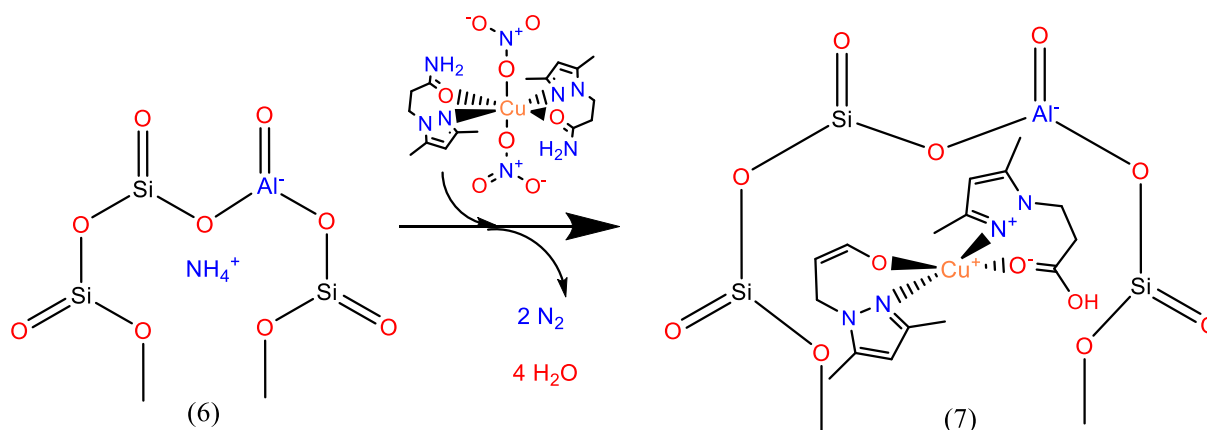
Scheme 3-4. Complex exchange.

Since this complex exchange shows low rates, the reaction is done in similar conditions as in the zeolite exchange. Due to the fact that water and ammonia are expected byproducts, the

reaction is also carried out in a dipolar solvent (DMF) for thermal distillation of the mentioned byproducts. After 24 hours of constant stirring, the solution changes from blue to violet or red, which indicates the partial reduction of copper [155].

The aluminum atoms of the zeolite structure are usually the anchor point for the complex, because they generate the Bronsted acidity in the cage. Therefore, these aluminum bonds are a good indicator of complex immobilization after the ion exchange process. Consequently, to verify the stability and activity of the encapsulated complex, spectroscopy techniques are used. For these solid supports, EPR or NMR can indicate the characteristics of the aluminum bond in the zeolite, which can give insight into the copper complex in the zeolitic structure [156] (see chapter 6).

3.2   Integration of Catalyst and Support

The catalytic material plays the main role in the catalytic filter, but in practice, a solid structure is needed for the hosting of the active phase. Hence, a support structure is as important as the catalyst itself. In recent years, the fabrication of catalytic materials was dominated by the coating process. Coating requires a support, which already contains a defined porosity. Supports with high porosity are easy to coat, but they lack filtration efficiency, while low porosity ones reject the coating, because the pores become plugged. Therefore, filtration of small particles and high load coating are not compatible in the same device [157].

To tackle this incompatibility issue typical in low porosity supports, a catalyst integration concept was tested in this work. Conversely to coating processes, here, the catalyst is synthesized and encapsulated before the casting of the porous structure. The integration of the catalyst and the porous filter is done by shaping a monolith into a mold, which contains a mixture of the catalyst, the support, and the binder [158].

3.2.1   Encapsulation of the Catalyst

Due to the high ratio of negatively charged cages on zeolite Y, an encapsulation can be carried out with ionic surfactants [159]. Through a simple preparation also illustrated in scheme 3-5, a zeolite structure can be encapsulated with large surfactant chains. In this step, zeolite structures are encapsulated by controlled addition of surfactant CTAB (cetyltrimethylammonium bromide) in tert-butyl alcohol. For the encapsulation of the catalyst, this surfactant was used with the complex (7) seen in scheme 3-4.
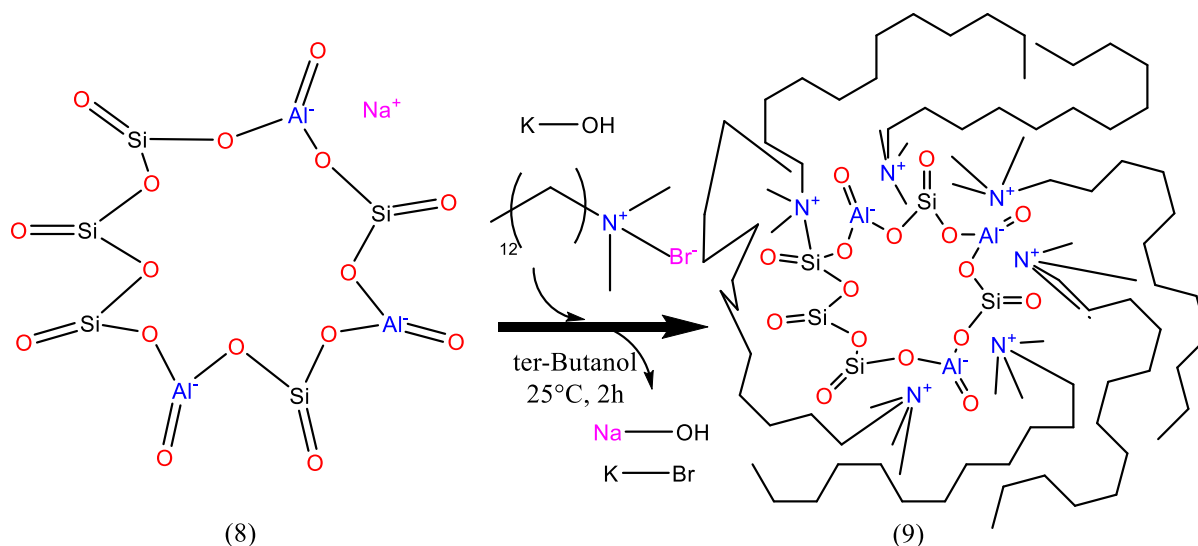
Scheme 3-5. Micelle formation with CTAB.

After the treatment with CTAB, small clusters (9), also named micelles, exhibit hydrophobic behavior, which makes them stable in ter-Butanol solvent. On the other hand, NaOH and KBr precipitate slowly, thus facilitating their filtration after 4 hours.

To continue with the encapsulation, a silanol agent, TEOS (triethylorthosilicate), is added dropwise to form a silica shell, as is shown in scheme 3-6. After a few minutes of stirring, the mixtures start to gelate, which is normal in silica gel preparations. To avoid the gelation of the silica before the silica agent is completely added, the mixture is diluted with 2-propanol. This solvent addition keeps the pKa value neutral during the mixing of the TEOS and the catalyst.
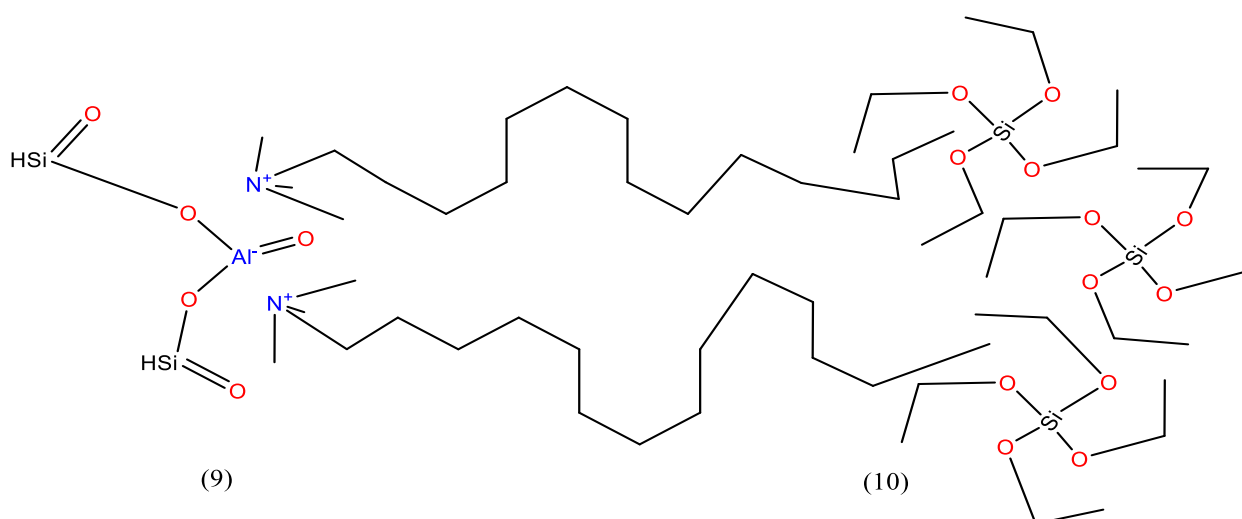
Scheme 3-6.Core shell formation

Increasing of temperature results in an addition of the amine chain to the ester of the silica, which must be avoided here. To tackle this issue, the gelation of the silica shell is done using vacuum. This allows for slow removal of the solvent, without changing the acidity of the zeolitic structure (see left side of scheme 3-6).

3.2.2   Support Material

The properties of the support material are defined in accordance to the requirements of the filter. For a typical fabrication of a ceramic filter, in which only porosity matters, economical ceramic powder can be selected as a support. In contrast, for catalytic filters, the composition of the support should be carefully selected. For instance, in NO_x catalysis, chemical elements, such as aluminum and titan oxide, provide acidity for ammonia activation, while elements, such as Sulfur and Phosphorus, inhibit the activation of ammonia ions. Therefore, support materials must be selected in order to contain the promoters and discard the poisoners [160].

The catalyst uses silica agents for the encapsulation, therefore a support material with high amounts of silica assures stability of the entire filter system. Raw material for ceramic filters mostly consists of Silica and Aluminum oxides and, to a lesser extent, of Calcium, Magnesium and Potassium, and other oxides. The following table shows a normal composition for a material used in hot gas filtration. This material was also used in this work, because it is already used in hot gas filters.

Table 3-2. Chemical composition.

Composite	Content %	Analysis method
SiO_2	70 - 75	DIN EN ISO 26845
Na_2O	10 - 15	DIN EN ISO 12677
CaO	7 - 11	
Al_2O_3	0,5 - 5	
MgO	0 - 5	
K_2O	0 - 4	
Ignition Loss	0,2	

3.2.3   Monolith Shaping

In this fabrication method the catalyst and the support materials are mixed together with the aid of an inorganic binder. On the one hand, as explained in the previous subchapter, the synthesized catalytic material remains in colloidal form. On the other hand, a dry powder is employed for the bulky structure of the filter. These two materials can easily be mixed. However, for a strong cohesion between catalyst and support, a binder is needed. Moreover, a porous template is included in order to generate the porosity of the filter after the shaping step.

i.   *Porous Structuring of a Filter*

A large polymeric chain (P123) is used in the monolith as porous agent. This chain has two hydrophilic branches and one hydrophobic one (more details are given in subchapter 2.1.3). This feature facilitates the stretching of the polar chain, when a suitable solvent is used. To achieve this, a mix of ter-Butanol and ethanol was prepared [161]. This allows to unravel the different branches during the mixing of the ceramic material and the porous template [162].

In this step a support powder material, see table 3-2, is mixed with the catalyst from chapter 3.1.3 and the promoter at a ratio of 9:1. During vigorous mixing, 18g of P123 (Pluronic 123) and 24 g of Na_2SiO_3 are added to 200ml of ethanol solution. This leads to a pasty mixture, which is partially reduced in size after an hour of stirring. Subsequently, the ethanol is removed by vacuum evaporation at room temperature.

After the removal of the ethanol, the mixture behaves more like a gel, which is extremely fluid for molding. To address this circumstance, the addition of dry support powder is needed after drying, in order to get a pasty mixture. To finish up, the mixture is continuously stirred until it turns into a dough-like consistence.

ii.   *Monolith Molding*

Giving a defined geometry requires the fabrication of a mold. This mold was designed to support the mechanical load while pressing the previously prepared mixture. The mold was also equipped with a lower and an upper drainage, in order to supply an exit for the excess of material and air in the monolith (see Drainage in figure 3-3). As shown on the right side, the mold encloses a cylindrical geometry, which fits into a commercial filter unit MSP2000 (Firm M&C GmbH), here also referred to as a monolith.

Before the loading of the prepared material, Sodium Silicate (Na_2SiO_3), an inorganic binder, is added. This has two functions. On the one hand, the silicate will increase the adhesion of the

particles during the compacting in the mold. Furthermore, the binder increases the compacting ratio, because the former reduces the material memory. In other words, the pressed body keeps its current geometry, without recovering its initial volume, which reduces the formation of pockets in the monolith during casting.

On the other hand, it will join together the big particles later during the thermal treatment. By the reaction of Sodium with organic acid, the binder promotes the formation of silica bridges between particles [84] [163]. This will be discussed in more detail in section 3.3.1.
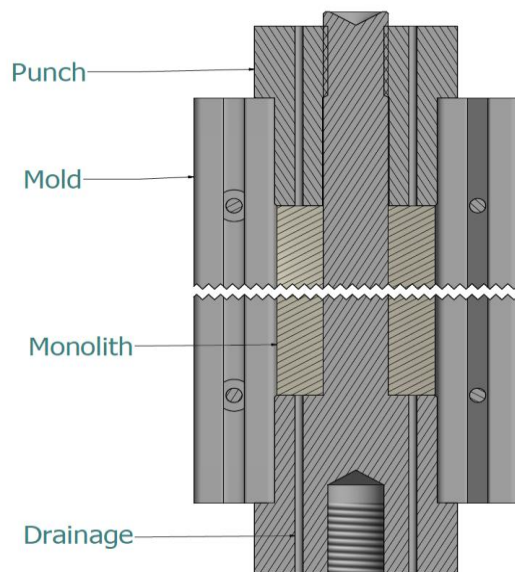
Figure 3-3. Monolith Mold.

Figure 3-4. Shaped monolith.

To conclude the shaping of the catalytic filter, the mold is loaded with the stirred mixture step by step until the high of the monolith is reached (160 mm) by applying increasing strokes of 10 MPa. During the compression it is observed that the compressed body retracts by around 3mm when the pressure is retired. This fact indicates the internal pressure capacity of the monolith, also referred to as green body [164]. Hence, at this point, when the material doesn't compress more than 3mm, the operation is stopped, because the elastic limit of the mixture is achieved.

3.3   Filter Catalyst Thermal Treatment

To finish the fabrication, a thermal treatment is applied for enabling several processes required for the finishing of the catalytic filter. First, pore opening is started by evaporation of the remaining solvent. Secondly, porous structure is shaped by the removal of the organic

template. Thirdly, the monolith structure is hardened by sintering the inorganic binder. Finally, the activity of the catalytic filter is tuned for the final test. All these processes need a certain amount of time, oxidant and temperature to be accomplished.

3.3.1 Temperature Profile

Due to the chemical complexity of the monolith, a stepped calcination curve was planned. Basically, different types of reactions are controlled by the energy supplied in the calcination chamber. Because the activation energy directly depends on the temperature in the system, a gradual increase of temperature in the thermal treatment can control the starting point of several reactions. Hence, during the calcination of the catalytic filter, crucial events, such as solvent evaporation, template combustion, silicon sintering, and catalyst activation are set to a critical temperature, as illustrated in figure 3-5.
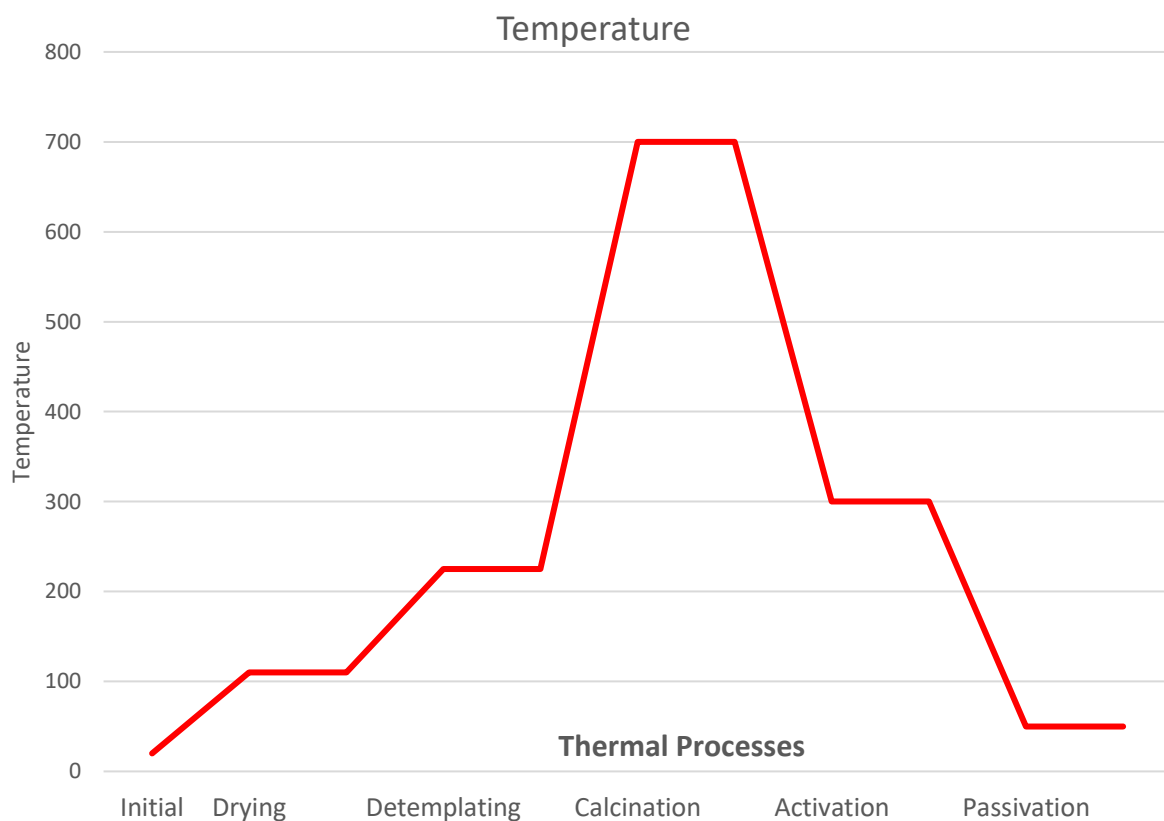
Figure 3-5. Calcination Profile.
Thermal processes during calcination of the monolith.

The key parameter for designing a calcination profile is the transition temperature of the involved material. For instance, when drying, the target temperature is related to the boiling

point of the solvents used in the synthesis. For the upcoming steps, boiling temperature and other parameters were considered, as explained below.

i. Drying

During the drying process, remaining quantities of water, alcohol and DMF are evaporated at normal pressure. Despite of the drying temperature being the lowest of the calcination process, some flaws can come up when this step is done too quickly. For example, rapid evaporation of water leads to cracks in the monolith. To deal with this, the heating rate should be slowed down, as was previously found for honeycombs [165]. A heating rate of 0.5°C per minute avoids the formation of cracks. With this approximation, the first ramp is defined to three hours, with an intermission of 30 minutes, during which the temperature has to remain at the same value. This tempering time assures the removal of residual solvent that needs more time to be released due to capillary forces.

ii. Detemplating

At the beginning of this step, the monolith contains around 10% of organic material. This is mainly the template used for shaping the porosity and the organic complex. The removal of this organic part can be summarized as an oxidation reaction, as in the reaction R 3.3. However, complete combustion of the organic material is difficult to achieve in these conditions, therefore additional gas molecules, such as carbon monoxides, aldehydes and acetones, are taken into account for the design of the flue gas treatment.

$$4CH_nO_m + (4+n-2m)O_2 \rightarrow 4CO_2 + 2nH_2O \qquad\qquad \textit{R 3.3}$$

$$12CH_nO_m + (4+3n-12m)O_2 \rightarrow 4CO + 4CH_2O + 4CH_2O_2 + (6n-8)H_2O \qquad \textit{R 3.4}$$
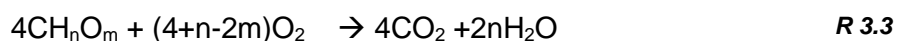
Formation of carbon monoxides, aldehydes, esters and ketones is expected, as indicated in reaction R 3.4. However, in practice, these reactions are even more complex because of the presence of a heterogeneous catalyst itself. Additionally, the activation energy of these compounds is similar, as some studies on gas kinetics have shown [166].

To overcome these issues, the removal of the template is carried out with air excess at low temperature, as shown in figure 3-5. This reduces the volatilization of long hydrocarbon chains. Additionally, the calcinating chamber is pressurized, allowing only light gases to pass to the next calcination step. To control the unreacted species, a water trap is installed at the exit for collecting the condensed gases, as illustrated in figure 3-6. This trap is activated with potassium and calcium ions, which later on will form carbonate salts.

1   Reaction chamber

2   Flanch

3   Sight glass

4   Thermoelement

5   Isolation

6   Cover

7   Condenser

8   Water trap
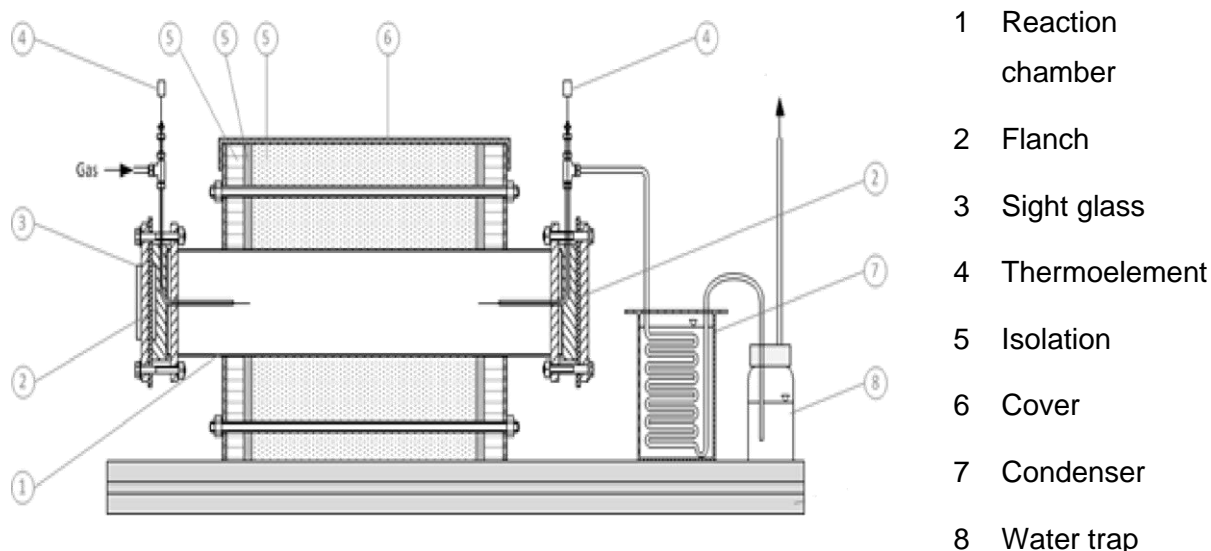
Figure 3-6. Calcination oven.

iii.   Sintering

During the removal of the template many pores are open, thus weakening the monolith structure. For the benefit of the sintering step, these opened pores allow to start the reaction of glycol from the template group with the inorganic binder (see P123 in chapter 2.3.1). Now, the binder starts to interact with the remaining polymer residues from the organic template [167]. As shown in scheme 3-7, the sintering of the binder starts through sequential redox reactions of the sodium silicate with the acidic branch of the PPG chain (Poly-propylene-glycol).
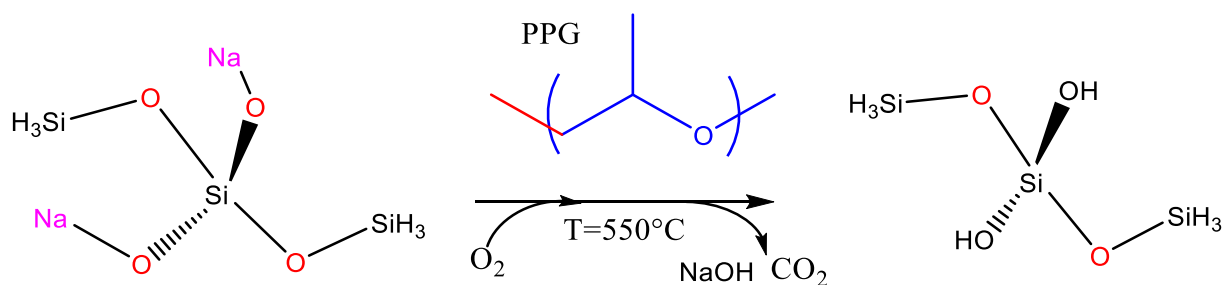
Scheme 3-7. Silanol Mechanism.

In the next step, the silanol monomers follow a condensation reaction, as shown in scheme 3-8 [168]. In summary, these silanol groups react together in a SN_2 reaction, leading to the formation of silicium-oxygen bonds, with the respective release of water. Hence, some authors call this reaction silanol condensation [169].
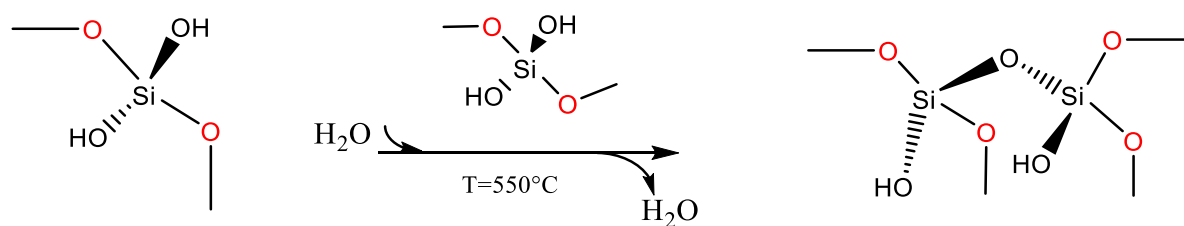
Scheme 3-8. Silanol Condensation.

iv.   Activation

The strengthening of the silica structure implies oxidation of some active centers, though. During the sintering some Copper oxides are formed, as illustrated in scheme 3-9. These CuO moieties are stable even at high temperatures [170], which is detrimental to NOx catalysis. Hence, a catalyst functionalization of the copper ions must be done again for the final use.
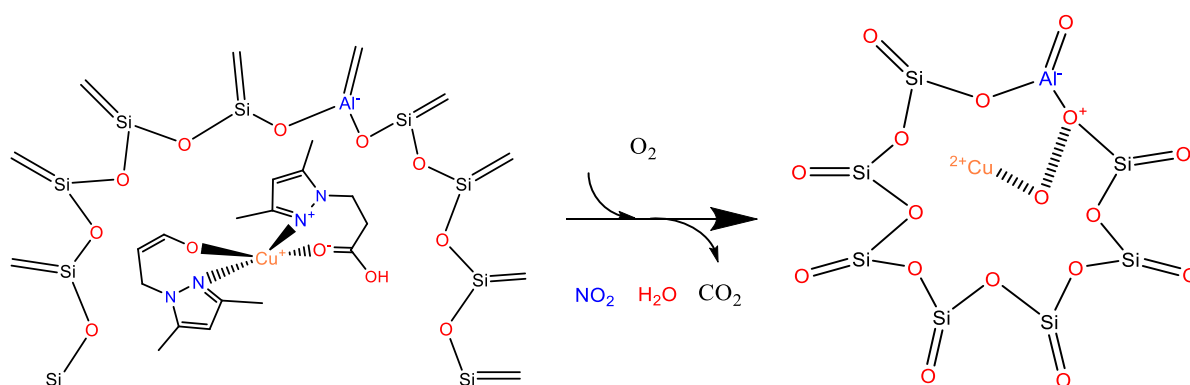
Scheme 3-9. Active center oxidation.

Since this thermal treatment restores the oxidized active center, some authors call this step the regenerating of the catalyst [171], while others refer to it as the functionalization of the catalyst [127] [172].

Basically, in this step, the oxidized catalytic centers are reduced by ammonia. Even other reductants, such as methane or propane, can be used [173]. A thermal treatment with ammonia weakens the copper oxide bond, which starts the reduction mechanism [174]. Cu(II) species are prone to coordinate with ammonia, because of their electron rich state. This leads to deprotonation of ammonia. Meanwhile, the amine is strongly bonded to Copper (see $NH_2Cu^{2+}OH$ in R 3.5). The formation of this new Bronsted acidity prepares the copper center for the reduction step. Either NO or O_2 can initiate a reduction with the amine intermediate, according to the available oxidant. As a result, the amine site decomposes, thus producing water and N_2 or NO, according to reactions R 3.6 and R 3.7.

$$NH_3 + Cu^{2+}O \leftrightarrow NH_2Cu^{2+}OH$$ *R 3.5*

$$N^{3-}H_2Cu^{2+}OH + O_2 \rightarrow Cu^+OH + N^{2+}O + H_2O$$ *R 3.6*

$$NH_2Cu^{2+}OH + NO \rightarrow Cu^+OH + N_2 + H_2O$$ *R 3.7*
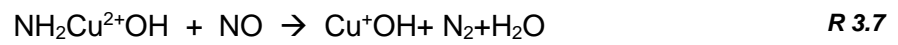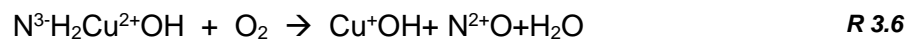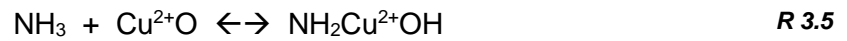
Clearly, this mechanism follows the same steps of the SCR reactions explained in subchapter 2.2.1. However, in this case, the addition of ammonia and oxidant is done separately. This avoids ammonia oxidation. Thus, some authors call this regeneration, because after the procedure, the active centers are ready to catalyze NOx again [175].

4   Testing Method for Catalytic Filters

The functionality of the catalyst was tested under SCR conditions at 200°C. In this way, the NOx conversion was used to find the optimal formulation between catalyst, support, promoter and binder. Once, the synthesis was validated, further chemical absorption analyses were carried out, as will be explained within this chapter.

The catalytic activity is measured in accordance to a protocol for SCR catalysts [66], using a test stand as illustrated in figure 4-1. Gas flow is controlled with volumetric flow controllers (MKS, MF1) for NO, NO_2, O_2, N_2 and NH_3. Water vapor is generated by a vaporizer (ASTEAM, DV4) connected in line with a gravimetric feeder. Through a bypass valve, see middle of figure 4-2, gas concentrations are measured at the input and output with an IR Gas Analyzer (MCA 04 Födisch).
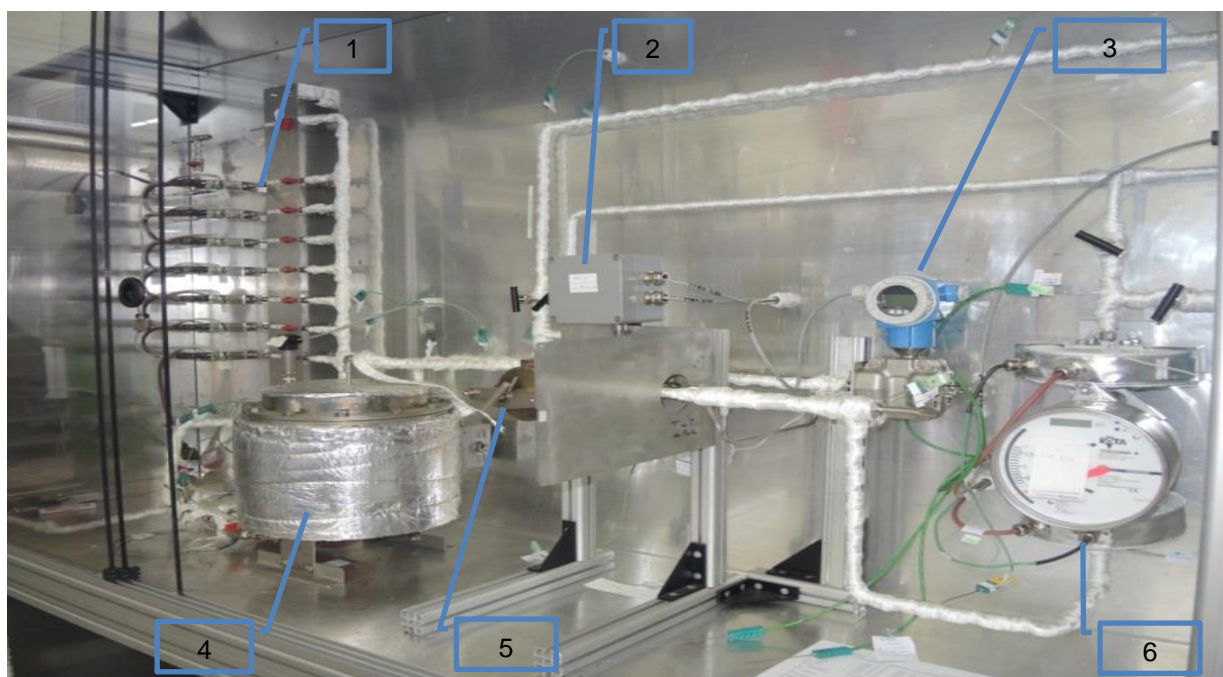
Figure 4-1. SCR test rig.
1) Gas flow controllers. 2) Heater. 3) Differential pressure measurement. 4) Mixer. 5) Reactor. 6) Flowmeter.

4.1.1   Catalytic Test Stand

This system begins with a gas mixing grid, where each individual gas has a valve and a flow controller as shown on the left side of figure 4-2. Additionally, there is an evaporation unit able to supply a flow steam of up to 32 [g/s]. The entire mixture is homogenized in a vessel to avoid condensation of water at the input of the reactor, see mixer on current figure. The mixed stream of flue gas, reductant and steam can be either sent directly to the gas analyzer or to the reactor

for further conversion, see upper right side. When the flue gas mixture moves towards the reactor, values of temperature, pressure and flow are measured at the input and the output as well.
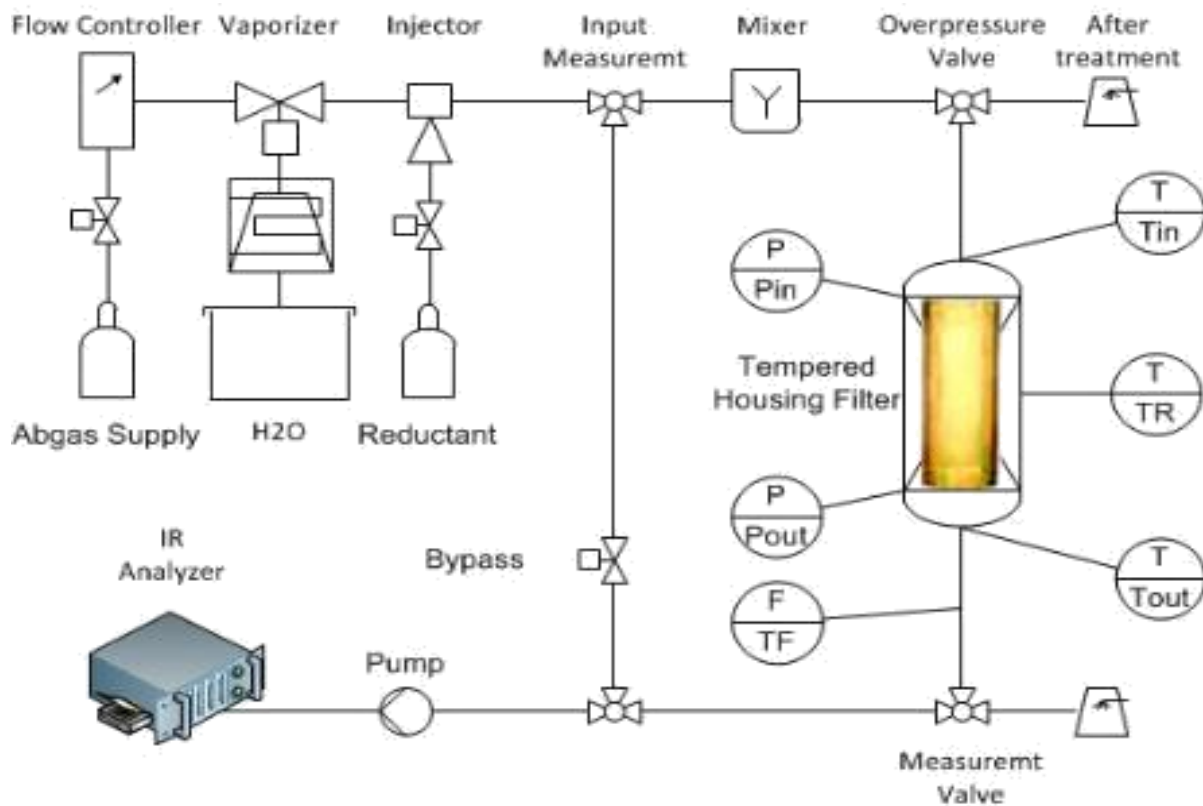
Figure 4-2. Catalyst test rig.

Regarding the SCR-testing protocol, each component of the test stand was adjusted for the generation and measurement of synthetic flue gas. In the next section, the functional components of the test standard will be described in detail.

v.   *Gas Dosing System*

The gas flow system was designed to emulate typical pollutants generated by biomass furnaces. Each bottle of gas has a pressure valve, which allows to balance the input pressure (2~3 Bar) at the Flow controller (MSK , MF1). Flow controllers are commanded by a control panel, where a desired mixture can be configurated according to the SCR protocol test. Below, the standard values for the SCR test are shown, which emulate the concentration values of exhaust gases from biofuels [176].

Table 4-1. Composition of flue gas from Biomass.

Gases	NO	NO2	NH3	O2	H2O	CO2	N2
Concentration	500 mg/Nm^3	1000 mg/Nm^3	470 mg/Nm^3	6 Vol.-%	10 Vol.-%	8 Vol.-%	Balance

vi.   *Evaporator*

Typically, biofuels contain a high amount of water, which strongly interferes with the catalyst. High humidity values can inhibit the catalyst, because of the affinity of water and ammonia, [177]. To study this effect, a variable steam generator unit was built, as illustrated in scheme 4-1.
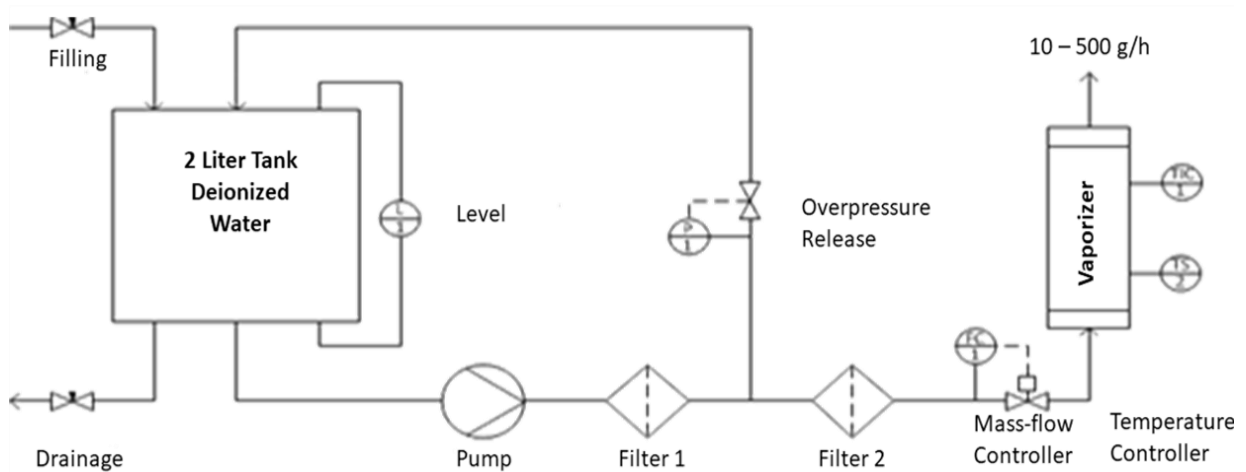
Scheme 4-1 Steam generator.

Briefly, water is recirculated continuously to a store tank through a bypass circuit, see left side. Valves V3 und V4 regulate the water flow to the evaporator. Additional filters, F1 and F2, protect the system from alkaline corrosion. Finally, water is heated up to 180°C, supplying a saturated vapor to the mixer.

vii.   Mixer

The cold gases and the steam meet at different temperatures, which might lead to condensation in the pipelines. To avoid this, a mixer unit was built as illustrated in figure 4-3. In a heated vessel, three meshes create a turbulent flow, which generate a homogenous mixture of flue gases, steam and ammonia.
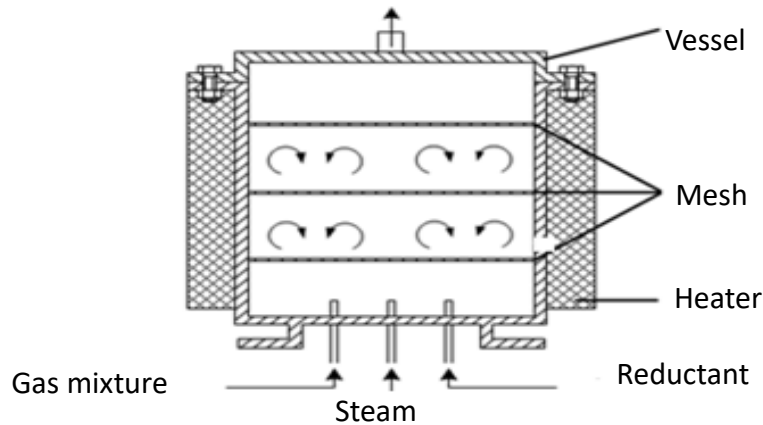
Figure 4-3. Mixer.

viii.   Reactor

In the reactor, the exhaust gas is distributed evenly along the filter, see figure 4-4. This is achieved through a shaft in the middle, which assures the internal flow across the filter, see blue arrows. This device is attached to the lid of the reactor, which facilitates the extraction and installation of the catalyst.
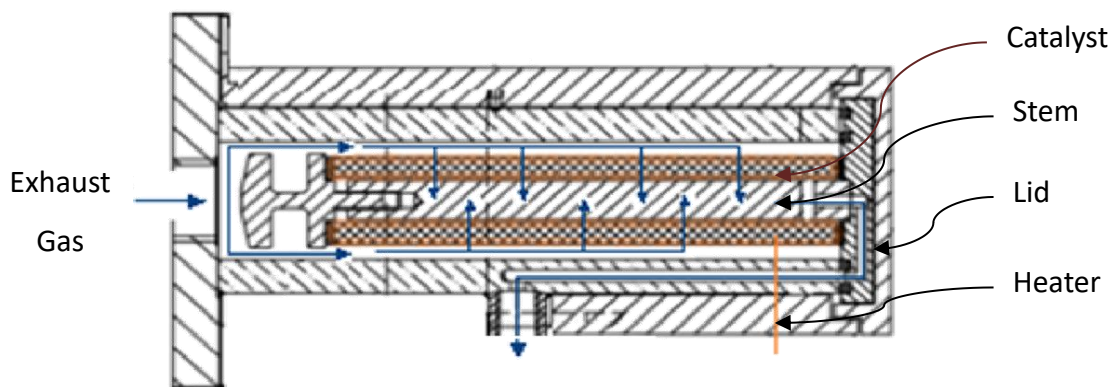
Figure 4-4. Filter reactor.

Additionally, a heating system regulates the temperature distribution around the chamber. Through this heating and isolation system it is possible to evaluate the performance from 60°C up to 300°C. Eventually, this range covers low temperature conditions in exhaust gases treatment [178].

4.2   NOx Conversion

The catalytic activity is measured in accordance to a protocol for SCR catalysis [66]. Gas concentrations are measured with an infrared gas analyzer (MCA04, Frödisch). Although concentrations of NH_3, NO, NO_2, CO_2, H_2O, O_2 are measured at input and the outlet as well, for the NO_x conversion only values of NO and NO_2 are used. The equation Eq. 4-1 is used to calculate the NOx conversion.

$$NO_x \text{ Conversion} = \left(1 - \frac{NO_{x(out)}}{NO_{x(in)}} \right)$$

Eq. 4-1

4.3   Engine Test Rig

Simulated gases give a good idea of how the catalyst operates in controlled conditions. However, in practice, concentration of pollutants, humidity and temperature are constantly changing. Hence, a test stand with an engine powered by a commercial biofuel was constructed to validate the functionality of the catalytic filter in real conditions. Additionally, the conversion of nitrate compounds – caused by nitrogen in the fuel – were evaluated by using this biofuel, which is described in detail in section 4.3-i.

The flue gases are generated by a central heating power plant (30kW) equipped with a diesel engine, which generates an exhaust gas concentration, as shown in table 4-3. Due to the high volumetric amount of exhaust gases, only a reduced stream of 5 lit/min was sent to the mixer through bypass valves, see left side in scheme 4-2.
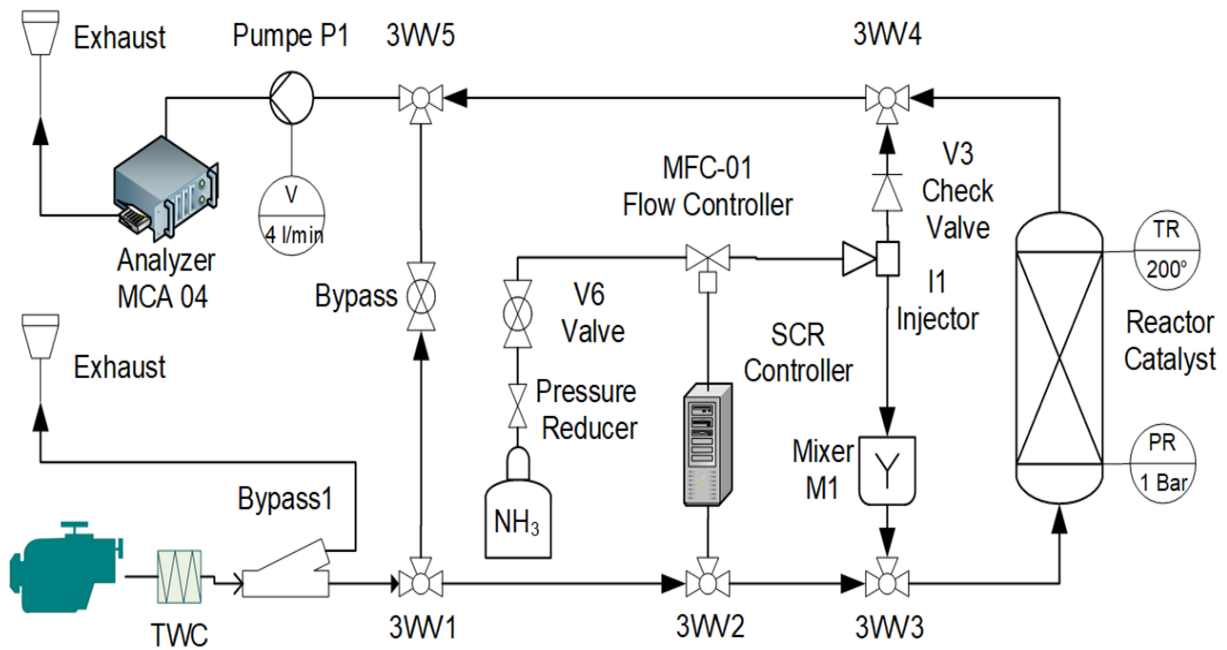
Scheme 4-2. Motor catalytic test stand

The middle of scheme 4-2 shows that ammonia is fed to the mixer by a volumetric flow controller (MKS, MF1). Additionally, valves V3 and 3WV4 facilitate the calibration of ammonia in the stream. As explained previously in section 4.1.1, a mixer (M1) homogenizes the flue gas stream and the injected ammonia.

By operation of valves 3WV1 and 3WV3, the mixed stream is pushed to the reactor, where temperature and pressure are controlled, as sown in figure 4-2. Finally, the catalyzed stream is measured at the analyzer MCA 04, see upper left of scheme 4-2.

i.   Biofuel

A standard commercial biofuel, also named FAME (Fatty Acid Methyl Ester), was used for these experiments [179]. Fundamental specifications are given below, whereas a more detailed chemical description is found in the annex 9.1.

Table 4-2. Thermal properties of biofuel FAME.

Fuel	Density (15°C)[Kg/m^3]	LHV [MJ/Kg]	Water Content [wt.%]	Ash Content [wt.%]
FAME	883,0	37,1	0,05	<0,1

ii.   Exhaust Gas

The diesel motor has a DOC (Diesel Oxidation Catalyst) close to the exhaust gas collector, which reduces emissions of CO and HC and NOx simultaneously [180]. Despite the fact that a NO_x reduction step is already implemented, NOx emission values reach up to 570 mg/m^3 after the DOC. Therefore, a second NOx control system is required to set emission values according to German emission law. For small CHP (Central Heating Power), emission limits are defined by the TA Luft, as the lower row of table 4-2 indicates.

Table 4-3. Emission measurement at CHP unit.

Gases	CO	NO_x	SO2	HCHO
Units	[mg/m³]	[mg/m³]	[mg/m³]	[mg/m³]
Biodiesel	79,9	1356,9	19,7	3,1
Limit values TA Luft	300	500	31	60

HC and CO emissions are another relevant aspect of automotive exhaust gas. Although an oxidation catalyst may reduce these emissions to acceptable values, the remaining unburned hydrocarbons form soot at the cool zone of the SCR system. Therefore, the effect of soot accumulation on the catalytic filter was also reviewed in this work, see figure 5-6 and figure 5-7.

5   Analysis of Performance

De-NOx performance was used as a screening parameter for the optimization and analysis of the catalytic filter. To optimize the synthesis, the catalytic filters were initially tested at 200°C under standard SCR condition in the test rig of figure 4-2. Through this basic method, key material compounds of the catalyst were screened and then studied in more detail.

To disclose the SCR performance regarding temperature, six catalysts were synthesized with slight changes in the support material in order to explore adsorption properties. Moreover, studies of water and oxygen effects in the flue gas were done, for the validation of the catalyst under extreme conditions.

Finally, a catalyst was tested in real-world conditions with flue gas emission from biofuel, see section 4.3. Besides NO_x performance, stability and passive reduction were investigated.

5.1.1   Functionality Test

The development of the catalytic filter involves numerous chemical reactions, which are difficult to evaluate stepwise. Therefore, a straight-fordward approach was used to screen the preparation method. In this approach, different ligands of copper complexes were synthesized as previously explained in section 3.1.2. These complexes were encapsulated and sintered with the same filter support for reasons of comparability, see section 2.2.3.

Several ligands can be coordinated with copper metal, however, for this work mainly pyrazole and imidazole ligands were used. These ligands bind strongly to copper and are stable under acidic conditions, which is desired during the synthesis of the support [181]. In figure 5-1, black bars illustrate the De-NO_x performance of several catalysts, which were synthetized with imides and azoles during the active center synthesis.

The influence of these ligands, also named templates, on the performance of a catalytic filter is profound. Therefore, copper complexes are widely researched by several teams nowadays [182], [42]. Despite these efforts, the reaction path of copper ions with organic molecules is still a hot research topic [138][183]. To overcome this complicated scenario, the evaluation of a suitable template for the encapsulation of the copper center was assessed by a functionality test. In this test, NO_x conversion of different catalysts was evaluated at 200°C using the test rig, see figure 4-2.
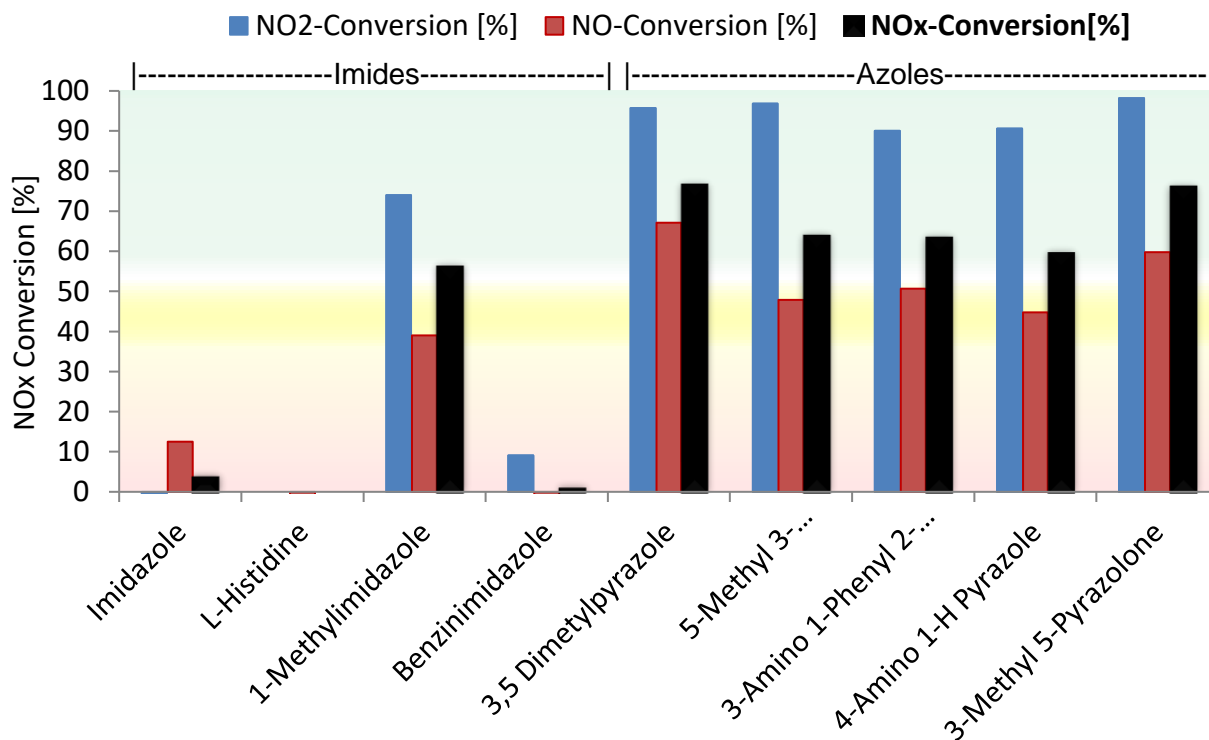
Figure 5-1. De-NOx test at 200°C.
Test Conditions: NO=1000ppm, NH3=1000ppm, O2 = 6%, H2O=10%, N2=rest.

A functionality test was set up for 9 catalysts, which only differ in the template for the active center. For around one hour, the catalyst was fed with a gas mixture of NO, NO_2 , NH_3, CO_2, H_2O, O_2 and N_2 ,as previously described in section 4.1.1. To conclude the experiment, NO_x conversion was calculated with Eq. 4-1 and summarized in figure 5-1.

From the previous graph it can be concluded that catalysts based on imidazole templates yield low conversion rates in comparison with the pyrazoles. In consequence, more pyrazol based catalysts (5 samples) were synthetized in order to explore the performance of additional functional groups. This observation indicates that the copper-azol bond remained more stable during the synthesis than the imide bond [148]. However, a precise explanation requires further spectroscopy experiments.

The figure 5-1 shows that all the pyrazole-catalysts, also called azol-based, are in the green area. This area stands for NO_x conversions over 600 mg/m^3, when the exhaust flue gas contains around 1300mg/m^3. In fact, NO_x concentration of motor exhaust gases are below 800mg/m^3, therefore these tested catalysts may fulfill current standards for NO_x emissions for power plants [25].

Moreover, variation of functional groups in the template (akyls, amines) doesn't notably affect the performance of NO$_x$ reduction. For this reason, a low cost and environmentally friendly pyrazole template was used in the synthesis. Therefore, further copper complexes were coordinated with Dimethylpyrazole, because of its commercial availability and low environmental impact.

5.1.2   Support Effect

Active metal oxides enable adsorption and decomposition of NO$_x$. Hence, after setting the suitable template, sintered filter catalysts were fabricated with different promoting metal oxides, see figure below. In this way, adsorption of NO$_x$ and NH$_3$ was explored at low temperatures, see Table 6-1. Each catalyst has a notation that starts with the element notation of the active center – Cu –, followed by the metal oxide promoter. Oxygen atoms are neglected for the sake of understanding, see lower side of figure 5-2. The third notation indicates the fabrication method, for instance, 'S' indicates sintering. The following figure illustrates NO$_x$ conversion at 200°C of the fabricated catalyst.
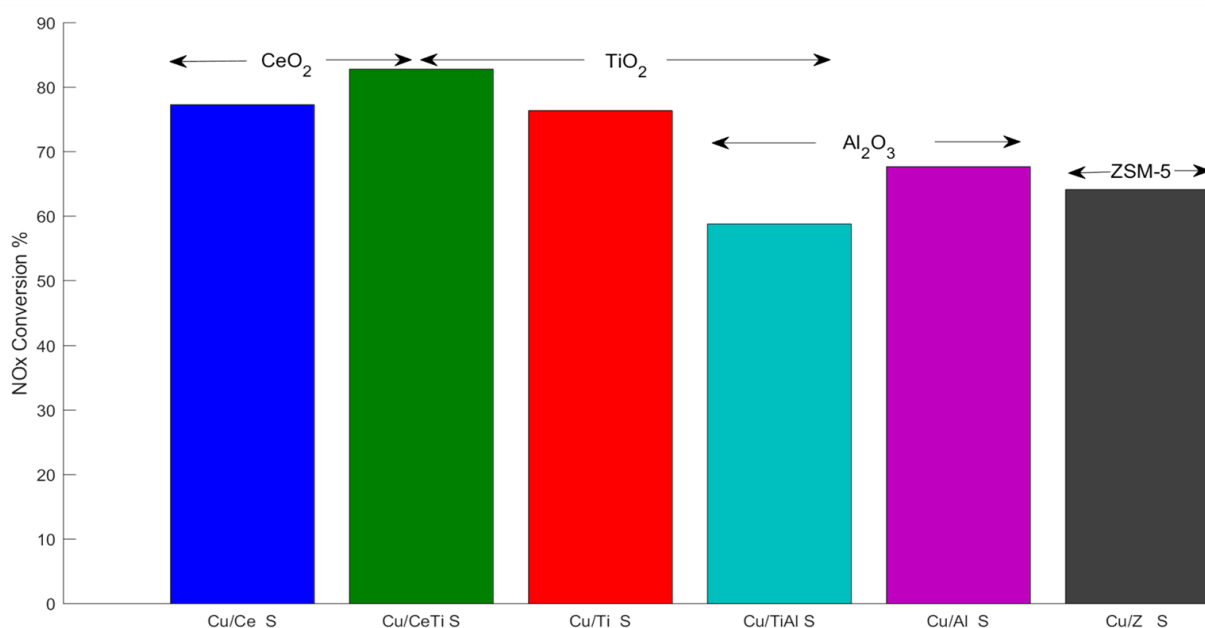
Figure 5-2. NOx conversion of different supported catalytic filters.
Test Conditions: same as figure 5-1.

Regarding the promoters, the results show that TiO$_2$ and CeO$_2$ improve the absorption of NO$_x$ more strongly than Al$_2$O$_3$, which confirms observations already published [184],[185]. Conversely, the addition of NH$_3$ absorbers, such as zeolite ZSM-5, doesn't help significantly,

as seen in the performance of Cu/Z-S. This fact confirms previously reported results, which support that at a low temperature range, NO_x absorbers are crucial for the SCR reaction [45],[186].

5.1.3 Temperature Effect

In most of the cases, the temperature performance determines the applicability of the catalyst, which is defined by the activation temperature. A low activation temperature means a more efficient catalyst, because less energy is required to overcome the operative state [187]. Once this temperature value, also named $T_{ligth-off}$, is surpassed, the conversion accelerates according to mass transfer properties and the amount of catalytic material. In consequence, the thermal behavior will be studied in detail in this section.

To see the temperature performance of the catalyst, the test was done under auto thermal conditions. This means, the reactor was heated up to 250°C until stable conditions for measurement were observed. Subsequently, the heating supply was switched off, which removed external influence of the heaters during the temperature run.

During the cooling of the system, the catalyst worked under similar conditions as an industrial one, where no heating is supplied for the SCR system. When the system reaches 120°C, the reactor is heated again to avoid water condensation and formation of nitrate salts [188]. Finally, NO_x conversion of the 'fresh' catalyst – noted as 'F' – is calculated as shown in eq. 4-1.
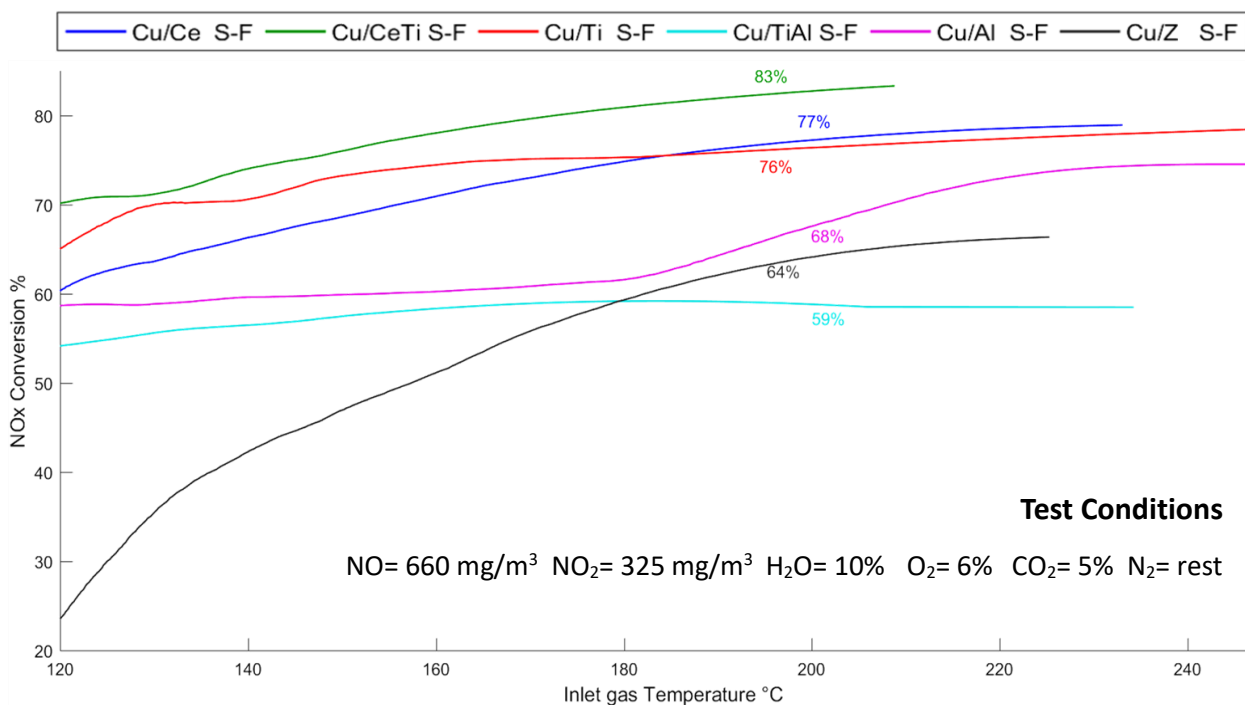
Figure 5-3. NOx Conversion vs. Temperature.

As shown in figure 5-3, NO_x conversion increases slightly, proportionally to the temperature profile in all catalysts tested. Nevertheless, catalysts Cu/Ce S-F, Cu/Ti and Cu/TiAl S-F became stable after 220°C, indicating that these catalysts were already saturated. It means that active centers of these catalysts are already occupied. Thus, further increase of temperature does not noticeably increase mass conversion in the catalyst.

Despite the fact that sintered catalysts did not achieve total conversion, their mass conversion values are above 700mg/m^3 for NOx. This NO_x conversion value is enough to clean flue gases under the limit of 250mg/m^3, which is the actual limit for combustion of biomass [189].

Regarding activation temperature ($T_{Light-off}$), almost all the catalysts are already activated above 120°C. In fact, the sintered catalysts are able to work at a low temperature range, which makes them promising for industrial application.

In the case of Cu/Z S-F, the addition of ZMS-5 in the support material lessens the temperature performance. This effect is also perceived in the catalysts Cu/TiAl and Cu/Al, which showed less activity than the Cu/Ce and Cu/CeTi. This infers that aluminum oxide in the support results in reduction of performance. However, in filtration experiments aluminum supported catalysts were more mechanically stable than the other ones.

5.1.4 Water Influence on Conversion

SCR reactions (R 1.5 and R 1.6) yield water as effect of the oxidation of ammonia by NO, therefore presence of water shifts the reaction backward, which reduces catalyst conversion. Moreover, H_2O and NH_3 tend to occupy similar active sites on ceramic materials [190]. Therefore, absorption of water molecules on the active sites inhibits SCR reaction in oxidative conditions [191].

Furthermore, humidity of the flue gases is directly related to humidity in the feed material of the furnace. Eventually, flue gases from biomass combustion contain up to 20% water. Thus, the chemistry between the gases NO and NH_3 was investigated under wet conditions, in order to quantify the effects of humidity on the developed catalyst. By doing this, water sensibility of the catalyst can be estimated to define operation limits of the firing system.

The water sensibility test was run at a constant temperature of 200°C and conditions as shown in figure 5-4. Water feeding changed the temperature in the reactor immediately, because of the high calorific value of water. Therefore, a large stabilization lapsus was needed during the water feeding. Even though this experiment was treated extremally carefully, the added water took some of the available energy of the system, thus causing a temperature decrease as seen in figure 5-4.

Concerning NO_x conversion, water proportionally lowers the SCR reaction until the water content overpasses the concentration of NO and NH_3 manifold. This means that in normal conditions (above 2% water content), humidity of the feedstock has a constant negative effect. This effect decreases NO_x conversion up to 40%, which indicates that at least 40% of absorption sites in the catalyst are occupied by water.
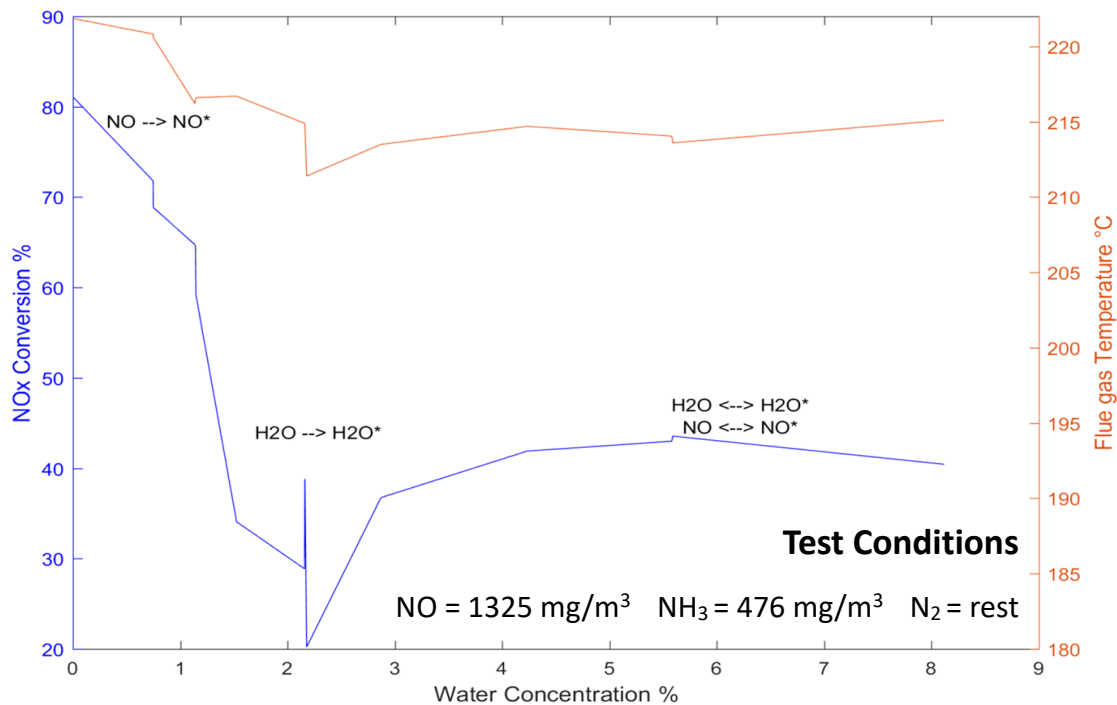
Figure 5-4. Water sensibility test on catalyst Cu/CeTi.

From the experiment it can be concluded that water adsorption on the catalyst has a limit, as seen above. Up to 2% of water is absorbed and desorbed on the catalyst. Therefore, small amounts of water compete with NO molecules for adsorption sites, while higher values settle down on the catalyst. In consequence, when the water concentration exceeds NO and NH_3 concentrations manifold, water molecules conquer most of the hydrophilic places on the substrate. That means that NO conversion in wet condition mostly occurs at Lewis sites, because water preferably binds at Bronsted sites [192], [193].

5.1.5   Oxygen Effect

Biomass combustion is also carried out on oxygen excess, because of the heterogeneity of the solid fuel. Moreover, secondary burners inject additional air to complete combustion. Hence, flue gases from biomass feeds are over 10% in most of the cases. This excess of oxygen favors the oxidations of ammonia to NO, which plays against NOx conversion. Besides, oxygen radicals compete with nitrogen oxides for absorption sites during SCR reactions. For

this reason, the sensibility of the catalyst toward changes of oxygen concentration was also analyzed, see figure 5-5.

Although the experiment was planned to observe negative effects, positive effects were more noticeable. As shown in figure 5-5, oxygen promotes NOx conversion. In fact, the catalyst is activated when oxygen concentration surpasses 1%. This means that intermediate oxidation of NO to NO_2 promotes the SCR mechanism in this catalyst.

$$2\,NO \;+\; O_2 \;\rightarrow\; 2\,NO_2 \qquad\qquad\qquad \textbf{\textit{R 5.1}}$$

$$6\,NO_2 +\; 8\,NH_3 \;\rightarrow\; 7\,N_2 +\; 12\,H_2O \qquad\qquad \textbf{\textit{R 5.2}}$$
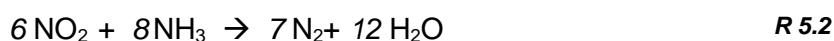
This oxidation effect has already been studied on LNT (Lean NO Trap) catalysts [186], [194]. On these catalysts, NO is absorbed when the catalyst is cold, which is also called cold start. When the catalyst warms up, NO and NO_2 are released and then treated on the SCR catalyst.

Because a mix of NO_2 and NO required less activation energy than NO alone [195], NO absorbers on a SCR catalyst are called promoters in some cases [196]. This promotional effect was also used and tested in this work. By doing so, large amounts of NO_x absorbers were integrated on the catalytic filter, which noticeably promotes the SCR performance in normal operation modus.

Test Conditions

NO = 1325 mg/m³   NH₃ = 476 mg/m³   N₂= rest
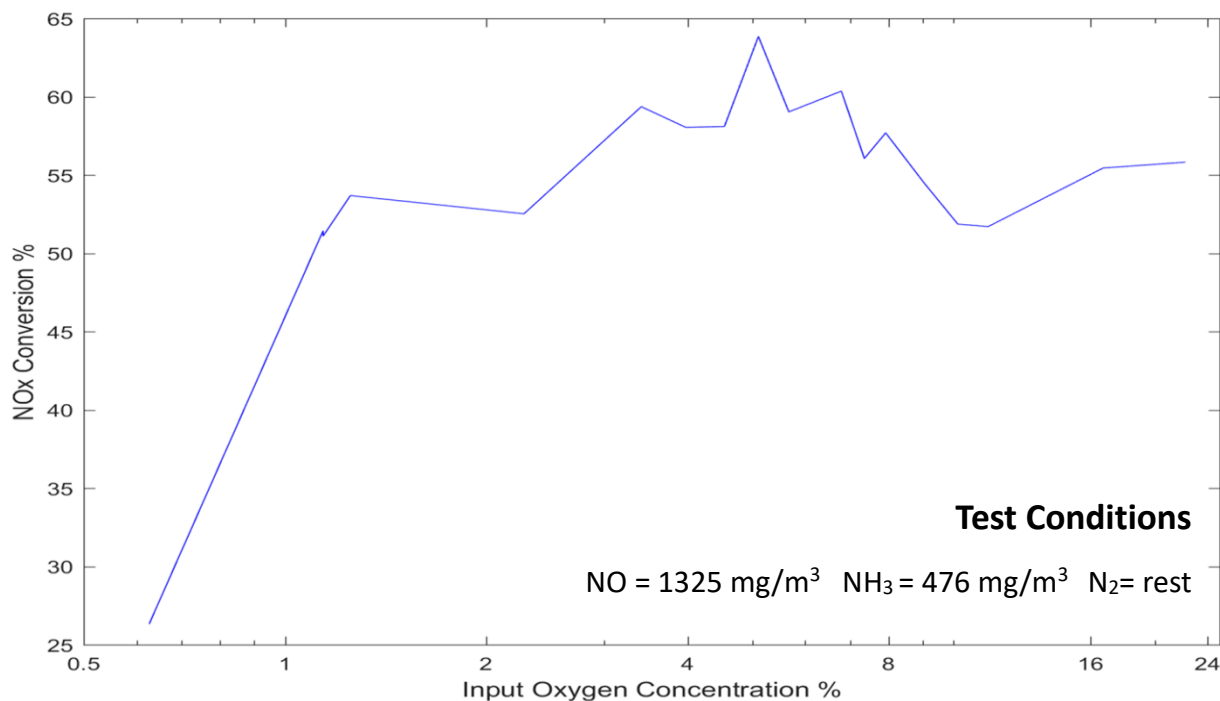
Figure 5-5. Oxygen effect on NOx conversion.

Similarly, as water, oxygen concentration beyond 2% doesn't have any strong effect on the catalyst. This indicates that   excess of oxygen in the combustion does not affect the performance of the catalyst, at least in common lean conditions (>10%). Therefore, these catalysts are suitable for NO_x reduction at biomass furnaces.

5.2   NOx Emission Reduction of Biofuels

In biofuel combustion, NO_x formation in an internal combustion engine (IC) strongly differs due to several factors. For instance, ignition delay, nitrogen content and oxygen-containing groups are some unwanted properties in biofuels, which speed up the formation of pollutants. In consequence, exhaust gases are rich in oxygen and moisture and dust particles. Particularly at diesel engines, unburned hydrocarbon and soot particles accompany NOx emissions, which considerably changes the SCR mechanism in these systems. These conditions generate a real working scenario for catalytic filters. Therefore, a motor test stand was built as described previously in section 4.3.

Soot filtration and NO_x reduction were tested in a Cu/Ce-Ti catalyst, which initially looks as figure 5-6 illustrates. Additionally, pressure drop was constantly measured in order to analyze the soot effect on the filter. As seen in figure 5-7, soot and hydrocarbon are found on the catalyst, after a couple of operation hours. Although this soot layer results in a pressure drop, the NO_x conversion was not affected at all, as shown in figure 5-8. Eventually, adjustment in the injection of ammonia was needed in order to compensate the reducing effect of soot.
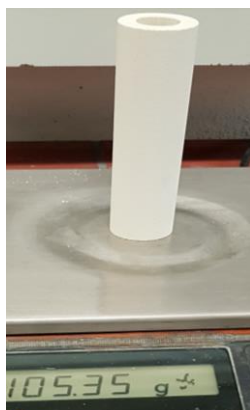
Figure 5-6. New Catalytic Filter   *Figure 5-7. Catalytic filter after 3 operation hours*
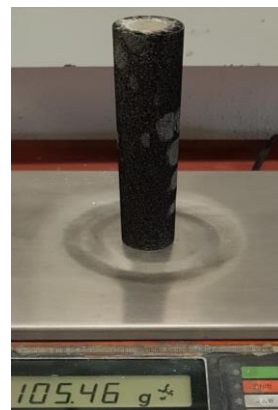
5.2.1   Temperature Performance

In comparison with the emulated furnace exhaust gas, the soot deposition changed the kinetics of the catalyst in this experiment. Presumably, at low temperatures soot condensates in the

porous media, which reduces the mass transfer in the catalyst. This might explain the small valley at 200°C, where soot particles start to volatize, releasing absorbed NO [197].
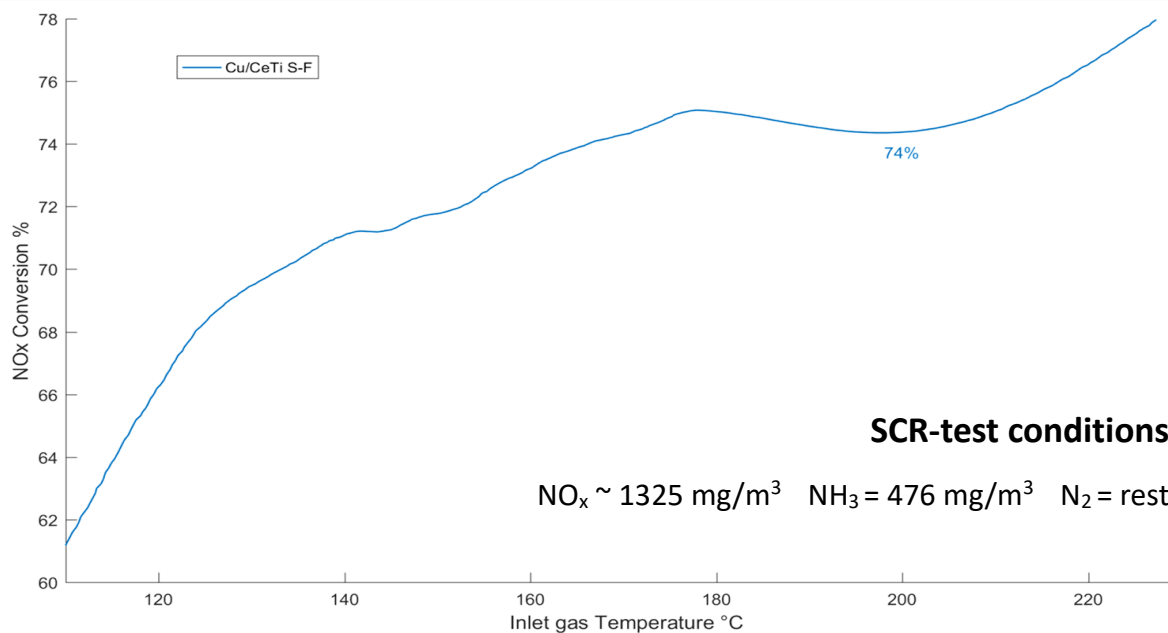
Figure 5-8. NOx conversion of catalyst Cu/CeTi.

Complete exhaust gas compositions are described in 4.3.

Above 210°C NO_x conversion takes a growing tendency, which can be evidence of soot activation. Further increase of temperature will achieve higher conversion in normal conditions. Unfortunately, the system is not capable to heat beyond 250°C. This indicates that efficient NO_x conversion at low temperature requires previous full conversion of hydrocarbon at the oxidative catalyst, also known as 3-Way or DOC catalyst. Otherwise, the conversion is limited due to soot clogging.

5.2.2   Stability Test

Laboratory tests are usually run for a few hours under stable conditions, because of the availability of the laboratory and its operational cost. Conversely, for practical applications, the catalyst should work more than 120.000 hours and respond to changes of gas concentration and dust content. In some cases, these long-time tests are shortened through thermal aging, where the catalyst is tested for a couple of days at over 700°C [198]. However, for low temperature catalysts, thermal aging is not an option because of the big temperature difference.

For this work, a stability test was prepared for two days, in order to get a general insight into the long-time behavior of the catalyst under variable conditions. To do so, SCR reduction was performed over 36 hours with the motor stand depicted in scheme 4-2. Temperature, NH_3 and NO concentration were varied as lower part of figure 5-9 shows.

Initially, temperature was set to 250°C in order to volatize deposited soot. After six hours of conversion, ammonia was varied in order to find the optimal conversion, without any ammonia slip. After 18 hours of operation, the lower temperature range was tested for around 10 hours. At hour 28, the cold-start behavior of the catalyst was evaluated by ranging the temperature from 100°C to 250°C. Finally, during the last 6 hours, NO_x reduction with soot was tested for analysis of the catalyst under passive conditions.
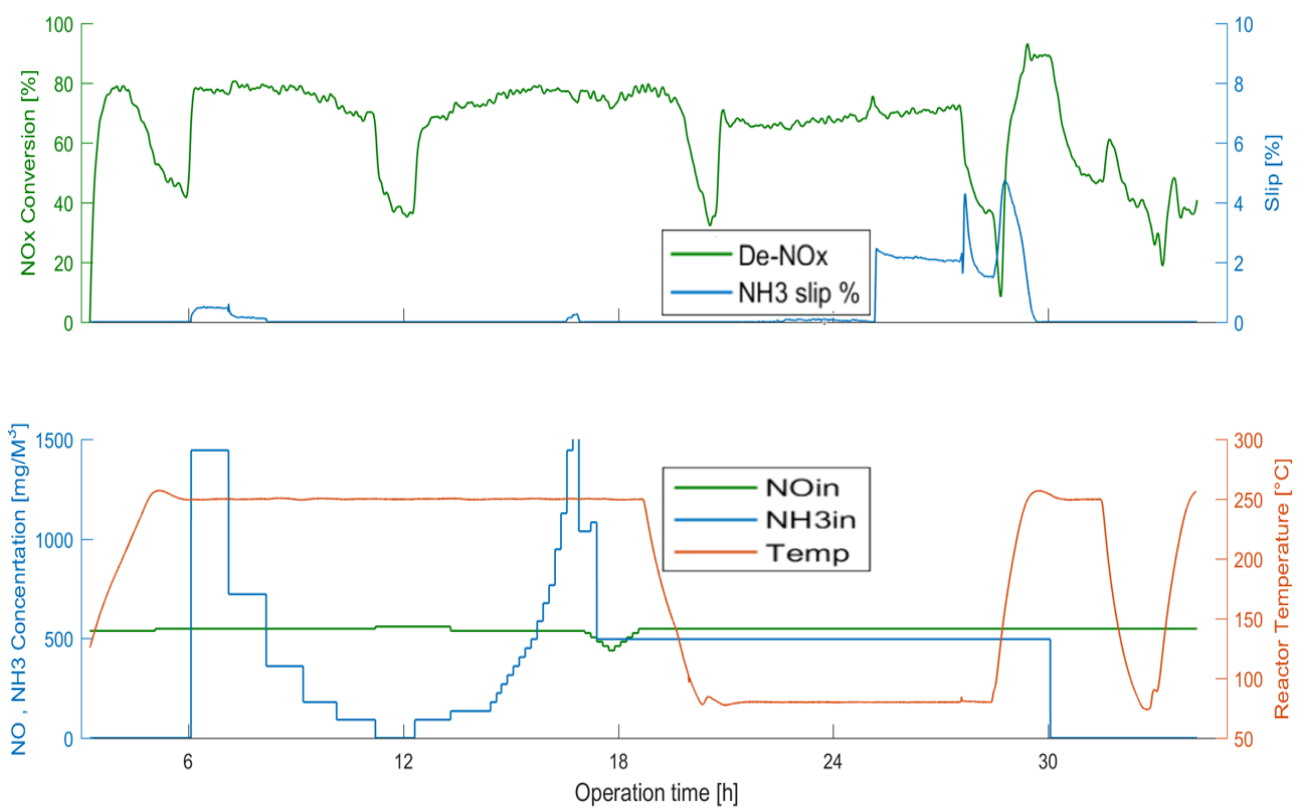
Figure 5-9. Stability test.
Upper figure: NO_x conversion and NH_3 slip. Lower figure: Temperature in the reactor and NO and NH_3 concentration at the exhaust gas.

i.   Ammonia Consumption

Above 200°C soot volatilization creates a reducible environment on the catalysts, which lessens the ammonia consumption [199]. Even though this positively impacts the SCR reaction, new consumption of ammonia cannot be directly calculated, because of the

uncertainty of soot deposition. Therefore, in the first part of the experiment, the ammonia injection was gradually varied as shown on the left side of figure 5-9.

Lack of ammonia lowers the conversion by 40%, which indicates that soot alone converts around 224 mg/m^3 of NO. Nevertheless, better conversions are attained with ammonia concentrations above 200 mg/m^3. In fact, the best performance of the catalyst is achieved around the stoichiometric ratio of ammonia and NO, which is around 500 mg/m^3. Therefore, for low temperature applications ammonia is definitely necessary to accomplish standard regulations [200].

ii.   Ammonia Slip

Theoretically, over stoichiometric feed of ammonia results in a NH_3 slip, however, here it was seen when ammonia was three times above the stoichiometric ratio. Moreover, during cooling of the catalyst, around hour 19, no ammonia slip was observed in the flue gas. Therefore, the catalyst oxidizes ammonia completely, when the molar ration NO_x-NH_3 is close to 1. This confirms the acidity of the catalyst due to the copper loading [201]. However, at the cold start, ammonia oxidation is inhibited by ammonium salts until the catalyst overpasses 150°C, see hour 29 in previous figure.

A possible clarification lies in the formation of ammonium nitrate salts, which strongly bind on the catalyst. These ammonium nitrates inhibit the catalyst below 120°C, as a combined effect with condensated water [202]. Similar behavior was seen on diesel particle filter. In this study, NH_4NO_3 were bounded to soot particles at low temperatures. Then, during heat increase, nitrate salts decompose to NH_3 and NO_2 or N_2O [203].

iii.   Cold Start

Across the different tests carried out on the catalyst Cu/CeTi, cold start was the most critical one, where the weakness of the catalyst was exposed. In figure 5-10, the NO_x conversion drastically sinks due to the accumulation of soot and nitrates. During the cold start, ammonia nitrate, which is bounded to water, is decomposed first. This might explain the first peak of NH_3 and NO_2 at 8:15 AM in the figure below. In fact, the catalyst was releasing previously stored NO_2, thus NO_x conversion dramatically decays in this period, see orange line in figure 5-9.

Further heating promotes the decomposition of ammonium nitrate bounded to soot particles, see second NH_3 and NO_2 peak at 9:12 AM. During this period, high values of NO_2 are emitted, which agrees with the observation of [204]. After the temperature rose over 150°C, the catalyst became active, which led to the regeneration of the aftertreatment system.
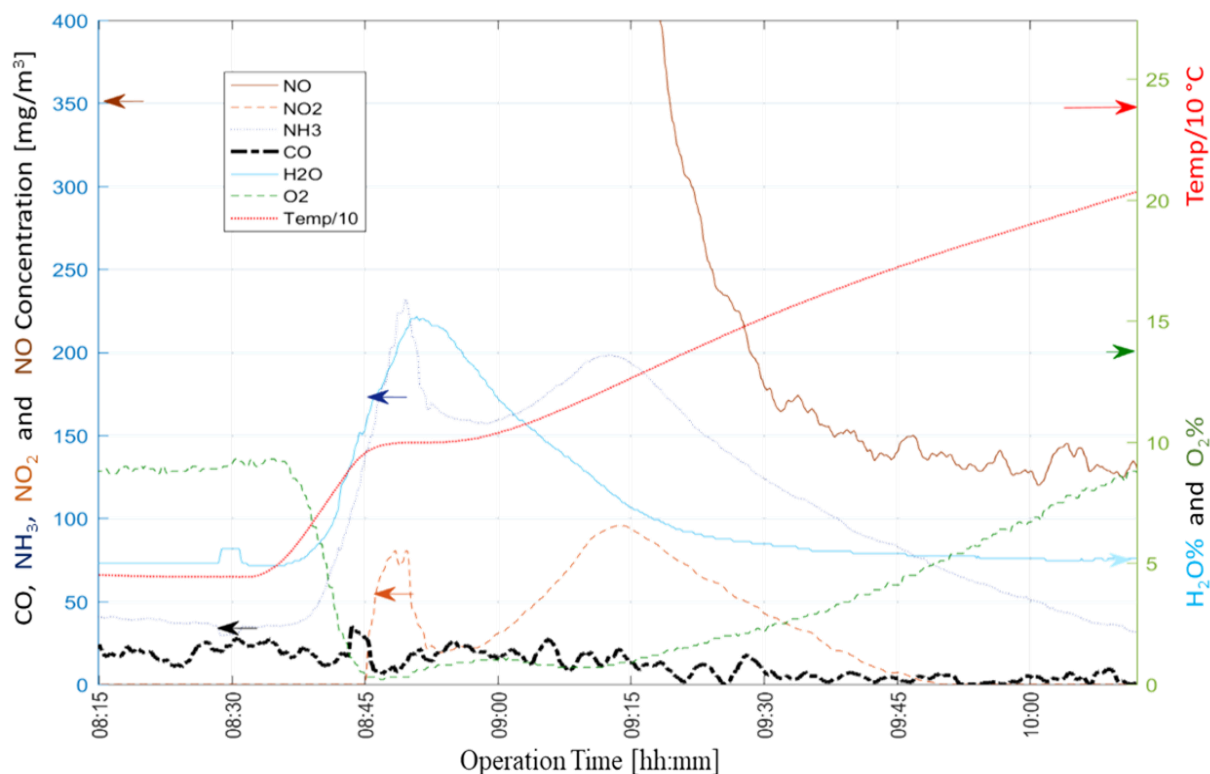
Figure 5-10. Catalytic behavior of catalyst Cu/Ce at cold start.

iv.   Soot Oxidation

NO_x conversion without ammonia achieved 40 %, which resulted in ~250mg/m^3 of NOx. This might be plausible in some applications. To see the long-term conversion by soot, the last part of the stability experiment was used to see the ammonia-free behavior of the catalyst.

At the max temperature of the system (250°C), NOx conversion by soot was between 35% and 20% efficient, when ammonia was cut off. Moreover, at low temperature the conversion decayed below 20%, thus heating of the catalyst was required at this point. These findings indicate sensibility of the active center toward hydrocarbon, which might be useful for low requirement applications. To shed light on this, a detailed analysis of soot oxidation is depicted in chapter 6.2.3, where soot oxidation on the catalyst is kinetically studied .

5.3   Overview of Performance

The performance of this newly fabricated catalyst was described in this chapter. In general, NO_x conversion of over 80% was achieved at low temperature range (120°C to 250°C). These results validated the fabrication of catalysts by the encapsulation method as an alternative in contrast to impregnation of catalysts. Moreover, performance of the catalytic filter under

particle loaded exhaust gases was successfully tested. Even though, accumulation of soot on the external area of the filter reduced by about 40% NO_x conversion during starting condition. Fortunately, after heat regeneration the catalyst was reactivated again, as seen in figure 5-9. This result shows the convenience of catalytic filters, which are not deactivated in dusty environments due to their porous structure.

6   Analysis of the Catalytic Filter

Functional SCR testing validates the fabrication process of the catalytic filter to some extent. However, additional analysis of the internal chemistry was done, in order to give insights into the SCR mechanisms and the crystal structure of the catalytic filter. Due to the complexity of the material in the catalyst, basic elemental and spectroscopy analysis were run on a sample of the catalyst Cu/Ce-Ti, which performed best. Finally, a feedback on the synthesis is postulated, with the goal of further improving the synthesis process (see section 2.2.1.).

6.1   Material Characterization

During the development of the catalyst, variations in the material composition were tested so as to increase De-NOx performance at low temperature. From these experiments, the variation of promoters in the support produced more significant changes on the performance than the active material, as previously studied in section 5.1.2. Therefore, through the analysis of the catalyst, the characterization of the support and the active elements are treated simultaneously.

6.1.1   Elemental Composition

Elemental composition of the catalyst was measured using EDX analysis (LEO 1450VP Field Emission SEM coupled with Oxford EDX). The elemental parameters of each catalyst are shown in the next table (see table 6-1). As previously explained, the first element in the notation stands for the active element, while the second accounts for the promoter used in each case. Catalyst, promoter and support percentages are shown in table 6-1. In the elemental composition row, the third term 'FM' accounts for the chemical elements found in the raw materials for monolith fabrication, which are mostly inert ceramic oxides. These unreactive materials of the support, such as SiO_2, Al_2O_3, NaO and CaO among others, are referred to as "rest". Additional details of the support material are found in table 3-2.

The pictures in table 6-1 show the final appearance of the catalytical filter after testing under SCR and dust conditions. Elemental analysis is done with a small powdery sample obtained after thermal treatment. To get a global overview, 30 samples, six of each monolith, were collected. Three of them were taken along the outer surface and the others along the internal surface, in order to see the catalyst distribution on the whole monolith. Finally, the 6 values of each monolith were averaged, giving a single value for each monolith.

Table 6-1. Summary of fabricated filter catalyst.

Name	Cu/Ce-S	Cu/Ti-S	Cu/Al-S	Cu/Z-S	Cu/CeTi-S
Elemental Composition	Cu/Ce/FM	Cu/Ti/FM	Cu/Al/FM	Cu/Z/FM	Cu/Ce-Ti/FM
Mass %	0.9/10/rest	1.9/8.5/rest	1.7/10/rest	1/18/rest	0.2/6.3/rest
BET Surface (m^2/g)	58	77	56	88	27
Porosity (ε)	0.62	0.72	0.57	0.65	0.67

Variation of elemental composition among the different spots was minimal, see annex. This confirms the effectiveness of mixing during the casting process (see 3.2.3). An interesting fact comes from the different copper mass composition of each catalyst. A similar mass percentage was expected for each case, however, catalysts with CeO_2 and ZSM-5 as promoters showed less bulk copper. A possible explanation lies in the measurement method. Generally, the EDX method measures elements on surfaces, thus bounded elements in the bulk material are difficult to identify, because the X ray sensor reads mainly the scattering from the first nanometer layer. In consequence, catalysts show less superficial species of copper oxides when they are integrated with bimetallic oxide (CeO_2) or encapsulated with ZSM-5.

6.1.2 Porous Structure

Porosity and surface area were estimated with nitrogen adsorption isotherms by using a porosity analyzer (Micromeritics ASAP 2020). One representative sample of each monolith (ø 10mm X 10mm large) was fabricated using a similar synthesis as previously described but with a small dimension mold for fitting on the measurement cell. In table 6-1, the porosity and BET

surface of each monolith are summarized. Additional measurements of pore distribution and mesoporosity suggest the presence of a hierarchical structure in the monolith [205]. This feature is observed mostly in the pore distribution graph (Figure 6-1), where the minor peak accounts for the pore structure at the nanoscale range [206]. Other surface measurements, such as mercury porosimetry and helium pycnometry, also supported the presence of large porosity networks, (see Supporting Information).
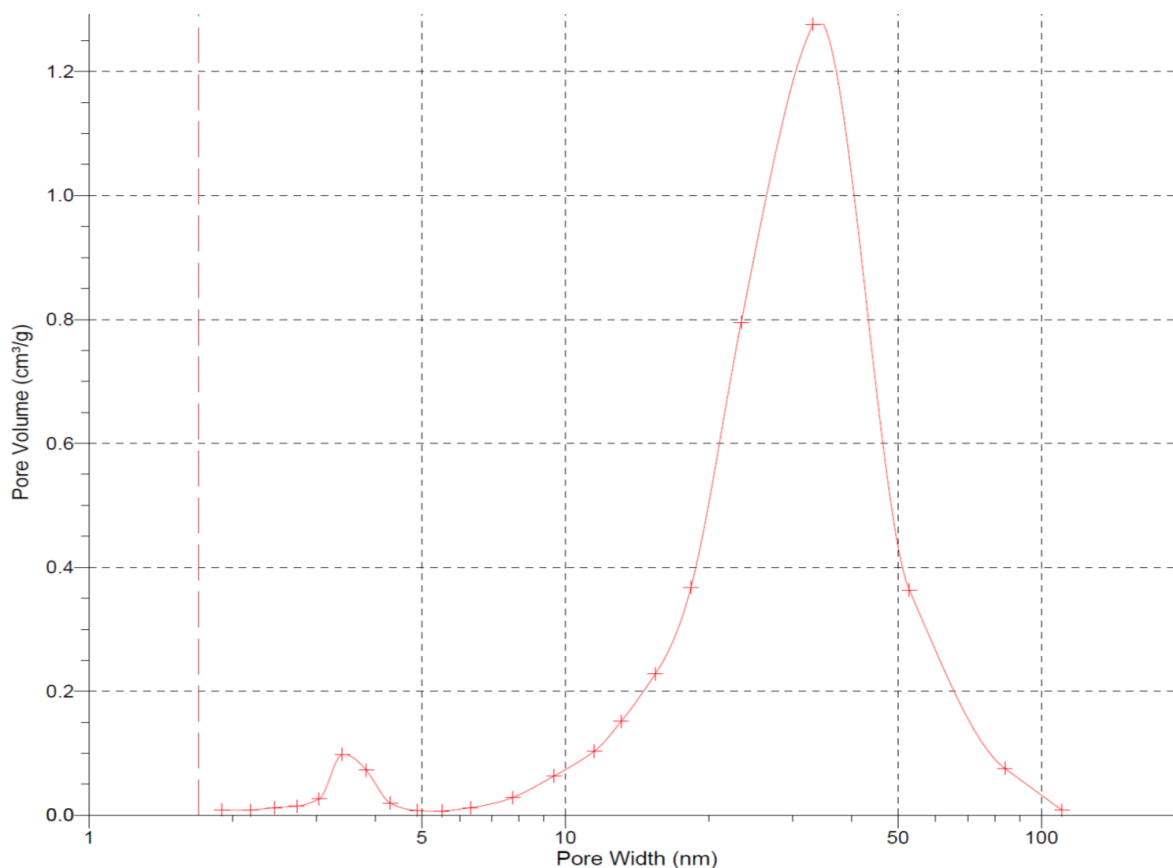
Figure 6-1. Pore volume distribution.

Bimodal porous distribution of the monolith indicates at least the presence of two porous channel distributions, as seen in above figure. But more importantly, the peak at around 3~4 nm infers the possibility of porous structures at the molecular level, which allow the interaction of gas molecules with active sites [207]. Additionally, XRD spectroscopy gives insight into the mesoporous ceramic structure, which is probably related to the ligands during encapsulation [208]. Putting all together, the encapsulation of the active centers with organic ligands might produce the narrowest porous structure, as initially designed in chapter 2 and synthesized in chapter 3. In this process, the organic templates CTAB and P123 were meant to form mesoporous structures in the range of 2 to 15 nm [209]. However, in figure 6-1, pores are

around ø 30 nm, which indicates that agglomeration due to excess of organic templates was dominant during the shaping step.

6.1.3 XRD

Structural morphology of the fresh catalyst was investigated with a X-Ray diffraction equipment D5000 of Bruker GmbH. The common metal oxide phases are highlighted in figure 6-2. Due to its outstanding conversion results, the last catalyst of table 6-1 (Cu/Ce-Ti) was selected for this diffraction analysis.
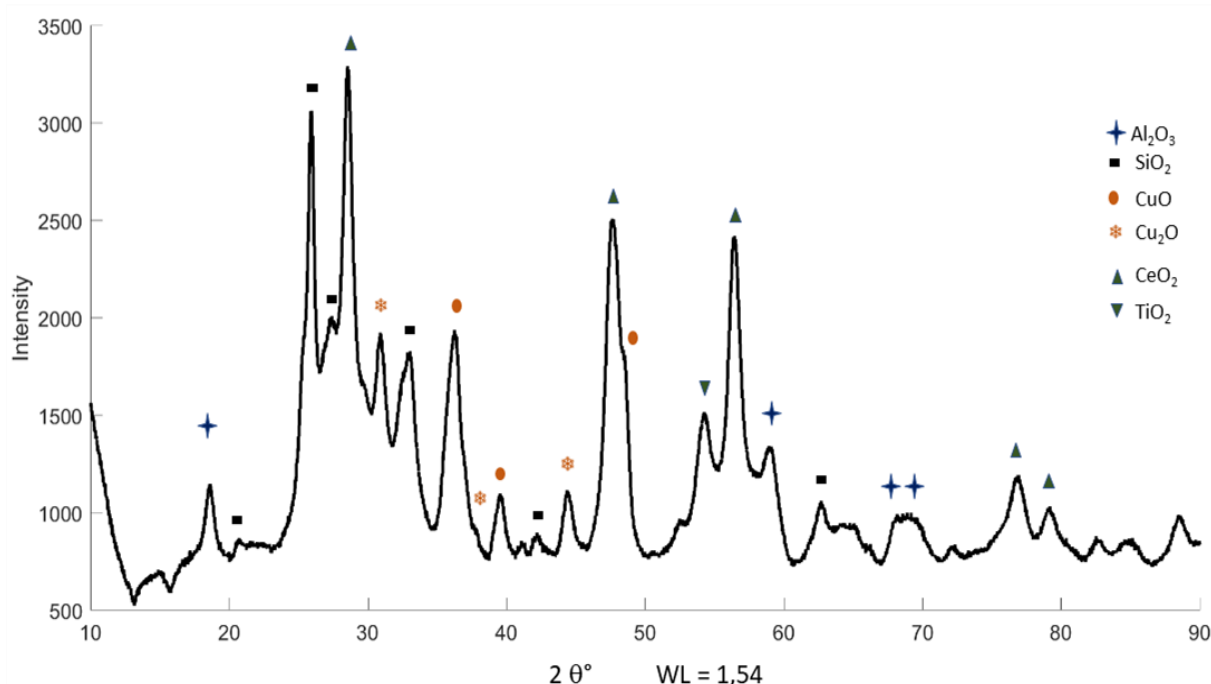
Figure 6-2. XRD patterns of SCR catalyst .
Powder sample of final catalytic filter based on Cu/Ce-Ti after calcination at 700 °C. Main transition metal oxides found in the catalytic filter.

As expected, most of the crystal structure is concentrated on SiO_2, Al_2O_3 and CeO_2, because these oxides represent roughly 90% of the monolith. In fact, these elements are mainly used in the filter support. Surprisingly, the last element CeO_2 appears to be the most abundant crystal in the catalyst, although its mass content is below 10%. This fact could be explained by the reactivity of ceria with oxygen, because the organic template gets oxidized as the temperature increases.Consequently during the thermal treatment, ceria varies the oxidation states of +3 and +4, which makes their crystal growth flexible in comparison to silica and alumina [210]. Moreover, CeO_2 has a large lattice size ($3.82 Å$) in comparison to disilicate Si_2O_7

structures (~1,6$\mathring{A}$) [211], which usually form around lantants. Therefore minor impurities of other oxides do not substantially dislocate the crystal formation [212].

Regarding the copper species, whose defects play the main role in the SCR reaction, at least two defined species were identified, CuO and Cu_2O. This changed the perception of the synthesis, because only isolated copper species were expected in the monolith. Although crystallized copper oxides are not ideal materials for the SCR process, they have shown effective results [213], [214]. Formation of Cu_2O oxides also illustrates some of the advantages of the promoters in the catalytic filter [215], [211], [208], [209], [198]. Copper oxides locally form bimetallic oxides in presence of promoters such as CeO_2, which reduces the growth of CuO clusters [198], [215], [216]. Hence, CeO_2 avoids the agglomeration of CuO particles. As seen clearly at angles of 30°, 37° and 43° (see figure 6-2), metastable Cu_2O species were stabilized. These interesting observations confirm the necessity of promoters in catalyst synthesis, which react synergically with the source of the active centers [184].

On the one hand, silicate compounds show low crystallinity, although they make up around 70% of the catalytic filter. On the other hand, the left side of figure 6-2 indicates a noticeable structure that scatters at small angles [217]. Taking into account these two observations, it may be concluded that heterogeneous aluminosilicate structures are present in the catalytic filter [217]. However, the heterogeneity of the monolith hinders a proper matching of any registered zeolite structure.

To sum up, the monolith is based on a semi-amorphous silicate structure, which is bounded through the formation of alumina and silicate phases. Nevertheless, NO_x absorbers, such as CeO_2, tend to form crystal structures in the catalyst, due to their oxidation flexibility during the calcination process.

6.2   Kinetics Study

In chapter 5, the behavior of the catalytic filters was explored under operational conditions. Nevertheless, to go deeper into the mechanism of the catalyst, the absorption and reaction of NH_3 and NO were studied individually by TPD (Temperature Programmed Desorption). In the following, three concrete experiments are analyzed in order to disclose relevant kinetic aspects of the catalyst Cu/Ce-Ti. In this way, critical temperatures for absorption and desorption are estimated.

6.2.1 NO Decomposition

Materials, such as CeO_2 and TiO_2, enhance the formation of NO_2, which in turn improves the SCR process. In fact, these oxides promote NO oxidation to NO_2, allowing Fast-SCR processes [218]. This suggests that NO requires an individual analysis to characterize the effect of the support material in the SCR performance of the catalytic filter. Hence, a simplified test was planned as follows:

A stream of Nitrogen gas with 1000 ppm of diluted NO was passed through the catalytic monolith. Temperature was regulated slowly from 110°C to 250°C, as shown in figure 6-3. To follow the N_2 evolution, NO and NO_2 were constantly measured at the input and the output, see R 6.1.

$$4\ NO \longleftrightarrow 2\ NO_2 + N_2 \qquad\qquad T{<}170°C \qquad\qquad \textbf{\textit{R 6.1}}$$

NO_x conversion and NO_2 formation are calculated, as shown in Eq. 6-1

$$NO_x\ Conversion = \left(1 - \frac{NO_{x(out)}}{NO_{x(in)}}\right) \qquad\qquad \textbf{\textit{Eq. 6-1}}$$

At first glance, nitrogen oxides are stored and partially reduced at low temperates under passive conditions. However, when temperature surpasses 200°C, the absorption effect vanishes, because some of the trapped NO is released. Moreover, formation of NO_2 is almost neglectable, as seen on the bottom part. This indicates possible decomposition of NO to N_2. Unfortunately, selectivity toward N_2 was not measured due to technical issues. Therefore, N_2 selectivity is not further considered.

NO_x measurement indicates that around 50% NO is consumed at the surface, which consequently suggests the formation of intermediate nitrate compounds [219]. Nitrate species remain stable under 190°C, afterwards they are released as NO, NO_2 , N_2O_5, N_2 and O_2, which indicates partial decomposition of NO at low temperature [220]. This plays a key role at low temperatures, because trapped NO is hardly released again as a stable species [221]. Instead, NO species move towards oxygen vacancies or defects on the support [47].

According to studies on LNT catalysts (Lean NOx Storage Trap) [222], NO is mostly absorbed on oxygen vacancies ($[MO_2]^+$), leading to the formation of nitrates, see R 6.2. In the monolithic catalyst Cu/Ce-Ti, nitrates such as $Ce(NO_3)$, $Al(NO_3)$ and $Cu(NO_3)$ can be expected. Particularly ceria is widely recognized across the literature [223], [186], because of its redox

properties Ce^{+3}/Ce^{+4}. This redox reaction might explain the high adsorption and conversion rate observed in figure 6-3. Therefore, it can be concluded that mostly cerium ions are involved during the NO adsorption experiments.

$$[MO_2]^+ + NO \rightarrow MNO_3 \qquad\qquad T<200°C \qquad\qquad \textbf{\textit{R 6.2}}$$
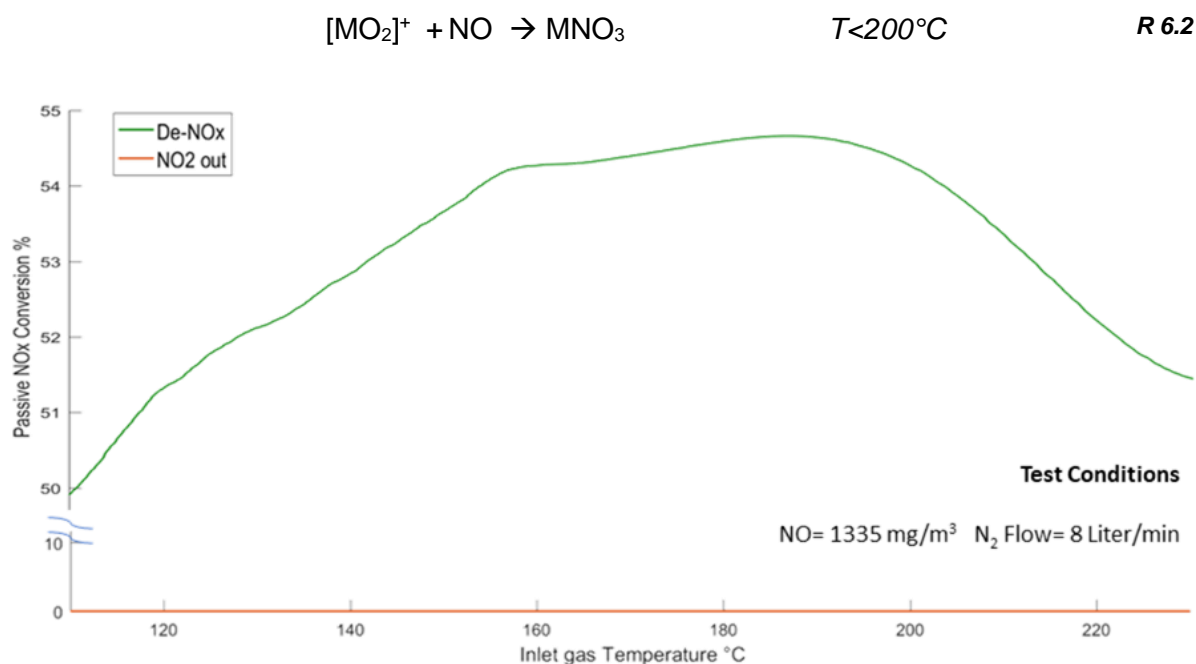
Figure 6-3. Passive NOx conversion in relation to temperature.

As seen on the right side of the previous figure, the NO_x-Trap has a limit, which is basically set up for the absorption properties of the catalyst. NO desorption on ceria supports begins at around 190°C [222]. Despite of the small temperature range, this storage effect is highly beneficial, because stored nitrate reacts also at a low temperature, when a reducing agent (NH_3) is absorbed in its neighborhood. This surface mechanism is also named Langmuir-Hinshelwood mechanism [224].

6.2.2   Ammonia Oxidation

In working conditions, NH_3 slips are common due to the unstable NO feed. Thus, adsorption and subsequently oxidation of overdosed ammonia are desired characteristics of a catalyst. At low temperature, ammonia is absorbed at the Bronsted sites of the monolith and oxidized to NO_x as depicted in reactions R 6.3 and R 6.4 [93]. Depending on the availability of active centers downstream of the catalyst, NO and NO_2 are reduced by the remaining ammonia. However, part of the overdosed ammonia might generate additional NO_x emissions, when the nitrogen oxides don't react, which is detrimental to the after-treatment system. To analyze this, the ammonia oxidation was evaluated in dependency of temperature under air conditions, see figure 6-4.

$$4NH_3 + 5\ O_2 \leftrightarrow 4\ NO + 6\ H_2O \qquad\qquad T<170°C \qquad\qquad \textbf{\textit{R 6.3}}$$

$$4NH_3 + 7\ O_2 \leftrightarrow 4\ NO_2 + 6\ H_2O \qquad\qquad T<170°C \qquad\qquad \textbf{\textit{R 6.4}}$$

As shown below, ammonia is totally converted, indicating the strong acidity of the catalyst [225]. Around 10% of NH_3 is converted to NO_x, which might be undesired. Nevertheless, these conditions are far away of the standard exhaust emissions. Therefore, it can be stated that the excess of ammonia in the aftertreatment system might be controlled with an efficiency of 90%.
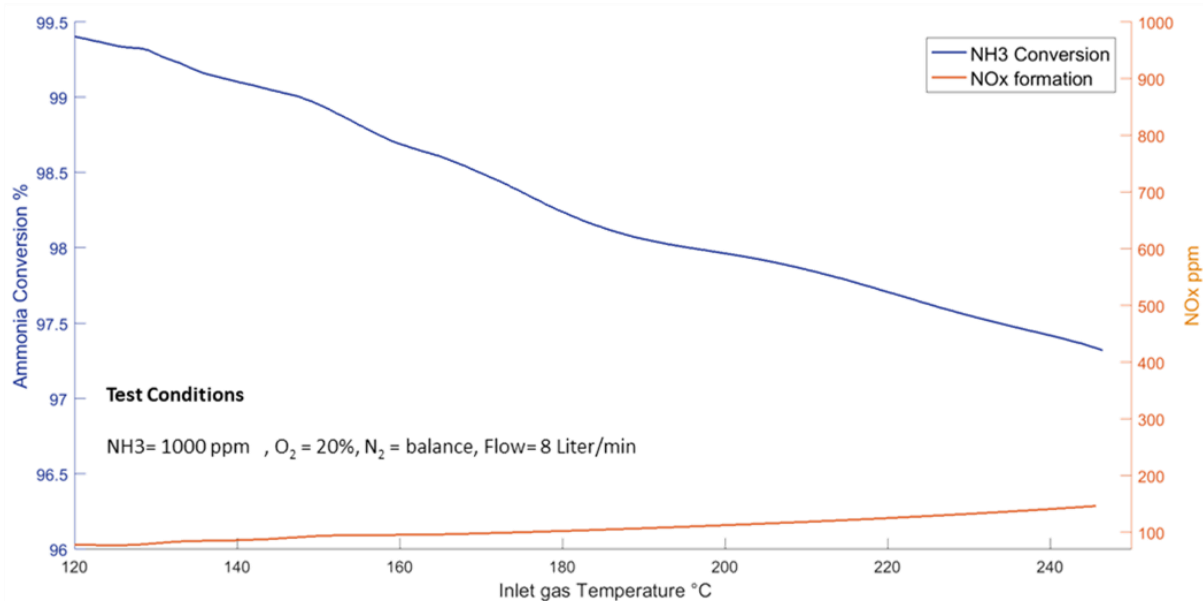
Figure 6-4. Ammonia oxidation.

Looking at the synthesis, isolated copper ions are expected to generate acid sites, where ammonia preferably binds [93]. For simplification, these active centers are illustrated as charged metal oxides [M-O], see R 6.5 and R 6.6. Moreover, the previous figure shows that almost all the ammonia is converted. Therefore, the monolith contains enough active sites with a selectivity of approximately 90% towards N_2. As seen on the red line, only around 100 ppm NO_x can escape from the catalytic center. This indicates that once ammonia is absorbed at the active center it evolves to NO intermediate under oxygen presence, as shown in reaction R 6.5. Apart from water production in reaction R 6.5, the active center $M^+O-[NH4]^+$ turns into a nitrate intermediate $[M^{2+}-NO]^-$, which facilitates the uptake of another ammonia molecule.

Afterwards, a second ammonia molecule reduces the nitro compound to N_2, as proposed in reaction R 6.6. In this step, the activated center $[M-NO_2]^-$ returns to its initial step, M-OH, and subsequently ammonia is dehydrolyzed and nitrogen is formed, see right side of R 6.6.

$$M^+O\text{-}[NH4]^+ + O_2 \leftrightarrow [M^{2+}\text{-}NO_2]^- + 2H_2O \qquad\qquad T<120°C \qquad\qquad \textbf{\textit{R 6.5}}$$

$$[M\text{-}NO_2]^- + NH_3 \leftrightarrow M\text{-}OH + N_2 + H_2O \qquad\qquad T<120°C \qquad\qquad \textbf{\textit{R 6.6}}$$
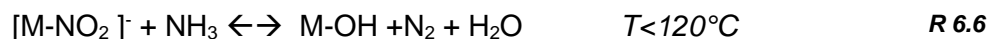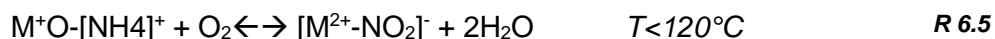
As shown in section 5.2, excess of ammonia was not critical under SCR conditions. This confirms that the catalyst efficiently converts NH_3 to N_2, because NO species evolve at the same active center, which overcome the inefficiencies as a result of random absorption. Therefore, ammonia oxidation at low temperature is possible up to 95%, because intermediate species are converted immediately in the same active center. In consequence, excess of NH_3 does not increase the NO_x emissions notably.

Taking into consideration both the results of this section and those of the previous sections, it is found that the NO_x conversion rate in the catalytic filter is determined by the NO absorber rather than the accessibility of the active sites (Cu- ions). Therefore, the different proximities of NO_x traps and Bronsted sites are crucial for the conversion rate in these catalytic filters. This fact also supports the finding in chapter 5.1.2, where the activity of the catalyst was strongly promoted by CeO_2 and TiO_2 supports.

6.2.3   NOx Conversion by Propane

Today, experiments with diesel aftertreatment shows that NOx reduction by soot is a relevant topic of the catalyst. Previous studies have concluded that volatilization of soot initiates the SCR cycle in a similar way as ammonia does, which diminishes the urea consumption [226]. Additionally, at low temperatures soot gets oxidized by NO, thus leading to intermediate species as in the 3-way catalyst [180], as shown in the reactions below.

$$C_{x+1}H_y + O_2 \rightarrow C_xH_yO + CO \qquad\qquad T<190°C \qquad\qquad \textbf{\textit{R 6.7}}$$

$$C_xH_yO + 2NO \rightarrow N_2 + H_2O + CO_2 + C_{x-1}H_{y-2} \qquad\qquad T<230°C \qquad\qquad \textbf{\textit{R 6.8}}$$

$$2CO + 2NO \rightarrow N_2 + 2CO_2 \qquad\qquad T<550°C \qquad\qquad \textbf{\textit{R 6.9}}$$
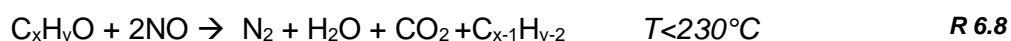
In our experiments, NO reduction by soot was also identified, see section 5.2. However, meassuremts of chemical composition and soot concentration was difficult to implement in the motor test bench. Instead, a controlled experiment was set up in order to measure the

contribution of soot in the NOx conversion. In figure 6-5, the reduction of NO by propane was recorded at low temperature range. For practical reasons, propane gas was used to simulate the volatile hydrocarbons generated during soot volatilization. Additionally, 10% oxygen was fed into the flow to emulate lean conditions, which are typical in diesel motors.

As seen in the figure below, at more than 240°C propane becomes active towards NO. In the range from 190°C to 230°C, there is a plateau behavior indicating absorption and possibly NO decomposition as denoted by reaction R 6.1. At around 180°C, there is an absorption peak, which correlates with the observation of NO absorption, see figure 6-3. Therefore, it can be assumed that at temperatures between 160°C and 230°C absorbed NO starts to react towards NO_2 on the surface.
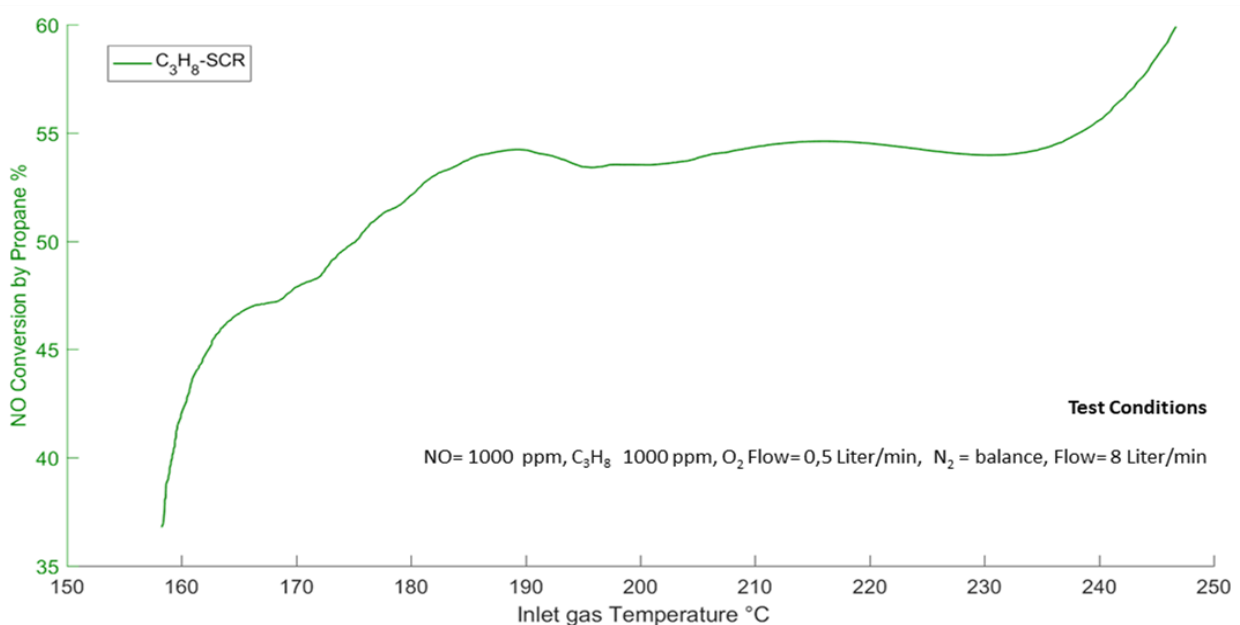
Figure 6-5. NOx reduction by C_3H_8 over Cu/Ce-Ti catalyst from 160°C to 250°C.

In conclusion soot oxidation on the catalytic filter is advantageous when the flue gas is hotter than 240°C. Despite the positive effect on the NO reduction, soot continuously accumulates, thus clogging the catalyst. To release absorption sites and to consequently reduce pressure drop, temperatures of over 550°C are required to oxidize the soot completely. Hence, at temperatures of under 250°C, the accumulation of soot will saturate the porosity of the catalyst, which leads to plugging of the monolithic catalyst.

6.3   Active Sites

Measurements of NOx, NH_3 and C_3H_8 conversion support the existence of active structures, which change in presence of NO and NH_3 above 130°C. However, an exact structure or position of active sites is difficult to infer based on the previous EDX and XRD measurements. In fact, active centers transform themselves at working conditions, thus analysis at room temperature does not show the real picture of the system. In consequence, the elucidation of an active center in this sintered catalyst goes beyond the analysis of a single cluster at mild conditions.

Actually, active monoliths require the addition of binders and promoters, in order to improve mass transfer, adsorption of reactants and mechanical stability. Despite of the complex porosity of a catalytic filter, active sites in the bulk structure can be investigated through magnetic techniques, such as EPR (Electron Paramagnetic Resonance) and NMR (Nuclear Magnetic Resonance) spectroscopy. Thanks to these techniques, it is possible to go inside of the catalytic monolith to unveil some of the active sites.

6.3.1   EPR Analysis

Because of their activity towards ammonia at low temperature [227], [228], [68], isolated Cu^{+2} ions are referenced in several publications as active centers for the SCR reaction. Furthermore, these copper ions have paramagnetical properties, which make them detectable by EPR technique. Hence, this spectroscopy technique has been widely used for studies of Cu^{2+} ions in SCR catalysts. Not only ion existence but also coordination environments can be revealed through this method. Thus, EPR measurements were also implemented here on the sintered catalyst in order to find the state of some copper species in the monolith [68].

To make a grounded analysis and to obtain accurate *g* and *A* values, an approximate EPR spectrum was simulated. This was done using the Easyspin tool, which runs under Matlab environment [229]. By omitting hyperfines it was possible to estimate a theoretical spectrum, see blue dotted line (see figure 6-6). By this approach, values of $g_{1\parallel}$~2.44 and $g_{1\perp}$~1.9 were estimated from the simulated signal.

The model includes an anisotropic component, which is actually even stronger than the isotropic one, see minimum value $g_{2\perp}$~2.04. Eventually, the value $g_{2\perp}$ gives insight into the interaction of hydrate species in coordination with the copper ions. In fact, under normal conditions these copper ions are slightly stable on the support, thus they reduce their charge stress by bounding with hydronium species $[OH]^-$. This feature accounts for the hydrated species in the catalyst, which frequently come from ambient air [230].

Moreover, this anisotropical signal $g_{2\perp}$ points out another important aspect of the activated catalyst at 230°C. In the heated sample, the signal $g_{1\perp}$ shows more intensity than $g_{2\perp}$, indicating homolytical cleavage of $[Cu(OH)_2]^{+2}$ moieties, which leads to isolated Cu^+ species [231]. This cleavage partly generates Cu^+ sites, which are highly active but EPR silent, subsequently the $g_{2\perp}$ signal declines in the upper red line (see figure 6-6).

In addition to unpaired ions, the EPR spectrum might give insight into other properties of the prepared catalyst. As shown in figure 6-6, the fresh catalyst not only contains isolated copper species but also oxygen vacancies and dimers of CuO. In fact, anisotropic distribution of these copper species generates other signals and features, whose observable peaks are portrayed as "O" , "K" and feature "B" in figure 6-6.

Feature "B" represents the strong broading ($\Delta H \sim 240G$), produced by dipolar interaction of unpaired ions [232]. Typically, this signal comes from dipolar interaction between Cu^{2+} ions in CuO [233]. In fact, the CuO has been clearly identified by XRD analysis, see figure 6-2.
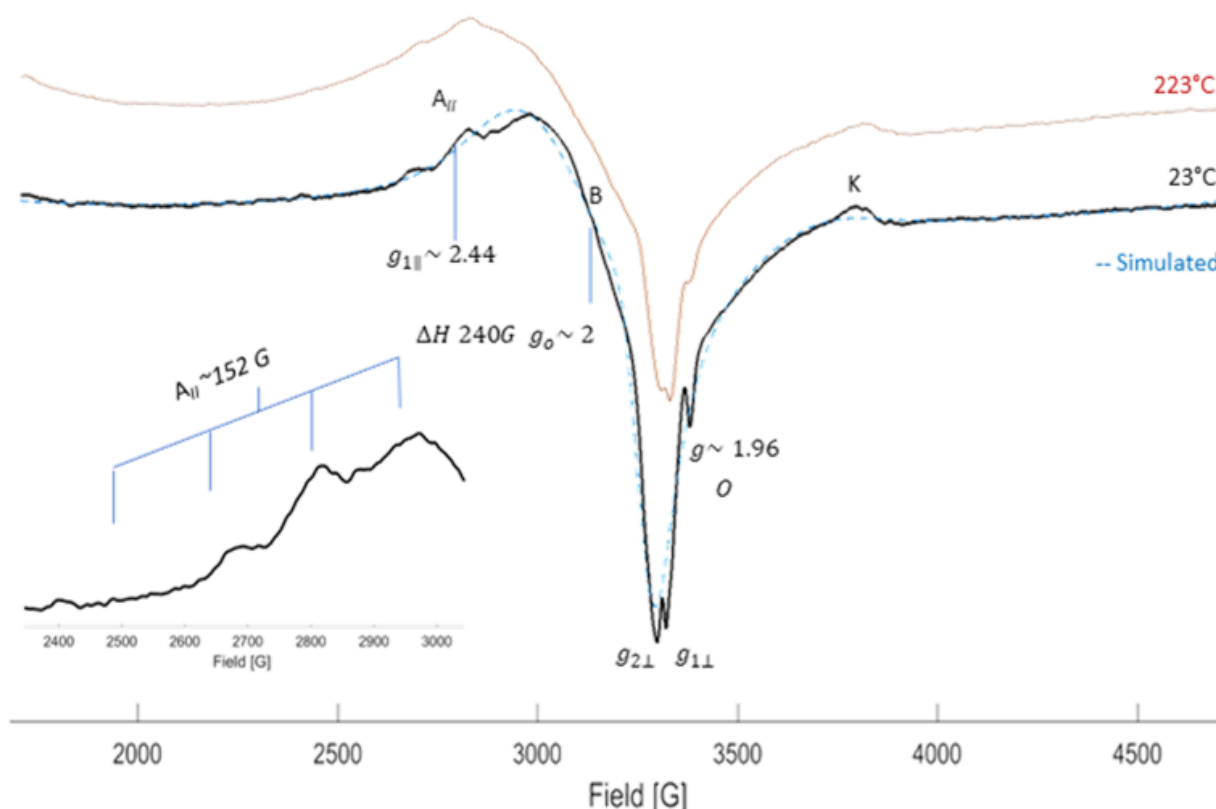
Figure 6-6. EPR spectrum from fresh catalyst.

Black line: Cu/Ce-Ti catalyst at room conditions. Red line: Cu/Ce-Ti heated up to 230°C.

Dotted blue line: Simulated spectrum.

Regarding isolated ions, the enlarged interaction of the electron with the Cu nucleous, left lower corner of figure 6-6, illustrates a weak interaction of Cu^{+2} ions in the catalyst. This hyperfine resonance, $A_\parallel \sim 152$ G, agrees numerically with well measured copper hyperfines [234]. However, in the case of the sintered catalytic filters, evidence of isolated species is barely found. Although the formation of isolated species was the main focus of this work, integration of catalyst and support favored the formation of mixed clusters instead.

In accordance to previous studies, the "O" signal illustrates the formation of oxygen vacancies on metal oxides, for instance Ce^{3+} and Ti^{3+} [235]. Particularly the latter one is responsible for the signal at $g_\parallel \sim 1.96$ G. Theses oxygen vacancies, also named holes, entrap electrons which are stabilized by cationic impurities. As the heterogeneity of the material increases, these defects become representative [236], which strengthens the signal "O" shown in figure 6.6.

At working temperature, hyperfine splitting almost vanishes, but $g_{1\perp}$, "O" and "K" are still active, suggesting the formation of CuO species [237], see red line figure 6-6. In fact, signals "O" and "K" are generated by oxygen vacancies in oxides, i.e., Ti or Ce oxides [232], therefore oxidation of supported Cu ions is highly presumable. During sintering of the catalytic filter, some copper ions migrate to these oxygen vacancies [201]. In this process, temperature and oxidative atmosphere facilitate the oxidation of these ions on the support lattices. This process results in the formation of polymeric copper oxides on the support, which also remain stable at 230°C [232]. As seen on the red line of figure 6-6, signals "K" and "O" are still active at over 200°C, which confirms the relevance of promoting agents in the catalyst.

i.   *Reduced sample*

Coming back to the reaction conditions, two additional samples were prepared in order to see how the electronic structure of the catalyst changes under reduced and oxidized conditions. For the reduced sample, a stream flow of argon with 1000 ppm of ammonia was set. The reduction was performed at around 300°C for 6 hours, which simulates the injection of ammonia at working conditions, see reaction R 6.10. To keep the sample reduced, it was cooled down under ammonia flow and stored at dry conditions.

In the next step, an EPR spectrum was recorded at room temperature. Finally, to see the change on the catalyst under oxidative atmosphere, the sample is heated under ambient air. By doing so, the sample should return to the conditions of a fresh catalyst.

As seen in figure 6-7, some features of the signals "A", "B", "K" and "O" changed. Firstly, the anisotropic signal $g_{\perp, a}$ vanished partially, as ammonia reduced the sample. Additionally,

shown in the lower left side of figure 6-7, distortion of the original hyperfine splitting reveals new electron-neutron interference patterns, here denoted as "D" and "G". This could indicate that bonds between copper and ammonia are being created, where previously hydroxy bonds existed. This can clearly be seen at the zoomed hyperfine, see figure 6-7. Like in similar works, coordination of ammonia with copper generates additional signals "D" and "G", due to the formation of $[Cu(NH_3)_4]^{+2}$ and $[Cu(NH_3)_5]^{+2}$ species, which may follow the reaction R 6.10 [238].

$$Cu^{2+} + 4\,NH_3 \rightarrow [Cu(NH3)_4]^{+2} \qquad\qquad T>180°C \qquad\qquad \textbf{\textit{R 6.10}}$$

During the oxidation process, most of the ammonium species react with oxygen, leading to Cu^+ formation, see reaction R 6.11. Because Cu^+ are EPR silent, the hyperfine interaction disappears as noticed on the plateau behavior of the upper red line in figure 6-7. Thus, Cu^+-O-M bonds start to be abundant under this condition, making the Cu^{2+} hyperfine smoother and the O^- signal larger, as described in reaction R 6.11 [239]. Moreover, the oxygen vacancies rise up to an intensity comparable to that of the isolated Cu^{2+} species. That means that the O signal is a product of migration of copper ions that were bounded on metal oxide clusters [240]. This suggests that the reaction of ammonia species mostly reduces copper oxide clusters, thus increasing the intensity of the O^- signal.

$$[Cu(NH3)_4]^{+2} + 3\,O_2 \rightarrow Cu^+\ 2N_2 + 6H_2O \qquad T\sim230°C \qquad\qquad \textbf{\textit{R 6.11}}$$
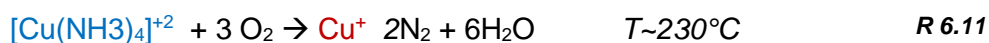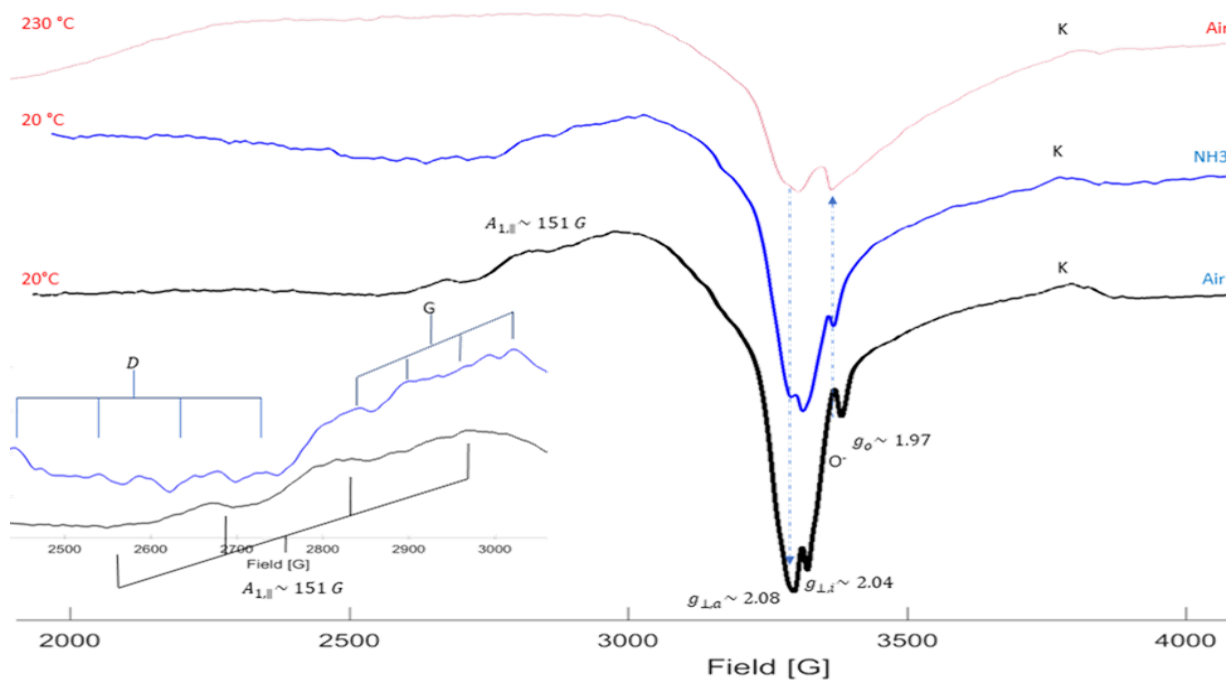
Figure 6-7. EPR spectrum during ammonia oxidation.

ii. Oxidized Sample

The third sample was treated with stream of argon and 1000 ppm of NO diluted by a mixer. Similar to that of the reduced sample, the reaction was carried out for 6 hours at 300°C. By doing so, structural changes caused by NO absorption were identified during the EPR measurement.

$$2\ Cu^- + 2\ NO \rightarrow 2\ CuO +\ N_2 \qquad\qquad T>180°C \qquad\qquad \textbf{R 6.12}$$

$$2\ [Cu_2(OH)]^+ + 2\ NO \rightarrow 4\ CuO + N_2 +\ H_2O \qquad T>180°C \qquad \textbf{R 6.13}$$
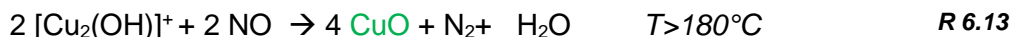
Oxidation of copper sites by nitrogen oxide shows a different picture. In general, the EPR response suffered a strong straightening, which could be connected to the oxidation of Cu^+ to CuO clusters [241]. Moreover, the "O" peak and the anisotropic signal $g_{\perp, a}$ lose intensity under oxidation. This tendency can be traced by the signal "O" in figure 6-6 and figure 6-8. In fact, this effect becomes more evident, when the sample is heated up to 230°C at ambient air, see upper brown line in figure 6-8. This indicates that some Cu_2O species, identified in figure 6-2,

were converted to CuO, see R 6.14. Consequently, the oxidized spectrum is widened due to the increase of dipolar species like CuO [242].

$$2\ Cu_2O + O_2\ \rightarrow\ 2\ CuO \qquad\qquad T>220°C \qquad\qquad \textbf{R 6.14}$$

Despite the strained spectrum, the original hyperfine $A_{1,\parallel}\sim$ can still be observed after an offset correction, though. Following the previous three reactions, it can be expected that the oxidative treatment does not affect isolated Cu^{2+} species. However, their signal intensity turned out weak because of the spreading of CuO particles.

The role of the oxygen vacancies is even more interesting to disclose here. This is represented by the signal "O" and "K" at the right side of figure 6-8. While signal "O" becomes silent through heating, the "K" signal seems to be weak but stable. In fact, the "K" signal stands for the coupling of Cu ions with other oxides in the support, which results in bimetallic oxides, see left side of R 6.15. Eventually, when the temperature ascends, most of these bimetallic clusters tend to regenerate when the catalyst gets oxidized, as depicted in reaction R 6.17. On the contrary, the "O" signal does not come back, which indicates the difference between vacancies and dimeric species during oxidation.

NO treatment forms nitrate species, which could be responsible for the remaining oxygen vacancies. In chemical terms, the lack of oxygen reduces "K" species by the NO treatment, see R 6.15 and R 6.16. Finally, during the heating with ambient air, these nitrate species react releasing dimeric sites, see reaction R 6.17, resulting in a small recovery of the "K" peak, see brown line in figure 6-8.

$$[CuO_2M] + 2\ NO\ \rightarrow\ Cu(ON)_2 + MO_2 \qquad\qquad T\sim300°C,\ Ar \qquad \textbf{R 6.15}$$

$$M^{+4}O_2 +\ m\ NO + \rightarrow\ M^{+3}(NO_3)^{-3} + (m/2\text{-}1)N_2 \qquad T\sim300°C,\ Ar \qquad \textbf{R 6.16}$$

$$2\ MNO_3 + O_2 \rightarrow\ 2\ MO_2 + N_2 + O_2 \qquad\qquad T\sim230°C,\ Air \qquad \textbf{R 6.17}$$
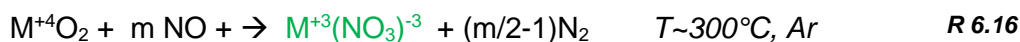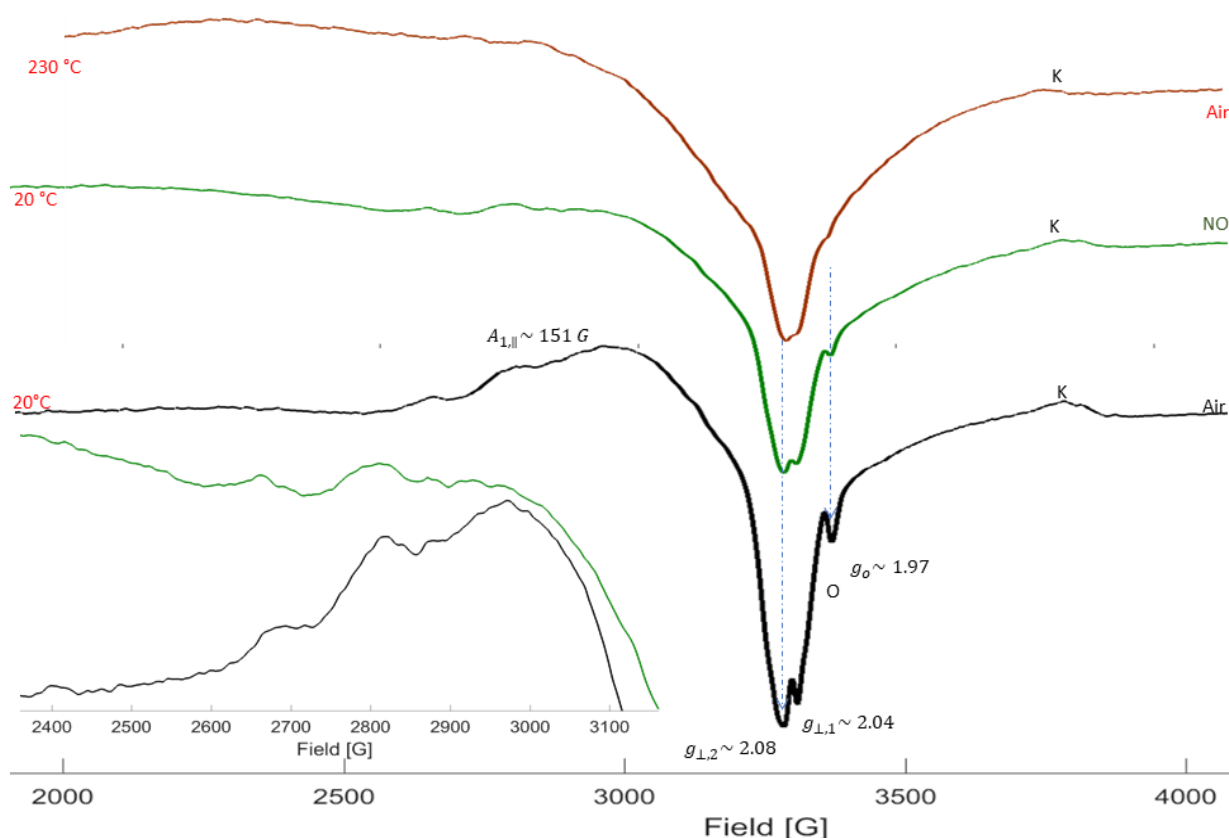
Figure 6-8. EPR spectrum from oxidation of catalyst with NO/O₂ at 230 °C.

Black line: Reference sample. Green Line: Treated sample with 1000ppm of NO. Brown line: Spectrum after NO treatment and in-situ oxidation with air.

To summarize the EPR observations, at least three active species were found, i.e., copper ions, oxygen vacancies and dimeric species. In the first instance, the expected isolated ions ($A_{1,\parallel}$) are present but only as a minority. Nevertheless, their existence remarkably contributes to the activation of ammonia at low temperatures, as seen in figure 6-7. Secondly, oxygen vacancies, "O¨" sites of the support material (i.e. Ce^{3+}, Ti^{+3}), were present in most of the EPR measurements [201], thus indicating their relevance for NOx adsorption. Finally, dimeric species seem to be selective towards NO oxidation, however their low intensity limits any further claim.

6.3.2   NMR Analysis

Around 80% of the catalytic filter consist of supporting material. More precisely, the support is based on silicates and aluminated compounds. Although silicates are not highly catalytical, these structural compounds contribute to flow mass distribution and absorption of species

during catalysis. Actually, in technical catalysis, it could be considered equally important as the function of the active centers. Therefore, an analysis of the silicate and alumina molecules by NMR would reveal important features of the monolith structure. In addition, interactions between support and active centers can be inferred by analysis of silicate environment.

i. *Silicates*

The solid state ^{29}Si Magic Angle Spinning (MAS) NMR spectra was recorded on an Agilent DD2 500WB spectrometer at resonance frequencies of 99.30 MHz. The chemical shifts of ^{29}Si are referenced to tetramethyl silane (TMS) at 0 ppm. Although XRD indicates the formation of SiO_2 and Al_2O_3 compounds, these compounds do not supply the required absorption sites for ammonia and nitrogen oxides for the reaction. Therefore additional silicate species need to be identified in order to clarify the absorption properties of the catalytic filter [76].

In conformity with the XRD measurement, the filter structure is dominated by tetragonal silica compounds. In figure 6-9, the colorful signals account for tetragonal silicate compounds Q_4, where the aluminated type Q_4 (1Al) is the most popular among them. Conversely, pure silica "Quartz" was also identified at the left side of figure 6-9, Q_4 (0Al) but to a lesser extent [205].
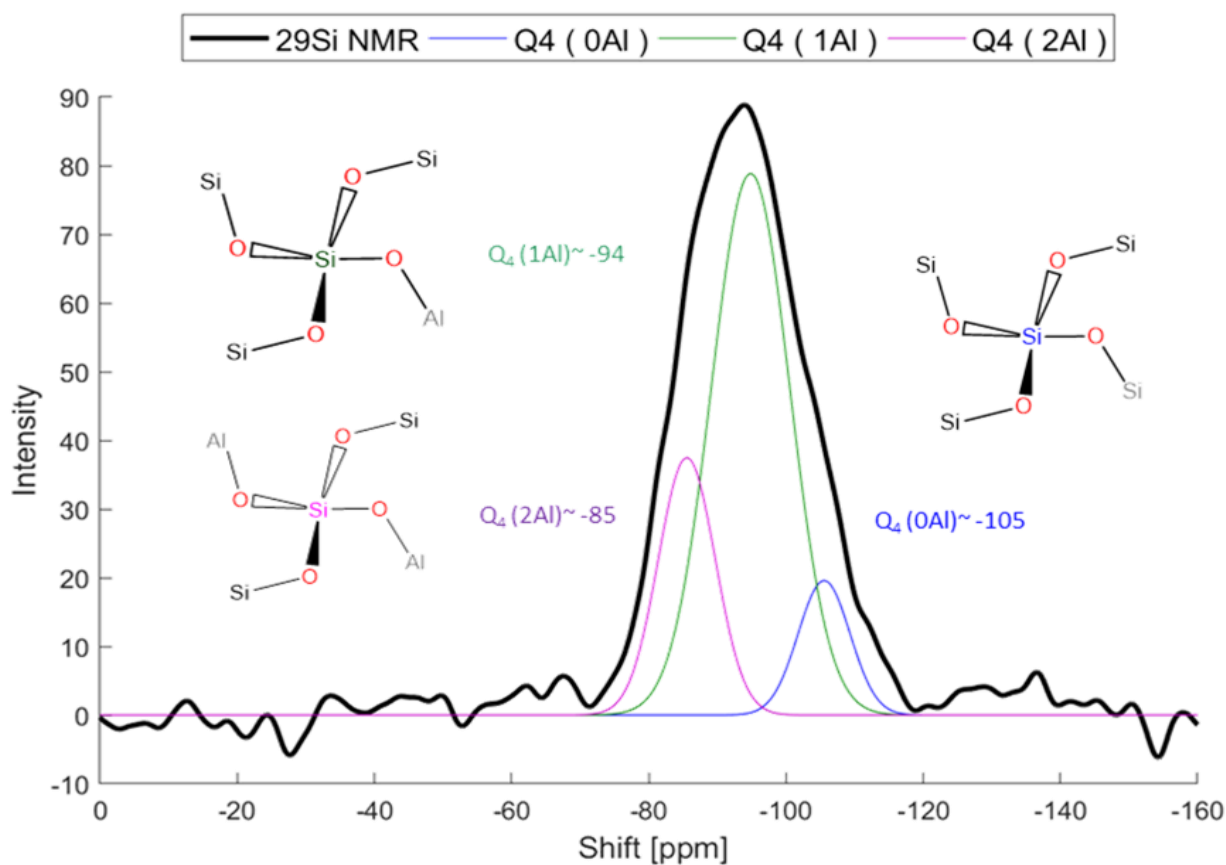
Figure 6-9. ^{29}Si and ^{27}Al NMR of the catalytical filter.

While Q4(0Al) stands for pure and inert SiO_2 crystals, Q4(1Al) and Q4(2Al) indicate the existence of one and two alumina bonds respectively. Actually, this characteristic makes the later ones, aluminosilicates, more interesting for the catalytic process, because of the chemical properties of these bonds [243].

ii.   Aluminates

^{27}Al NMR measurements were conducted on an Agilent DD2 500 W B spectrometer at a magnetic field of 11.74 T equipped with a 3.2 mm triple resonance MAS probe at [27]Al resonance frequency of 130.24 MHz. Using this configuration, the aluminum NMR spectrum shows a more mixed pattern. To shed further light into this, the signal was deconvoluted into 4 aluminum species, as figure 6-10 illustrates. Individual signals cover the possibly coordinated aluminates, showing the functionality of aluminates in these monolithic bodies.

On the right side of figure 6-10, octahedral species might be assigned to the cluster of Al_2O_3 (q_6) at the range of -6 [ppm]. On the monolith most of them work as binders in the filter structure. Particularly so (κ-Al_2O_3), here portrayed as q_{5+1}, facilitates the transition of alumina phases towards $\gamma-Al_2O_3$ in the ceramic structures [244]. These species are also named Al_{v+l} due to their stressed oxygen bond, see left lower side of figure below [245]. Even though all these octahedral species contribute to the mechanical stability of the support, their catalytical activity is limited [246], [164].

The five coordinated aluminates are chemically more interesting because of their ability to bond with copper species [247]. They are also named hexagonal and seem to be predominant, see blue component $Al(OAl)_5$, q_5. Quantification of individual components indicates that more than 60% of the aluminum remain in the catalyst as gamma phase $\gamma-Al_2O_3$, which comprises q_5 species [248]. Despite the fact that these phases are not mechanically stable, their absorption and reactivity properties make these aluminum compounds fundamental for coupling different silicate and alumina phases in the monolith [249].
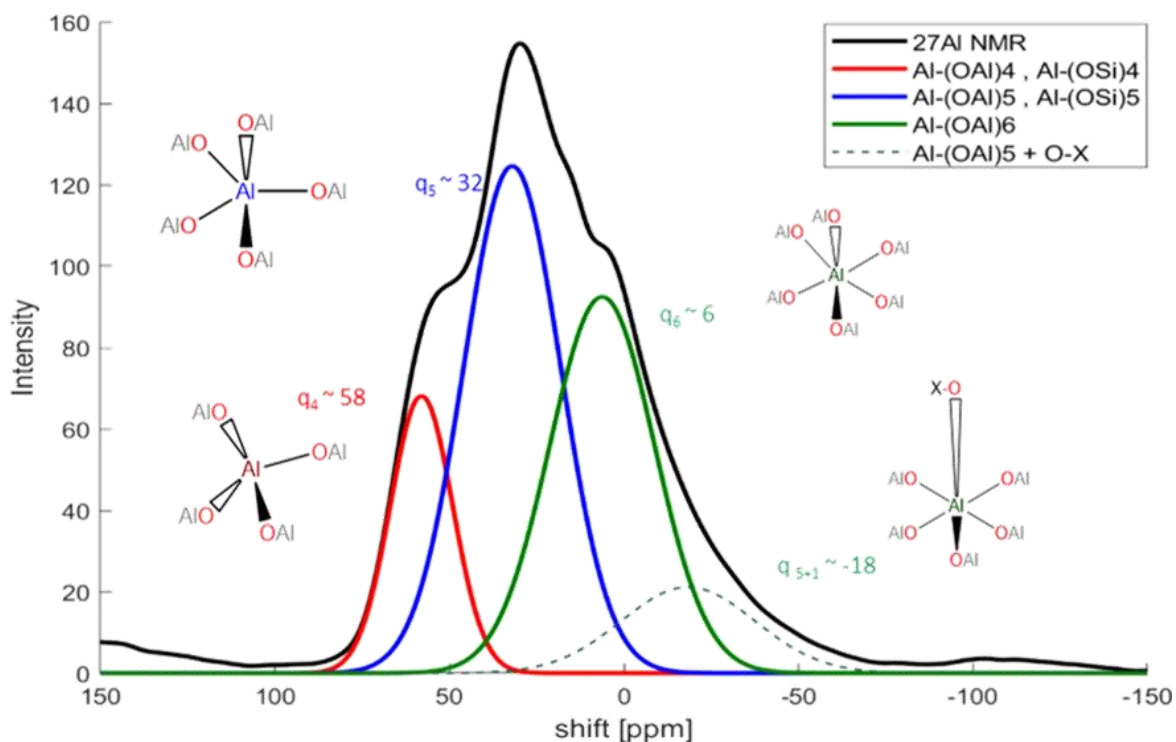
Figure 6-10. ^{27}Al NMR spectrum from catalyst support on Silicium-Aluminum matrix.

Finally, on the left side of figure 6-10 a tetragonal alumina is illustrated. These species (q4, see red line) have already been widely identified as the active aluminum atom in zeolites [250], [251], [252]. Moreover, these aluminum bonds indirectly account for ammonia absorption sites on the silica framework. Therefore, based on these observations, it can be assumed that the q4 species contribute to the formation of acidic sites in the silica structure.

To close, ^{29}SI NMR measurement shows the majority formation of Q_4 (1Al) silicate compounds, as expected from the material synthesis, see section 3.2.1. Regarding ^{27}Al NMR, few quantities of tetragonal aluminas q_4 were observed. From these observations, formation of aluminosilicate species might be proposed because of the presence of Q_4(1Al) and q_4. However, a finer estimation of the structure is required to corroborate the crucial role of these material compounds in the catalytic filter. Moreover, q_6 and q_5 alumina phases show that alumina phases β, γ and κ were formed during the calcination of the monolith [253] [65].

7   Conclusions and Outlook

Fulfilling of upcoming emission standards involves the development of new materials, which combine features such as sustainability, efficiency and marketability. For the case of air pollution, this means that economical aftertreatment systems with low operation cost and recyclable materials are required. To address these demands, an engineering approach was developed through this project by fabrication of a compact and efficient catalytic filter, as illustrated below.

Fabrication Process				
Stages	Educts	→	Process	→ Product
Synthesis	Catalyst, Solvent, Autoclave.		Solvothermal Treatment	Metalorganic complex
Shaping	Complex, Silicas, Filter Support.		Mixing, Molding	Monolith
Thermal Treatment	Monolith, Air, NH₃		Detemplating, Sintering	Sintered Catalytic Filter
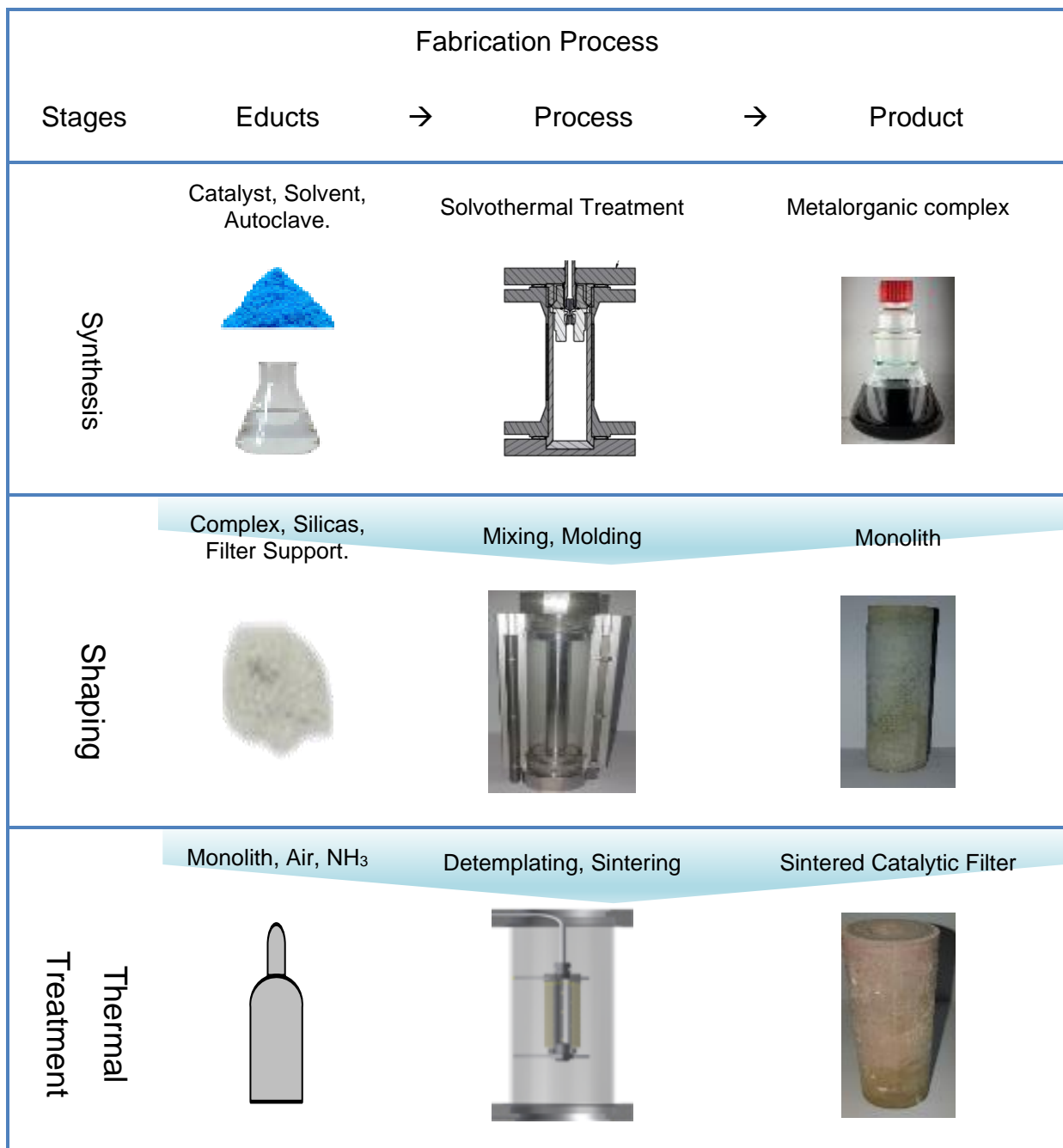
Figure 7-1. Overview fabrication process of a catalytic filter.

The fabrication process can be summarized in three steps – synthesis, shaping, and thermal treatment – as represented in the stages in the left column of figure 7-1. Incoming materials, main process and product are shown for each stage, illustrating the gradual transformation of the input materials into a catalyst. By following the arrows of the process from left to right, it is possible to get a complete overview of the fabrication which finally produces a sintered catalytic filter, as shown in the lower right-hand corner.

In the last chapter of this work, relevant learning aspects from this process will be elucidated first. In this section, results from the analysis are correlated with the fabrication process, involving aspects from chapter 3 and 6. In that way, the crucial element of the synthesis will be highlighted. Next, in section 7.2, technical aspects and performance results will be analyzed in more detail. By doing so, concrete aspects, seen in chapter 5, and features of the catalytic filter, analyzed in chapter 6, are correlated. Last, an outlook for future works will be given.

7.1   Process Development Overview

In contrast to impregnation, preparation of catalysts by encapsulation requires the use of organometallic chemistry for protecting the active center by organic ligands. As described in chapter 3, the preparation of the active center involved the use of azide complexes, which contain N-N bonds. These bonds coordinated strongly with copper ions, thus the active centers were shaped with azido bonds. These complexes were crucial during the calcination of the catalyst because after the thermal treatment, copper complexes form unstable copper oxides. Those oxides preferably react with ammonia under reduced conditions, as seen in chapter 6. Moreover, in the EPR test with the ammonia, isolated copper $[Cu(NH_3)_4]^{+2}$ and $[Cu(NH_3)_5]^{+2}$ species were identified in the catalyst. In consequence, the encapsulation method can partially produce isolated active centers, as initially planned. Nevertheless, interaction between the ligands and other compounds in the monolith led to the formation of other more active components.

Encapsulation and formation of a porous structure was planned by using organic compounds. This is a common practice in porous structure synthesis. Similarly, this concept was successfully applied by addition of porous agents, such as CTAB and P123. In that way, porosity of the monolith was proportional to the template content in the mixtures. These surfactants facilitate the fabrication of a homogenous mixture before mechanical shaping. However, excess of templating agents hinders the mechanical stability of the calcinated monolith because removal of the template interferes with continuous growth of single crystals.

Therefore, monoliths with porosities of over 70% were mechanically unstable and subsequently cracked, due to their fragility.

To cope with this stability issue, release of the template was mechanically controlled during the shaping step. In fact, expansion during calcination was constrained due to geometrical limitations at the casting mold. In addition, porosity was also systematically controlled by the pressure in the shaping process, which enhanced the mechanical stability of the monolith. Therefore, it was found that porosity of the monolith was not only defined by the amount of the template but also by the mold geometry and the shaping pressure.

In addition to measurement during the shaping process, thermal treatment was driven slowly for optimal template release. This configuration during the calcination elucidates that template removal involves more reactions than initially thought. Indeed, thermal decomposition studies show that template oxidation catalyzes the formation of dimeric bonds, such as Cu-O-Ce and Cu-O-Al, see chapter 6, which are not commonly observed in aqueous preparations. For instance, oxidation reaction of azides, polyglycols and alkyl chains with the support material and absorbers had a profound influence on the performance of the catalyst. This fact shows that the organic template not only works as a porous agent in this work, but also drives the formation of crucial catalytic sites during the calcination. Therefore, functionalities of the template, such as alkyl, glycol and azide, could be more important than structural materials, because the formation of metal oxides is influenced by the oxidation of these organic groups.

In fact, as seen in the last part of the fabrication chapter, thermal treatment conditions have a strong influence on the De-NO$_x$ performance of the catalyst. For instance, higher heating rates (>5°C/min) turn into reduction of copper centers and agglomeration of metallic copper particles, because metallic compounds react faster than organic ones. Conversely, lower heating rates facilitate the oxidation and volatilization of organic compounds, which promote the formation of porous channels and the activation of copper centers.

Using a slow calcination ramp produces monoliths with regular porosity, as shown in chapter 5. In addition, formation of cracks was avoided by setting the heating rate to under +1°C/min. But additional parallel effects were observed during the structural analysis of the active sites. As depicted in chapter 6, the active sites of the catalyst were not only isolated copper ions but also defects on the metal oxides and dimeric oxide bonds. Actually, dimeric clusters between cerium and coppers were more sensitive to NO than the isolated copper clusters. Therefore, the pace of the reaction during the thermal step was critical for the formation of these active dimeric centers.

Utilization of organic templates for generation of porosities also generates defects on the crystal structures of the catalyst. This was observed in the spectroscopy analysis in chapter 6 and in some cases referred to as oxygen vacancies. Indeed, these vacancies favored the absorption site for NO at low temperature range and its release at over 200°C. This mechanism is suspected to activate the redox cycle, $Ce^{+3} \leftrightarrow C^{+4}$, which regenerates the active centers in lean conditions, $Cu^{2+} \leftrightarrow Cu^{+}$. Hence, template oxidation leads to oxygen vacancies, which might be responsible for the regeneration of the active center in the catalyst.

Previous statements indicate that organometallic reactions were crucial throughout the fabrication process of the catalyst. However, reaction pathways in organometallic chemistry are extremely complex and uncertain. For this reason, organic templates were used mainly as porosity agents, omitting the side reactions for simplicity. This assumption facilitates the design of the process, as explained in chapter 2. In fact, the selection of materials for the catalyst was done following zeolite synthesis. By doing so, the development process was sped up by using commercially available materials. This facilitated the fulfilment of economic and environmental requirements for this project. Hence, the fabrication of monoliths using foundations of zeolite synthesis was a successful way to accomplish applied catalytic filters.

7.2 Operative Results

Functional testing of the catalyst facilitates the screening of suitable templates for the catalyst encapsulation. An organic complex with nitrogen functionalities was used as the template, because reduced copper was desired at the end of the synthesis. Out of amines, azoles, oxazoles and imines, encapsulation with azido complex, more precisely pyrazole, was the most effective templating agent. Even though the synthesis of copper complexes with pyrazoles requires extreme precautions in comparison to the other complexes, this careful treatment produced superior catalysts.

NO_x conversion at low temperatures requires not only highly active sites but also absorption sites for ammonia and NO. Particularly NO needs to be absorbed, because during operation NO_x peaks and cool gases might suddenly appear. In consequence, two NO absorbers, oxides from Ce and Ti respectively, were tested in combination with the support materials. To sum up, the addition of ceria in the support significantly enhances the performance of the catalyst more than titanium does. Moreover, the spectral analysis revealed that dimeric species of ceria and copper oxides were more active toward NO than isolated copper species. Therefore,

inclusion of CeO_2 in the support was a key factor in the performance of the catalyst at low temperature.

In some applications overstoichiometric combustion leads to low NO_x conversion because oxygen competes with NOx for absorption sites. Fortunately, this effect was overcome through the addition of TiO_2 and CeO_2 in the support material in this work. This doping of the filter material increased the oxygen vacancies and hence the NO_x absorption sites for NO. This fact promoted the oxidation of NO to NO_2, which finally improved the general NO_x conversion at low temperature.

Filtration properties of this monolith were evaluated through exhaust gases from a diesel engine. In this case, the porous structure retained soot at low temperature, thus reducing the emission of soot and hydrocarbons from the engine. Even though the filter was plugged after a couple of hours of operation, regeneration of the catalyst was easily achieved by subsequently heating it up to 500°C. This showed that the active centers of the catalyst can also work with hydrocarbons. Nevertheless, this HC-SCR mechanism achieved only 40% of the NH_3-SCR performance at 200°C.

As seen in figure 5-3, synthesis of catalytic filters through an encapsulation method can be implemented for flue gas cleaning at low temperature. After the evaluation of this encapsulated catalyst, NO_x conversion of up to 80% was achieved at 200°C. This confirms that integrating active material with unreactive supports can attain similar performance as coated catalysts, as long as the catalyst is protected.

7.3   Outlook

Biomass-based thermal processes are opening sustainable ways for energy conversion. This progress also requires the development of suitable aftertreatment systems for these new exhaust gases. Consequently, to supply a clean deployment of these technologies, a corrosion resistant catalytic filter was developed in this work to perform De-NOx in dusty and hydrothermal conditions. This catalyst was specifically manufactured in order to deal with the complex conditions of exhaust gases from biomass processes. Moreover, its operation temperature, around 200°C, facilitates their implementation in small and medium furnaces. For instance, decentralized power plants, incinerators, boilers – among other low scale firing systems – can fulfil upcoming air emission standards through these catalytic filters.

Additionally, the compact catalyst could be installed in already working systems. Due to the cylindrical geometry of the catalytic filter, see figure 7-1, integration of the catalyst in a

standard pipeline does not involve additional developments. However, highly dusty flows must be treated carefully.

Indeed, dust filtration requires additional regeneration and disposal of accumulated solids, otherwise dust accumulates gradually. This accumulation progressively forms a particle cake, which builds up alarming pressure in the reactor. Therefore, particle collectors and backflush systems are needed for dust treatment in order to reduce the pressure drop at high volumetric flow conditions.

Mechanical stability of the catalyst was basically controlled by the inorganic binder and the pressure during shaping. It was not possible to estimate exact values for the process because mechanical stability depends on external conditions, such as vibration and flow speed. Looking at future development, in situ parameters need to be defined clearly, in order to assess the required strength of the monolith. Hence, further research and development of mechanical properties are required for these kinds of ceramic bodies.

Encapsulation of catalytical material with inert support was developed for flue gas cleaning in this work. But the technique can also be extended to other application fields, where treatments of gases with entrained particles are critical. For instance, processes with multiphasic flow might be successfully processed by filters with encapsulated catalysts.

8 Bibliography

[1]   T. Nussbaumer and M. Oser, *Evaluation of Biomass Combustion Based Energy Systems by Cumulative Energy Demand and Energy Yield Coefficient: Final Report Prepared for International Energy Agency (IEA), Bioenergy Task 32: Biomass Combustion and Co-firing and Swiss Federal Office of Energy (SFOE)*. Verenum, 2004.

[2]   M. Obaidullah, S. Bram, V. Verma, and J. De Ruyck, "A review on particle emissions from small scale biomass combustion," *International Journal of Renewable Energy Research (IJRER)*, vol. 2, no. 1, pp. 147–159, 2012.

[3]   D.-G. JRC, "Integrated Pollution Prevention and Control (IPPC) Reference Document on Best Available Techniques in the Large Volume Organic Chemical Industry," 2002.

[4]   S. Heidenreich, M. Nacken, M. Hackel, and G. Schaub, "Catalytic filter elements for combined particle separation and nitrogen oxides removal from gas streams," *Powder Technology*, vol. 180, no. 1, pp. 86–90, 2008.

[5]   M. Nacken, S. Heidenreich, M. Hackel, and G. Schaub, "Catalytic activation of ceramic filter elements for combined particle separation, NO x removal and VOC total oxidation," *Applied Catalysis B: Environmental*, vol. 70, no. 1, pp. 370–376, 2007.

[6]   J.-H. Choi, S.-K. Kim, and Y.-C. Bak, "The reactivity of V2O5-WO3-TiO2 catalyst supported on a ceramic filter candle for selective reduction of NO," *Korean Journal of Chemical Engineering*, vol. 18, no. 5, pp. 719–724, 2001.

[7]   M. Lapuerta, J. Rodr'\iguez-Fernández, and F. Oliva, "Effect of soot accumulation in a diesel particle filter on the combustion process and gaseous emissions," *Energy*, vol. 47, no. 1, pp. 543–552, 2012.

[8]   Q. Zhou, K. Zhong, W. Fu, Q. Huang, Z. Wang, and B. Nie, "Nanostructured platinum catalyst coating on diesel particulate filter with a low-cost electroless deposition approach," *Chemical Engineering Journal*, vol. 270, pp. 320–326, 2015.

[9]   C.-Y. Chen, W.-J. Lee, L.-C. Wang, Y.-C. Chang, H.-H. Yang, L.-H. Young, J.-H. Lu, Y. I. Tsai, M.-T. Cheng, and J. K. Mwangi, "Impact of high soot-loaded and regenerated diesel particulate filters on the emissions of persistent organic pollutants from a diesel engine fueled with waste cooking oil-based biodiesel," *Applied Energy*, vol. 191, pp. 35–43, 2017.

[10] J. Chun-Te Lin, T.-C. Hsiao, S.-S. Hsiau, D.-R. Chen, Y.-K. Chen, S.-H. Huang, C.-C. Chen, and M.-B. Chang, "Effects of temperature, dust concentration, and filtration superficial velocity on the loading behavior and

dust cakes of ceramic candle filters during hot gas filtration," *Separation and Purification Technology*, 2017.

[11] A. für erneuerbare Energien eV, "Erneuerbare Energien 2020-Potenzialatlas Deutschland," 2010.

[12] P. Heck, T. Anton, J. Böhmer, P. Huwig, J. Meisberger, S. Menze, C. Pietz, A. Reis, S. Schierz, C. Synwoldt, and others, "Bioenergiedörfer-Leitfaden für eine praxisnahe Umsetzung," *Gülzow-Prüzen: FNR (Hrsg.)*, 2014.

[13] A. Williams, J. Jones, L. Ma, and M. Pourkashanian, "Pollutants from the combustion of solid biomass fuels," *Progress in Energy and Combustion Science*, vol. 38, no. 2, pp. 113–137, 2012.

[14] E. Fitzpatrick, K. Bartle, M. L. Kubacki, J. Jones, M. Pourkashanian, A. Ross, A. Williams, and K. Kubica, "The mechanism of the formation of soot and other pollutants during the co-firing of coal and pine wood in a fixed bed combustor," *Fuel*, vol. 88, no. 12, pp. 2409–2417, 2009.

[15] J. Wilson, M. Baeza-Romero, J. Jones, M. Pourkashanian, A. Williams, A. Lea-Langton, A. Ross, and K. Bartle, "Soot formation from the combustion of biomass pyrolysis products and a hydrocarbon fuel, n-decane: an aerosol time of flight mass spectrometer (ATOFMS) study," *Energy \& Fuels*, vol. 27, no. 3, pp. 1668–1678, 2013.

[16] I. Lusini, "Emissions of volatile organic compounds (VOCs) from biomass burning," 2015.

[17] R. Koppmann, K. von Czapiewski, and J. Reid, "A review of biomass burning emissions, part I: gaseous emissions of carbon monoxide, methane, volatile organic compounds, and nitrogen containing compounds," *Atmospheric Chemistry and Physics Discussions*, vol. 5, no. 5, pp. 10455–10516, 2005.

[18] H. Solo-Gabriele and T. Townsend, *Environmental Impacts of Preservative-Treated Wood*. Taylor \& Francis Group, Boca Raton, 2006.

[19] L. Carvalho, E. Wopienka, C. Pointner, J. Lundgren, V. K. Verma, W. Haslinger, and C. Schmidl, "Performance of a pellet boiler fired with agricultural fuels," *Applied Energy*, vol. 104, no. C, pp. 286–296, 2013.

[20] H. Knoef and J. Ahrenfeldt, *Handbook biomass gasification*. BTG biomass technology group The Netherlands, 2005.

[21] J. Warnatz, U. Maas, and R. Dibble, "Combustion: physical and chemical fundamentals, modeling and simulation, experiments, pollutant formation. 2006."

[22] S. Ghafghazi, T. Sowlati, S. Sokhansanj, X. Bi, and S. Melin, "Particulate matter emissions from combustion of wood in district heating applications," *Renewable and Sustainable Energy Reviews*, vol. 15, no. 6, pp. 3019–3028, 2011.

[23] O. Sippula, "Fine particle formation and emissions in biomass combustion," *Report series in aerosol science*, vol. 108, 2010.

[24] S. Andreoli, "Catalytic processes for the control of nitrogen oxides emissions in the presence of oxygen," 2000.

[25] J. M. Jones, A. R. Lea-Langton, L. Ma, M. Pourkashanian, and A. Williams, *Pollutants Generated by the Combustion of Solid Biomass Fuels*. Springer, 2014.

[26] M. M. Roy, A. Dutta, and K. Corscadden, "An experimental study of combustion and emissions of biomass pellets in a prototype pellet furnace," *Applied Energy*, vol. 108, no. C, pp. 298–307, 2013.

[27] E. Houshfar, T. Løvås, and \Oyvind Skreiberg, "Experimental investigation on NOx reduction by primary measures in biomass combustion: straw, peat, sewage sludge, forest residues and wood pellets," *Energies*, vol. 5, no. 2, pp. 270–290, 2012.

[28] A. Lucassen, K. Zhang, J. Warkentin, K. Moshammer, P. Glarborg, P. Marshall, and K. Kohse-Höinghaus, "Fuel-nitrogen conversion in the combustion of small amines using dimethylamine and ethylamine as biomass-related model fuels," *Combustion and Flame*, vol. 159, no. 7, pp. 2254–2279, 2012.

[29] S. Mahmoudi, J. Baeyens, and J. P. Seville, "NOx formation and selective non-catalytic reduction (SNCR) in a fluidized bed combustor of biomass," *Biomass and bioenergy*, vol. 34, no. 9, pp. 1393–1409, 2010.

[30] S. Qiao, X. Yin, T. Tian, R. Jin, and J. Zhou, "Hydrazine production by anammox biomass with NO reversible inhibition effects," *Green Chemistry*, 2016.

[31] H. Zhan, X. Yin, Y. Huang, H. Yuan, and C. Wu, "NOx precursors evolving during rapid pyrolysis of lignocellulosic industrial biomass wastes," *Fuel*, vol. 207, pp. 438–448, 2017.

[32] S. Alegret, A. Merkoçi, D. Barceló, A. Lewenstam, A. Radu, D. Diamond, R.-I. Stefan-van Staden, J. Bobacka, A. Ivaska, T. Wagner, and others, *Comprehensive analytical chemistry*. Elsevier, 2003.

[33] R. Peters, *Cooperative catalysis: designing efficient catalysts for synthesis*. John Wiley \& Sons, 2015.

[34] T. Luft, "Erste Allgemeine Verwaltungsvorschrift zum Bundes-Immissionsschutzgesetz (Technische Anleitung zur Reinhaltung der Luft-TA Luft)," *Vom*, vol. 24, pp. 25–29, 2002.

[35] N. Oxides, "Why and How they are Controlled," *Clean Air Technology Center (MD-12), US EPA Technical Bulletin No. EPA-456/F-99-006R. http://www. epa. gov/ttncatc1/dir1/fnoxdoc. pdf*, 1999.

[36] H. Liu, J. Chaney, J. Li, and C. Sun, "Control of NOx emissions of a domestic/small-scale biomass pellet boiler by air staging," *Fuel*, vol. 103, pp. 792–798, 2013.

[37] K. Skalska, J. S. Miller, and S. Ledakowicz, "Trends in NO x abatement: A review," *Science of the Total Environment*, vol. 408, no. 19, pp. 3976–3989, 2010.

[38] S. Andreoli, "Catalytic processes for the control of nitrogen oxides emissions in the presence of oxygen," 2016.

[39] C. A. Tsiliyannis, "Flue gas recirculation and enhanced performance of waste incinerators under waste uncertainty.," *Environ. Sci. Technol.*, vol. 47, no. 14, pp. 8051–61, 2013.

[40] X. Wang, Q. Ren, W. Li, H. Li, S. Li, and Q. Lu, "Nitrogenous Gas Emissions from Coal/Biomass Co-combustion under a High Oxygen Concentration in a Circulating Fluidized Bed," *Energy \& Fuels*, vol. 31, no. 3, pp. 3234–3242, 2017.

[41] I. Obernberger, T. Brunner, and G. Bärnthaler, "Chemical properties of solid biofuels—significance and impact," *Biomass and Bioenergy*, vol. 30, no. 11, pp. 973–982, 2006.

[42] I. Nova and E. Tronconi, *Urea-SCR technology for deNOx after treatment of diesel exhausts*. Springer, 2014.

[43] J. G. Amores, V. S. Escribano, G. Ramis, and G. Busca, "An FT-IR study of ammonia adsorption and oxidation over anatase-supported metal oxides," *Applied Catalysis B: Environmental*, vol. 13, no. 1, pp. 45–58, 1997.

[44] M. Rutkowska, "Catalytic decomposition of N 2 O using a new generation of functionalized microporous and mesoporous inorganic materials," *Wiadomo'sci Chemiczne*, 2015.

[45] C. K. Narula, C. S. Daw, J. W. Hoard, and T. Hammer, "Materials issues related to catalysts for treatment of diesel exhaust," *International journal of applied ceramic technology*, vol. 2, no. 6, pp. 452–466, 2005.

[46]   G. Liu and P.-X. Gao, "A review of NO x storage/reduction catalysts: mechanism, materials and degradation studies," *Catalysis Science \& Technology*, vol. 1, no. 4, pp. 552–568, 2011.

[47]   B. Liu, J. Liu, S. Ma, Z. Zhao, Y. Chen, X.-Q. Gong, W. Song, A. Duan, and G. Jiang, "Mechanistic Study of Selective Catalytic Reduction of NO with NH3 on W-doped CeO2 Catalysts: Unraveling the Catalytic Cycle and the Role of Oxygen Vacancy," *The Journal of Physical Chemistry C*, 2016.

[48]   L. Arnarson, H. Falsig, S. B. Rasmussen, J. V. Lauritsen, and P. G. Moses, "A complete reaction mechanism for standard and fast selective catalytic reduction of nitrogen oxides on low coverage VOx/TiO 2 (001) catalysts," *Journal of Catalysis*, vol. 346, pp. 188–197, 2017.

[49]   R. Singh and A. Shukla, "A review on methods of flue gas cleaning from combustion of biomass," *Renewable and Sustainable Energy Reviews*, vol. 29, pp. 854–864, 2014.

[50]   P. Hasler and T. Nussbaumer, "Gas cleaning for IC engine applications from fixed bed biomass gasification," *Biomass and Bioenergy*, vol. 16, no. 6, pp. 385–395, 1999.

[51]   E. Simeone, E. Hölsken, M. Nacken, S. Heidenreich, and W. De Jong, "Study of the behaviour of a catalytic ceramic candle filter in a lab-scale unit at high temperatures," *International Journal of Chemical Reactor Engineering*, vol. 8, no. 1, 2010.

[52]   M. Nacken, L. Ma, S. Heidenreich, and G. V. Baron, "Performance of a catalytically activated ceramic hot gas filter for catalytic tar removal from biomass gasification gas," *Applied Catalysis B: Environmental*, vol. 88, no. 3, pp. 292–298, 2009.

[53]   M. Gálvez, S. Ascaso, I. Tob'\ias, R. Moliner, and M. Lázaro, "Catalytic filters for the simultaneous removal of soot and NO x: Influence of the alumina precursor on monolith washcoating and catalytic activity," *Catalysis today*, vol. 191, no. 1, pp. 96–105, 2012.

[54]   R. M. Kakwani, K. C. Voss, J. A. Patchett, and K. R. Grimston, "Exhaust system for enhanced reduction of nitrogen oxides and particulates from diesel engines," 2004.

[55]   J. Yan, *Comprehensive Evaluation of Effective Biomass Resource Utilization and Optimal Environmental Policies*. Springer, 2015.

[56]   K. Li, *Study of Influence Factors in Municipal Solid Waste Management Decision-making*. 2007.

[57] S. Saxena and C. Jotshi, "Management and combustion of hazardous wastes," *Progress in Energy and Combustion Science*, vol. 22, no. 5, pp. 401–425, 1996.

[58] J. Kemsley, "New hazardous waste incinerator comes online."

[59] J. Matthey, "SINOx® Catalysts," *SINOx® Emissions Control*, vol. 16, no. 1, pp. 187–191, 2001.

[60] L. Baxter, "Biomass Impacts on SCR Catalyst Performance," *IEA Bioenergy Task 32, Technical Report*, p. 89, 2005.

[61] X. Guo, "Poisoning and sulfation on vanadia SCR catalyst," 2006.

[62] S. Xiong, J. Wen, Y. Liao, B. Li, S. Zou, Y. Gen, X. Xiao, N. Huang, and S. Yang, "Alkali Metal Deactivation on the Low Temperature Selective Catalytic Reduction of NOx With NH3 Over MnOx-CeO2: A Mechanism Study," *The Journal of Physical Chemistry C*, 2016.

[63] S. Sakka, *Handbook of sol-gel science and technology. 1. Sol-gel processing*, vol. 1. Springer Science \& Business Media, 2005.

[64] J. Regalbuto, *Catalyst preparation: science and engineering*. CRC Press, 2006.

[65] A. Montebelli, C. G. Visconti, G. Groppi, E. Tronconi, C. Cristiani, C. Ferreira, and S. Kohler, "Methods for the catalytic activation of metallic structured substrates," *Catalysis Science \& Technology*, vol. 4, no. 9, pp. 2846–2870, 2014.

[66] B. Ramachandran, R. G. Herman, S. Choi, H. G. Stenger, C. E. Lyman, and J. W. Sale, "Protocol for Laboratory Testing of SCR Catalyst Samples:," *Catalysis Today*, vol. 55, no. 3, pp. 281–290, 2007.

[67] K. W. Kasongo and B. Jean, "Synthesis and characterization of micro-and mesoporous materials for low temperature selective catalytic reduction of nitrogen oxides," 2011.

[68] A. Godiksen, P. N. Vennestrøm, S. B. Rasmussen, and S. Mossin, "Identification and Quantification of Copper Sites in Zeolites by Electron Paramagnetic Resonance Spectroscopy," *Topics in Catalysis*, vol. 60, no. 1–2, pp. 13–29, 2017.

[69] I. Lezcano-Gonzalez, D. S. Wragg, W. A. Slawinski, K. Hemelsoet, A. Van Yperen-De Deyne, M. Waroquier, V. Van Speybroeck, and A. M. Beale, "Determination of the Nature of the Cu Coordination Complexes Formed in the Presence of NO and NH3 within SSZ-13," *The Journal of Physical Chemistry*

C, vol. 119, no. 43, pp. 24393–24403, 2015.

[70] G. R. Chandler, K. A. Flanagan, P. R. Phillips, P. Schofield, M. L. W. Spencer, and H. M. Strutt, "Coating a monolith substrate with catalyst component 1," 2014.

[71] L. N Protasova, M. HJM de Croon, and V. Hessel, "Review of patent publications from 1990 to 2010 on catalytic coatings on different substrates, including microstructured channels: preparation, deposition techniques, applications," *Recent Patents on Chemical Engineering*, vol. 5, no. 1, pp. 28–44, 2012.

[72] J. M. Fisher, R. R. Rajaram, D. Thompsett, and J. E. Collier, "Selective catalytic reduction processes using doped cerias," 2017.

[73] Z. G. Liu, M. P. Henrichsen, W. C. Haberkamp, E. M. Yorkgitis, R. K. Miller, T. E. Wood, Z. Tan, and B. M. Verdegan, "High temperature nanofilter, system and method," 2006.

[74] V. Meille, "Review on methods to deposit catalysts on structured surfaces," *Applied Catalysis A: General*, vol. 315, pp. 1–17, 2006.

[75] S. Misumi, H. Yoshida, A. Matsumoto, S. Hinokuma, T. Sato, and M. Machida, "Thermal evolution of the structure and activity of Rh overlayer catalysts prepared by pulsed arc-plasma deposition," *Topics in Catalysis*, pp. 1–7, 2017.

[76] F. Akhtar, L. Andersson, S. Ogunwumi, N. Hedin, and L. Bergström, "Structuring adsorbents and catalysts by processing of porous powders," *Journal of the European Ceramic Society*, vol. 34, no. 7, pp. 1643–1666, 2014.

[77] G. Fischer, "EXTRUSION," *Solar energy materials and solar cells*, 2004. [Online]. Available: https://www.ikts.fraunhofer.de/en/departments/structural_ceramics/processes_and_components/shaping/extrusion.html. [Accessed: 21-2017].

[78] M. Konarova, W. Aslam, L. Ge, Q. Ma, F. Tang, V. Rudolph, and J. N. Beltramini, "Enabling process intensification via 3D printing of catalytic structures," *ChemCatChem*.

[79] A. Zhakeyev, P. Wang, L. Zhang, W. Shu, H. Wang, and J. Xuan, "Additive Manufacturing: Unlocking the Evolution of Energy Materials," *Advanced Science*, 2017.

[80] K. Zhang and M. L. Ostraat, "Innovations in hierarchical zeolite synthesis," *Catalysis Today*, vol. 264, pp. 3–15, 2016.

[81] X.-Y. Yang, L.-H. Chen, Y. Li, J. C. Rooke, C. Sanchez, and B.-L. Su, "Hierarchically porous materials: synthesis strategies and structure design,"

Chemical Society Reviews, 2017.

[82] D. T. On, D. Desplantier-Giscard, C. Danumah, and S. Kaliaguine, "Perspectives in catalytic applications of mesostructured materials," *Applied Catalysis A: General*, vol. 253, no. 2, pp. 545–602, 2003.

[83] S. Dutta, A. Bhaumik, and K. C.-W. Wu, "Hierarchically porous carbon derived from polymers and biomass: effect of interconnected pores on energy applications," *Energy \& Environmental Science*, vol. 7, no. 11, pp. 3574–3592, 2014.

[84] R. Nisticò, D. Scalarone, and G. Magnacca, "Sol-gel chemistry, templating and spin-coating deposition: A combined approach to control in a simple way the porosity of inorganic thin films/coatings," *Microporous and Mesoporous Materials*, 2017.

[85] V. G. Baldovino-Medrano, M. T. Le, I. Van Driessche, E. Bruneel, C. Alcázar, M. T. Colomer, R. Moreno, A. Florencie, B. Farin, and E. M. Gaigneaux, "Role of shaping in the preparation of heterogeneous catalysts: Tableting and slip-casting of oxidation catalysts," *Catalysis Today*, vol. 246, pp. 81–91, 2015.

[86] F. Svec, T. B. Tennikova, and Z. Deyl, *Monolithic materials: preparation, properties and applications*, vol. 67. Elsevier, 2003.

[87] A. Ojuva, F. Akhtar, A. P. Tomsia, and L. Bergström, "Laminated adsorbents with very rapid CO2 uptake by freeze-casting of zeolites," *ACS applied materials \& interfaces*, vol. 5, no. 7, pp. 2669–2676, 2013.

[88] X. Ma, H. Sun, and P. Yu, "A novel way for preparing high surface area silica monolith with bimodal pore structure," *Journal of materials science*, vol. 43, no. 3, pp. 887–891, 2008.

[89] beller Matthias and A. Renken, "Catalysis. From Principles to Applications. By Matthias Beller, Albert Renken and Rutger A. van Santen.," 2013.

[90] R. P. Vélez, "Structural Characterization of Iron Species in Fe-ZSM-5 Catalysts and the Elucidation of Their Role in the Mechanism of NO X Reactions," 2015.

[91] H. Zheng, W. Song, Y. Zhou, S. Ma, J. Deng, Y. Li, J. Liu, and Z. Zhao, "Mechanistic Study of Selective Catalytic Reduction of NOx with NH3 over Mn-TiO2: A Combination of Experimental and DFT Study," *The Journal of Physical Chemistry C*, 2017.

[92] T. V. Janssens, H. Falsig, L. F. Lundegaard, P. N. R. Vennestrøm, S. Rasmussen, P. G. Moses, F. Giordanino, E. Borfecchia, K. A. Lomachenko, C. Lamberti, and others, "A consistent reaction scheme for the selective catalytic reduction of nitrogen oxides with ammonia," *ACS Catalysis*, 2015.

[93]   Y. Li, J. Deng, W. Song, J. Liu, Z. Zhao, M. Gao, Y. Wei, and L. Zhao, "Nature of Cu Species in Cu-SAPO-18 Catalyst for NH3-SCR: Combination of Experiments and DFT Calculations," *The Journal of Physical Chemistry C*, vol. 120, no. 27, pp. 14669–14680, 2016.

[94]   M. Gruber, "The selective catalytic reduction of NO by NH3 at Brønsted and Lewis acid sites of vanadium oxide surfaces: Density functional theory studies," 2012.

[95]   F. Gao, D. Mei, Y. Wang, J. Szanyi, and C. H. Peden, "Selective Catalytic Reduction over Cu/SSZ-13: Linking Homo-and Heterogeneous Catalysis," *Journal of the American Chemical Society*, vol. 139, no. 13, pp. 4935–4942, 2017.

[96]   J. A. Schaidle, S. E. Habas, F. G. Baddour, C. A. Farberow, D. A. Ruddy, J. E. Hensley, R. L. Brutchey, N. Malmstadt, and H. Robota, "Transitioning rationally designed catalytic materials to real 'working' catalysts produced at commercial scale: nanoparticle materials," in *Catalysis*, 2017, pp. 213–281.

[97]   G. Busca, "Chapter 6 - Metal Oxides as Acid-Base Catalytic Materials ," in *Heterogeneous Catalytic Materials* , Busca, Guido , Ed. Amsterdam: Elsevier, 2014, pp. 103 – 195.

[98]   X. Du, X. Gao, W. Hu, J. Yu, Z. Luo, and K. Cen, "Catalyst Design Based on DFT Calculations: Metal Oxide Catalysts for Gas Phase NO Reduction," *The Journal of Physical Chemistry C*, vol. 118, no. 25, pp. 13617–13622, 2014.

[99]   Z. Sun, Q. Wang, Y. Xu, and Z. Wang, "A computationally designed titanium-mediated amination of allylic alcohols for the synthesis of secondary allylamines," *RSC Advances*, vol. 5, no. 102, pp. 84284–84289, 2015.

[100] M. P. Andersson, T. Bligaard, A. Kustov, K. E. Larsen, J. Greeley, T. Johannessen, C. H. Christensen, and J. K. Nørskov, "Toward computational screening in heterogeneous catalysis: Pareto-optimal methanation catalysts," *Journal of Catalysis*, vol. 239, no. 2, pp. 501–506, 2006.

[101] S. A. Bates, A. A. Verma, C. Paolucci, A. A. Parekh, T. Anggara, A. Yezerets, W. F. Schneider, J. T. Miller, W. N. Delgass, and F. H. Ribeiro, "Identification of the active Cu site in standard selective catalytic reduction with ammonia on Cu-SSZ-13," *Journal of Catalysis*, vol. 312, pp. 87–97, 2014.

[102] N. Krause, *Modern organocopper chemistry*. John Wiley \& Sons, 2002.

[103] S. Routier, J.-L. Bernier, M. J. Waring, P. Colson, C. Houssier, and C. Bailly, "Synthesis of a functionalized Salen- Copper complex and its interaction with DNA," *The Journal of Organic Chemistry*, vol. 61, no. 7, pp. 2326–2331, 1996.

[104] R. M. Gschwind, "Organocuprates and diamagnetic copper complexes: Structures and NMR spectroscopic structure elucidation in solution," *Chemical reviews*, vol. 108, no. 8, pp. 3029–3053, 2008.

[105] N. Yoshikai and E. Nakamura, "Mechanisms of nucleophilic organocopper (I) reactions," *Chemical reviews*, vol. 112, no. 4, pp. 2339–2372, 2011.

[106] I. Bull, U. Müller, and B. Yilmaz, "Copper Containing Levyne Molecular Sieve For Selective Reduction Of NOx," 2010.

[107] P. Karthikeyan, S. A. Aswar, P. N. Muskawar, P. R. Bhagat, and S. S. Kumar, "Development and efficient 1-glycyl-3-methyl imidazolium chloride-copper (II) complex catalyzed highly enantioselective synthesis of 3, 4-dihydropyrimidin-2 (1H)-ones," *Journal of Organometallic Chemistry*, vol. 723, pp. 154–162, 2013.

[108] E. Shilpa and V. Gayathri, "Encapsulation of Cu (II)[2-(2′-hydroxyphenyl) benzimidazole] 2 within zeolite nano-cavity: Structural properties and its catalytic activity towards phenol and styrene oxidation," *Journal of Environmental Chemical Engineering*, 2016.

[109] T. Vergunst, F. Kapteijn, and J. A. Moulijn, "Monolithic catalysts—non-uniform active phase distribution by impregnation," *Applied Catalysis A: General*, vol. 213, no. 2, pp. 179–187, 2001.

[110] C. M. Crudden, M. Sateesh, and R. Lewis, "Mercaptopropyl-modified mesoporous silica: A remarkable support for the preparation of a reusable, heterogeneous palladium catalyst for coupling reactions," *Journal of the American Chemical Society*, vol. 127, no. 28, pp. 10045–10050, 2005.

[111] A. Wahlberg, L. J. Pettersson, K. Bruce, M. Andersson, and K. Jansson, "Preparation, evaluation and characterization of copper catalysts for ethanol fuelled diesel engines," *Applied Catalysis B: Environmental*, vol. 23, no. 4, pp. 271–281, 1999.

[112] P. Sonstrom, M. Adam, X. Wang, M. Wilhelm, G. Grathwohl, and M. Baumer, "Colloidal nanoparticles embedded in ceramers: toward structurally designed catalysts," *The Journal of Physical Chemistry C*, vol. 114, no. 33, pp. 14224–14232, 2010.

[113] A.-M. Siouffi, "Silica gel-based monoliths prepared by the sol-gel method: facts and figures," *Journal of Chromatography A*, vol. 1000, no. 1, pp. 801–818, 2003.

[114] J. Liu, S. B. Hartono, Y. G. Jin, Z. Li, G. Q. M. Lu, and S. Z. Qiao, "A facile vesicle template route to multi-shelled mesoporous silica hollow nanospheres," *Journal of Materials Chemistry*, vol. 20, no. 22, pp. 4595–4601, 2010.

[115] O. Sel, D. Kuang, M. Thommes, and B. Smarsly, "Principles of hierarchical meso- and macropore architectures by liquid crystalline and polymer colloid templating.," *Langmuir*, vol. 22, no. 5, pp. 2311–22, 2006.

[116] T. Ci, T. Li, L. Chen, G. Chang, L. Yu, and J. Ding, "Effects of 'mature micelle' formation of Pluronic P123 on equilibrium between lactone and carboxylate forms of 10-hydrocamptothecin in water," *Polymer Chemistry*, vol. 4, no. 11, pp. 3245–3255, 2013.

[117] I. S. Han, J. C. Park, S. Y. Kim, and K. S. Hong, "Fabrication of the monolithic silica aerogels using sodium silicate and its network strengthening," in *Key Engineering Materials*, 2008, vol. 368, pp. 790–793.

[118] P. O. Vasiliev, Z. Shen, R. P. Hodgkins, and L. Bergström, "Meso/macroporous, mechanically stable silica monoliths of complex shape by controlled fusion of mesoporous spherical particles," *Chemistry of materials*, vol. 18, no. 20, pp. 4933–4938, 2006.

[119] A. Bazargan, P. Hadi, S. L. Rough, and G. McKay, "The preparation of pellets by the compaction of an aluminosilicate-based adsorbent from electronic waste," *Journal of Environmental Chemical Engineering*, vol. 4, no. 2, pp. 2322–2326, 2016.

[120] W. Pan, Y. Zhou, R. Guo, W. Zhen, J. Hong, H. Xu, Q. Jin, C. Ding, and S. Guo, "Influence of calcination temperature on CeO2-CuO catalyst for the selective catalytic reduction of NO with NH3," *Environmental Progress \& Sustainable Energy*, vol. 33, no. 2, pp. 385–389, 2014.

[121] B. M. Abu-Zied, W. Schwieger, and A. Unger, "Nitrous oxide decomposition over transition metal exchanged ZSM-5 zeolites prepared by the solid-state ion-exchange method," *Applied Catalysis B: Environmental*, vol. 84, no. 1, pp. 277–288, 2008.

[122] I. Jirka, P. Sazama, A. Zikanova, P. Hrabanek, and M. Kocirik, "Low-temperature thermal removal of template from high silica ZSM-5. Catalytic effect of zeolitic framework," *Microporous and Mesoporous Materials*, vol. 137, no. 1, pp. 8–17, 2011.

[123] K. H. Gilbert, R. M. Baldwin, and J. D. Way, "The effect of heating rate and gas atmosphere on template decomposition in silicalite-1," *Industrial \& engineering chemistry research*, vol. 40, no. 22, pp. 4844–4849, 2001.

[124] D. W. Fickel and R. F. Lobo, "Copper coordination in Cu-SSZ-13 and Cu-SSZ-16 investigated by variable-temperature XRD," *The Journal of Physical Chemistry C*, vol. 114, no. 3, pp. 1633–1640, 2009.

[125] W. Di, F. Zhang, and Y. Zhang, "Catalytic removal of organic template from TEA-β zeolite by copper ions," *Microporous and Mesoporous Materials*,

vol. 255, pp. 119–129, 2018.

[126] S. Heng, P. P. S. Lau, K. L. Yeung, M. Djafer, and J.-C. Schrotter, "Low-temperature ozone treatment for organic template removal from zeolite membrane," *Journal of Membrane Science*, vol. 243, no. 1, pp. 69–78, 2004.

[127] S. Goel, "Encapsulating Metal Clusters and Acid Sites within Small Voids: Synthetic Strategies and Catalytic Consequences," 2015.

[128] L. Chen, J. Jansson, M. Skoglundh, and H. Grönbeck, "Mechanism for Solid-State Ion Exchange of Cu+ into Zeolites," *The Journal of Physical Chemistry C*, vol. 120, no. 51, pp. 29182–29189, 2016.

[129] S. Shwan, M. Skoglundh, L. F. Lundegaard, R. R. Tiruvalam, T. V. Janssens, A. Carlsson, and P. N. Vennestrøm, "Solid-State Ion-Exchange of Copper into Zeolites Facilitated by Ammonia at Low Temperature," *ACS Catalysis*, vol. 5, no. 1, pp. 16–19, 2014.

[130] A. K. S. Clemens, A. Shishkin, P.-A. Carlsson, M. Skoglundh, F. J. Mart'\inez-Casado, Z. Matej, O. Balmes, and H. Härelind, "Reaction-driven Ion Exchange of Copper into Zeolite SSZ-13," *Acs Catalysis*, vol. 5, no. 10, pp. 6209–6218, 2015.

[131] Y. Liu, Y. Zheng, M. P. Harold, and D. Luss, "Lean NO X reduction on LNT-SCR dual-layer catalysts by H 2 and CO," *Applied Catalysis B: Environmental*, vol. 132, pp. 293–303, 2013.

[132] M. Piumetti, S. Bensaid, D. Fino, and N. Russo, "Catalysis in Diesel engine NO x aftertreatment: a review," *Catalysis, Structure \& Reactivity*, vol. 1, no. 4, pp. 155–173, 2015.

[133] D. A. Peña, "Development and characterization of mixed oxide catalysts for the selective catalytic reduction of nitric oxide from stationary sources using ammonia," 2003.

[134] M. Iwamoto and H. Yahiro, "Zeolites in the Science and Technology of Nitrogen Monoxide Removal," in *Handbook of Zeolite Science and Technology*, Marcel Dekker Inc New York, 2003, pp. 951–988.

[135] J. A. Anderson, *Supported metals in catalysis*, vol. 11. World Scientific, 2012.

[136] B. C. Gates, L. Guczi, and H. Knözinger, *Metal clusters in catalysis*, vol. 29. Elsevier Amsterdam, 1986.

[137] P. Pietrzyk and Z. Sojkaab, "DFT modeling and spectroscopic investigations into molecular aspects of DeNO x catalysis," *Studies in Surface Science and Catalysis*, vol. 171, pp. 27–65, 2007.

[138] C. Santini, M. Pellei, V. Gandin, M. Porchia, F. Tisato, and C. Marzano, "Advances in copper complexes as anticancer agents," *Chemical reviews*, vol. 114, no. 1, pp. 815–862, 2013.

[139] E. I. Solomon, P. Chen, M. Metz, S.-K. Lee, and A. E. Palmer, "Oxygen binding, activation, and reduction to water by copper proteins," *Angewandte Chemie International Edition*, vol. 40, no. 24, pp. 4570–4590, 2001.

[140] R. Mukherjee, "Coordination chemistry with pyrazole-based chelating ligands: molecular structural aspects," *Coordination Chemistry Reviews*, vol. 203, no. 1, pp. 151–218, 2000.

[141] S. Kashyap, U. P. Singh, A. Singh, P. Kumar, and S. P. Singh, "Synthesis and structural studies of some copper-benzoate complexes," *Transition Metal Chemistry*, vol. 38, no. 5, pp. 573–585,2013.

[142] Y.-R. Lee, J. Kim, and W.-S. Ahn, "Synthesis of metal-organic frameworks: A mini review," *Korean Journal of Chemical Engineering*, vol. 30, no. 9, pp. 1667–1680,2013.

[143] I. Smallwood, *Handbook of organic solvent properties*. Butterworth-Heinemann, 2012.

[144] S. Kaskel, *The chemistry of metal-organic frameworks: synthesis, characterization, and applications*, vol. 2. John Wiley \& Sons, 2016.

[145] D. Vuluga, J. Legros, B. Crousse, and D. Bonnet-Delpon, "Synthesis of pyrazoles through catalyst-free cycloaddition of diazo compounds to alkynes," *Green Chemistry*, vol. 11, no. 2, pp. 156–159, 2009.

[146] B. H. Pearce, H. F. Ogutu, and R. C. Luckay, "Synthesis of pyrazole based pyridine ligands and their use as extractants for nickel (II) and copper (II). Crystal structure of a copper (II)-ligand complex.," *European Journal of Inorganic Chemistry*, 2016.

[147] K. B. Girma, V. Lorenz, S. Blaurock, and F. T. Edelmann, "Coordination Chemistry of Acrylamide. 6 Synthesis and Coordination Compounds of N-Pyrazolylpropanamide-a Versatile Acrylamide-derived Ligand," *Zeitschrift für anorganische und allgemeine Chemie*, vol. 634, no. 2, pp. 267–273, 2008.

[148] B. Barszcz, T. G\lowiak, J. Jezierska, and A. Tomkiewicz, "Synthesis of new pyrazole-containing binuclear and mononuclear Cu (II) complexes: crystal structure, EPR, magnetic and spectroscopic properties," *Polyhedron*, vol. 23, no. 8, pp. 1309–1316, 2004.

[149] F. Yu, "In situ synthesis of mononuclear copper (II) complexes of the new tridentate ligand bis [(3, 5-dimethyl-1H-pyrazol-1-yl) methyl] amine," *Acta Crystallographica Section C: Crystal Structure Communications*, vol. 67, no.

10, pp. m331–m334, 2011.

[150] B. Barszcz, "Coordination properties of didentate N, O heterocyclic alcohols and aldehydes towards Cu (II), Co (II), Zn (II) and Cd (II) ions in the solid state and aqueous solution," *Coordination chemistry reviews*, vol. 249, no. 21, pp. 2259–2276, 2005.

[151] G. von Willingh, H. S. Abbo, and S. J. Titinchi, "Selective oxidation reactions over tri-and tetradentate oxovanadium (IV) complexes encapsulated in zeolite-Y," *Catalysis Today*, vol. 227, pp. 96–104, 2014.

[152] S. L. Hailu, B. U. Nair, M. Redi-Abshiro, R. Aravindhan, I. Diaz, and M. Tessema, "Synthesis, characterization and catalytic application of zeolite based heterogeneous catalyst of iron (III), nickel (II) and copper (II) salen complexes for oxidation of organic pollutants," *Journal of Porous Materials*, vol. 22, no. 5, pp. 1363–1373, 2015.

[153] G. A. Olah and H. C. Lin, "Electrophilic reactions at single bonds. V. Nitration and nitrolysis of alkanes and cycloalkanes with nitronium salts," *Journal of the American Chemical Society*, vol. 93, no. 5, pp. 1259–1261, 1971.

[154] G. W. Gribble, *Metalation of azoles and related five-membered ring heterocycles*, vol. 29. Springer, 2012.

[155] L. Kagedal and S. Akerstrom, "A Method for Coupling Biologically Important Molecules to Polysaccharides," *Acta Chem. Scand*, vol. 24, no. 5, 1970.

[156] S. Jana, B. Dutta, R. Bera, and S. Koner, "Anchoring of copper complex in MCM-41 matrix: A highly efficient catalyst for epoxidation of olefins by tert-BuOOH," *Langmuir*, vol. 23, no. 5, pp. 2492–2496, 2007.

[157] S. Govender and H. B. Friedrich, "Monoliths: A Review of the Basics, Preparation Methods and Their Relevance to Oxidation," *Catalysts*, vol. 7, no. 2, p. 62, 2017.

[158] A. C. Spivey and S. J. Woodhead, ". Synthetic methods. Part (v) Protecting groups," *Annual Reports Section" B"(Organic Chemistry)*, vol. 94, pp. 77–87, 1998.

[159] Y. Zhu, Z. Hua, J. Zhou, L. Wang, J. Zhao, Y. Gong, W. Wu, M. Ruan, and J. Shi, "Hierarchical Mesoporous Zeolites: Direct Self-Assembly Synthesis in a Conventional Surfactant Solution by Kinetic Control over the Zeolite Seed Formation," *Chemistry-A European Journal*, vol. 17, no. 51, pp. 14618–14627, 2011.

[160] G. Ertl, H. Knozinger, J. Weitkamp, and others, *Handbook of heterogeneous catalysis*. VCH, 1997.

[161] N. M. P. S. Ricardo, N. M. P. S. Ricardo, F. de M. L. L. Costa, C. Chaibundit, G. Portale, D. Hermida-Merino, S. Burattini, I. W. Hamley, C. A. Muryn, S. K. Nixon, and S. G. Yeates, "The effect of n-, s- and t-butanol on the micellization and gelation of Pluronic P123 in aqueous solution.," *J Colloid Interface Sci*, vol. 353, no. 2, pp. 482–9, 2011.

[162] C. Suwanchawalit and S. Wongnawa, "Triblock copolymer-templated synthesis of porous TiO2 and its photocatalytic activity," *Journal of Nanoparticle Research*, vol. 12, no. 8, pp. 2895–2906, 2010.

[163] D. Levy and M. Zayat, *The Sol-Gel Handbook: Synthesis, Characterization and Applications, 3-Volume Set*, vol. 1. John Wiley \& Sons, 2015.

[164] A. Inayat, B. Reinhardt, J. Herwig, C. Küster, H. Uhlig, S. Krenkel, E. Raedlein, and D. Enke, "Recent advances in the synthesis of hierarchically porous silica materials on the basis of porous glasses," *New Journal of Chemistry*, vol. 40, no. 5, pp. 4095–4114, 2016.

[165] A. Aranzabal, D. Iturbe, M. Romero-Sáez, M. González-Marcos, J. González-Velasco, and J. González-Marcos, "Optimization of process parameters on the extrusion of honeycomb shaped monolith of H-ZSM-5 zeolite," *Chemical Engineering Journal*, vol. 162, no. 1, pp. 415–423, 2010.

[166] C. M. Rosado-Reyes and J. S. Francisco, "Atmospheric oxidation pathways of propane and its by-products: acetone, acetaldehyde, and propionaldehyde," *Journal of Geophysical Research: Atmospheres*, vol. 112, no. D14, 2007.

[167] F. Bérubé and S. Kaliaguine, "Calcination and thermal degradation mechanisms of triblock copolymer template in SBA-15 materials," *Microporous and Mesoporous Materials*, vol. 115, no. 3, pp. 469–479, 2008.

[168] J. L. Gurav, A. V. Rao, A. P. Rao, D. Nadargi, and S. Bhagat, "Physical properties of sodium silicate based silica aerogels prepared by single step sol-gel process dried at ambient pressure," *Journal of Alloys and Compounds*, vol. 476, no. 1, pp. 397–402, 2009.

[169] R. W. J. M. Hanssen, *On the formation and reactivity of multinuclear silsesquioxane metal complexes*. Technische Universiteit Eindhoven, 2003.

[170] R. Yu, J. Yun, and Y. Kim, "Synthesis And Characterization Of SiO2, SnO2 And TiO2 Metal Oxide Shells Covering Cu2O Particles," *Archives of Metallurgy and Materials*, vol. 60, no. 2, pp. 1159–1163, 2015.

[171] W. Xiaodong, L. Hyeong-Ryeol, L. Shuang, and W. Duan, "Sulfur poisoning and regeneration of MnO x-CeO 2-Al 2 O 3 catalyst for soot oxidation," *Journal of Rare Earths*, vol. 30, no. 7, pp. 659–664, 2012.

[172] A. Shishkin, S. Shwan, T. N. Pingel, E. Olsson, A. Clemens, P.-A. Carlsson, H. Härelind, and M. Skoglundh, "Functionalization of SSZ-13 and Fe-Beta with Copper by NH3 and NO Facilitated Solid-State Ion-Exchange," *Catalysts*, vol. 7, no. 8, p. 232, 2017.

[173] H. Pan, Y. Jian, Y. Yu, C. He, Z. Shen, and H. Liu, "Regeneration and sulfur poisoning behavior of In/H-BEA catalyst for NO x reduction by CH 4," *Applied Surface Science*, 2016.

[174] C. Paolucci, A. A. Verma, S. A. Bates, V. F. Kispersky, J. T. Miller, R. Gounder, W. N. Delgass, F. H. Ribeiro, and W. F. Schneider, "Isolation of the Copper Redox Steps in the Standard Selective Catalytic Reduction on Cu-SSZ-13," *Angewandte Chemie International Edition*, vol. 53, no. 44, pp. 11828–11833, 2014.

[175] S. Shwan, "Metal-exchanged zeolites for NH3-SCR applications-Activity and Deactivation studies," 2014.

[176] A. A. Khan, M. Aho, W. de Jong, P. Vainikka, P. J. Jansens, and H. Spliethoff, "Scale-up study on combustibility and emission formation with two biomass fuels (B quality wood and pepper plant residue) under BFB conditions," *Biomass and Bioenergy*, vol. 32, no. 12, pp. 1311–1321, 2008.

[177] W. S. Kijlstra, J. C. Daamen, J. M. van de Graaf, B. van der Linden, E. K. Poels, and A. Bliek, "Inhibiting and deactivating effects of water on the selective catalytic reduction of nitric oxide with ammonia over MnO x/Al 2 O 3," *Applied Catalysis B: Environmental*, vol. 7, no. 3, pp. 337–357, 1996.

[178] G. J. Bartley, "Identifying Limiters to Low Temperature Catalyst Activity," 2015.

[179] J. Walberer, "Untersuchung und Untersuchung und Optimierung des Betriebsverhaltens eines Blockheizkraftwerks mit biogenen Ersatzkraftstoffen," 2015.

[180] A. Pesiridis, *Automotive exhaust emissions and energy recovery*. Nova Science Publishers, Incorporated, 2014.

[181] S. Fustero, M. Sánchez-Roselló, P. Barrio, and A. Simón-Fuentes, "From 2000 to Mid-2010: a fruitful decade for the synthesis of pyrazoles," *Chemical reviews*, vol. 111, no. 11, pp. 6984–7034, 2011.

[182] R. Liu, Y. Xu, F. Ye, J. Feng, and R. Xu, "Influence of transition metal (Fe, Co, Ag) doping on the MnOx-CeO2/Ti-bearing blast furnace slag catalyst for selective catalytic reduction of NOx with NH3 at low temperature," *New Journal of Chemistry*, 2017.

[183] A. J. Timmons and M. D. Symes, "Converting between the oxides of nitrogen using metal-ligand coordination complexes," *Chemical Society Reviews*, vol.

44, no. 19, pp. 6708–6722, 2015.

[184] T. Andana, M. Piumetti, S. Bensaid, L. Veyre, C. Thieuleux, N. Russo, D. Fino, E. A. Quadrelli, and R. Pirone, "CuO nanoparticles supported by ceria for NOx-assisted soot oxidation: insight into catalytic activity and sintering," *Applied Catalysis B: Environmental*, vol. 216, pp. 41–58, 2017.

[185] T. Boningari, D. K. Pappas, P. R. Ettireddy, A. Kotrba, and P. G. Smirniotis, "Influence of SiO2 on M/TiO2 (M= Cu, Mn, and Ce) Formulations for Low-Temperature Selective Catalytic Reduction of NO x with NH3: Surface Properties and Key Components in Relation to the Activity of NO x Reduction S1," *Industrial \& Engineering Chemistry Research*, vol. 54, no. 8, pp. 2261–2273, 2015.

[186] V. G. Easterling, "The Effects of Ceria Addition on Aging and Sulfation of Lean NOx Traps for Stand Alone and LNT-SCR Applications," 2013.

[187] R. J. Farrauto, L. Dorazio, and C. H. Bartholomew, *Introduction to Catalysis and Industrial Catalytic Processes*. John Wiley \& Sons, 2016.

[188] T. Boningari, P. R. Ettireddy, A. Somogyvari, Y. Liu, A. Vorontsov, C. A. McDonald, and P. G. Smirniotis, "Influence of elevated surface texture hydrated titania on Ce-doped Mn/TiO 2 catalysts for the low-temperature SCR of NOx under oxygen-rich conditions," *Journal of Catalysis*, vol. 325, pp. 145–155, 2015.

[189] D. V. zur D. des Bundes, "Immissionsschutzgesetzes (Verordnung über Großfeuerungs-und Gasturbinenanlagen—13. BImSchV) vom 20," *BGBl. I*, vol. 37, p. 1717, 2004.

[190] T. Du, H. Qu, Q. Liu, Q. Zhong, and W. Ma, "Synthesis, activity and hydrophobicity of Fe-ZSM-5@ silicalite-1 for NH 3-SCR," *Chemical Engineering Journal*, vol. 262, pp. 1199–1207, 2015.

[191] F. Gao, Y. Zheng, R. K. Kukkadapu, Y. Wang, E. D. Walter, B. Schwenzer, J. Szanyi, and C. H. Peden, "Iron Loading Effects in Fe/SSZ-13 NH3-SCR Catalysts: Nature of the Fe Ions and Structure-Function Relationships," *ACS Catalysis*, vol. 6, no. 5, pp. 2939–2954, 2016.

[192] G. Saracco and V. Specchia, "Catalytic ceramic filters for flue gas cleaning. 2. Catalytic performance and modeling thereof," *Industrial \& engineering chemistry research*, vol. 34, no. 4, pp. 1480–1487, 1995.

[193] Y. Tang, Y.-G. Wang, J.-X. Liang, and J. Li, "Investigation of water adsorption and dissociation on Au1/CeO2 single-atom catalysts using density functional theory," *Chinese Journal of Catalysis*, vol. 38, no. 9, pp. 1558–1565, 2017.

[194] M. P. Ruggeri, I. Nova, E. Tronconi, J. A. Pihl, T. J. Toops, and W. P. Partridge, "In-situ DRIFTS measurements for the mechanistic study of NO oxidation over a commercial Cu-CHA catalyst," *Applied Catalysis B: Environmental*, vol. 166, pp. 181–192, 2015.

[195] M. Devadas, O. Kröcher, M. Elsener, A. Wokaun, N. Söger, M. Pfeifer, Y. Demel, and L. Mussmann, "Influence of NO 2 on the selective catalytic reduction of NO with ammonia over Fe-ZSM5," *Applied Catalysis B: Environmental*, vol. 67, no. 3, pp. 187–196, 2006.

[196] D. W. Kwon and S. C. Hong, "Promotional effect of tungsten-doped CeO 2/TiO 2 for selective catalytic reduction of NOx with ammonia," *Applied Surface Science*, vol. 356, pp. 181–190, 2015.

[197] N. D. Wasalathanthri, T. M. SantaMaria, D. A. Kriz, S. L. Dissanayake, C.-H. Kuo, S. Biswas, and S. L. Suib, "Mesoporous Manganese Oxides for NO 2 Assisted Catalytic Soot Oxidation," *Applied Catalysis B: Environmental*, 2016.

[198] S. J. Schmieg, S. H. Oh, C. H. Kim, D. B. Brown, J. H. Lee, C. H. Peden, and D. H. Kim, "Thermal durability of Cu-CHA NH 3-SCR catalysts for diesel NO x reduction," *Catalysis Today*, vol. 184, no. 1, pp. 252–261, 2012.

[199] M. Moreno-González, A. E. Palomares, M. Chiesa, M. Boronat, E. Giamello, and T. Blasco, "Evidence of a Cu2+-Alkane Interaction in Cu-Zeolite Catalysts Crucial for the Selective Catalytic Reduction of NO x with Hydrocarbons," *ACS Catalysis*, vol. 7, no. 5, pp. 3501–3509, 2017.

[200] J. Villeneuve, J. H. Palacios, P. Savoie, and S. Godbout, "A critical review of emission standards and regulations regarding biomass combustion in small scale units (< 3MW)," *Bioresource technology*, vol. 111, pp. 1–11, 2012.

[201] Z. Wang, Z. Qu, X. Quan, Z. Li, H. Wang, and R. Fan, "Selective catalytic oxidation of ammonia to nitrogen over CuO-CeO 2 mixed oxides prepared by surfactant-templated method," *Applied Catalysis B: Environmental*, vol. 134, pp. 153–166, 2013.

[202] Z. Chen, Z. Si, L. Cao, X. Wu, R. Ran, and D. Weng, "Decomposition behavior of ammonium nitrate on ceria catalysts and its role in the NH 3-SCR reaction," *Catalysis Science \& Technology*, vol. 7, no. 12, pp. 2531–2541, 2017.

[203] O. Mihai, S. Tamm, M. Stenfeldt, and L. Olsson, "The effect of soot on ammonium nitrate species and NO2 selective catalytic reduction over Cu-zeolite catalyst-coated particulate filter," *Phil. Trans. R. Soc. A*, vol. 374, no. 2061, p. 20150086, 2016.

[204] O. Mihai, S. Tamm, M. Stenfeldt, and L. Olsson, "The effect of soot on ammonium nitrate species and NO2 selective catalytic reduction over Cu-zeolite catalyst-coated particulate filter," *Phil. Trans. R. Soc. A*, vol. 374, no.

2061, p. 20150086, 2016.

[205] M. E. Davis, J. Garc'\ia-Mart'\inez, and K. Li, *Mesoporous Zeolites: Preparation, Characterization and Applications*. John Wiley \& Sons, 2015.

[206] Y. Yampolskii and B. Freeman, *Membrane gas separation*, vol. 34. Wiley Online Library, 2010.

[207] Z. Li, "New micro and mesoporous materials for the reaction of methanol to olefins," 2014.

[208] Q. Li, M. L. Amweg, C. K. Yee, A. Navrotsky, and A. N. Parikh, "Photochemical template removal and spatial patterning of zeolite MFI thin films using UV/ozone treatment," *Microporous and mesoporous materials*, vol. 87, no. 1, pp. 45–51, 2005.

[209] F. Kleitz, S. H. Choi, and R. Ryoo, "Cubic Ia3d large mesoporous silica: synthesis and replication to platinum nanowires, carbon nanorods and carbon nanotubes.," *Chem. Commun. (Camb.)*, no. 17, pp. 2136–7, 2003.

[210] M. Pourkhalil, N. Izadi, A. Rashidi, and M. Mohammad-Taheri, "Synthesis of CeOx/γ-Al 2 O 3 catalyst for the NH 3-SCR of NOx," *Materials Research Bulletin*, 2017.

[211] A. J. F. Carrión, "Disilicatos de tierras raras simples y sus soluciones sólidas: Estructura cristalina y propiedades f'\isicas," 2014.

[212] T. Montini, M. Melchionna, M. Monai, and P. Fornasiero, "Fundamentals and catalytic applications of CeO2-based materials," *Chemical reviews*, vol. 116, no. 10, pp. 5987–6041, 2016.

[213] V. H. Vu, J. Belkouch, A. Ould-Dris, and B. Taouk, "Catalytic oxidation of volatile organic compounds on manganese and copper oxides supported on titania," *AIChE journal*, vol. 54, no. 6, pp. 1585–1591, 2008.

[214] K. Leistner, F. Brüsewitz, K. Wijayanti, A. Kumar, K. Kamasamudram, and L. Olsson, "Impact of Copper Loading on NH3-Selective Catalytic Reduction, Oxidation Reactions and N2O Formation over Cu/SAPO-34," *Energies*, vol. 10, no. 4, p. 489, 2017.

[215] L. Szabova, M. F. Camellone, and M. Huang, "Thermodynamic, electronic and structural properties of Cu/CeO2 surfaces and interfaces from first-principles DFT+ U calculations," *The Journal of chemical physics*, vol. 133, no. 23, p. 234705, 2010.

[216] P. Bera, K. Priolkar, P. Sarode, M. Hegde, S. Emura, R. Kumashiro, and N. Lalla, "Structural Investigation of Combustion Synthesized Cu/CeO2 Catalysts by EXAFS and Other Physical Techniques: Formation of a Ce1-x Cu x O2-

δ Solid Solution," *Chemistry of Materials*, vol. 14, no. 8, pp. 3591–3601, 2002.

[217] J. D. Epping and B. F. Chmelka, "Nucleation and growth of zeolites and inorganic mesoporous solids: Molecular insights from magnetic resonance spectroscopy," *Current opinion in colloid \& interface science*, vol. 11, no. 2, pp. 81–117, 2006.

[218] T. C. Brüggemann, D. G. Vlachos, and F. J. Keil, "Microkinetic modeling of the fast selective catalytic reduction of nitrogen oxide with ammonia on H-ZSM5 based on first principles," *Journal of catalysis*, vol. 283, no. 2, pp. 178–191, 2011.

[219] M. P. Ruggeri, T. Selleri, M. Colombo, I. Nova, and E. Tronconi, "Investigation of NO 2 and NO interaction with an Fe-ZSM-5 catalyst by transient response methods and chemical trapping techniques," *Journal of Catalysis*, vol. 328, pp. 258–269, 2015.

[220] A. Infantes-Molina, L. Righini, L. Castoldi, C. Loricera, J. Fierro, A. Sin, and L. Lietti, "Characterization and reactivity of Ce-promoted PtBa lean NO x trap catalysts," *Catalysis today*, vol. 197, no. 1, pp. 178–189, 2012.

[221] P. Forzatti, L. Lietti, and L. Castoldi, "Storage and Reduction of NO x Over LNT Catalysts," *Catalysis Letters*, vol. 145, no. 2, pp. 483–504, 2015.

[222] F. Lin, X. Wu, and D. Weng, "Effect of barium loading on CuO x-CeO 2 catalysts: NO x storage capacity, NO oxidation ability and soot oxidation activity," *Catalysis today*, vol. 175, no. 1, pp. 124–132, 2011.

[223] L. Zhang, J. Pierce, V. L. Leung, D. Wang, and W. S. Epling, "Characterization of Ceria's Interaction with NO x and NH3," *The Journal of Physical Chemistry C*, vol. 117, no. 16, pp. 8282–8289, 2013.

[224] B. M. Shakya, M. P. Harold, and V. Balakotaiah, "Modeling and analysis of dual-layer NOx storage and reduction and selective catalytic reduction monolithic catalyst," *Chemical Engineering Journal*, vol. 237, pp. 109–122, 2014.

[225] L. Xuesong, W. Xiaodong, W. Duan, and S. Lei, "Modification of Cu/ZSM-5 catalyst with CeO 2 for selective catalytic reduction of NO x with ammonia," *Journal of Rare Earths*, vol. 34, no. 10, pp. 1004–1009, 2016.

[226] H. Pan, Y. Guo, and H. T. Bi, "NOx adsorption and reduction with C 3 H 6 over Fe/zeolite catalysts: Effect of catalyst support," *Chemical Engineering Journal*, vol. 280, pp. 66–73, 2015.

[227] F. Gao, J. H. Kwak, J. Szanyi, and C. H. Peden, "Current understanding of Cu-exchanged chabazite molecular sieves for use as commercial diesel engine

DeNO x catalysts," *Topics in Catalysis*, vol. 56, no. 15–17, pp. 1441–1459, 2013.

[228] U. Deka, I. Lezcano-Gonzalez, B. M. Weckhuysen, and A. M. Beale, "Local environment and nature of Cu active sites in zeolite-based catalysts for the selective catalytic reduction of NO x," *ACS catalysis*, vol. 3, no. 3, pp. 413–427, 2013.

[229] S. Stoll and A. Schweiger, "EasySpin, a comprehensive software package for spectral simulation and analysis in EPR," *Journal of magnetic resonance*, vol. 178, no. 1, pp. 42–55, 2006.

[230] A. Godiksen, F. N. Stappen, P. N. Vennestrøm, F. Giordanino, S. B. Rasmussen, L. F. Lundegaard, and S. Mossin, "Coordination environment of copper sites in Cu-CHA zeolite investigated by electron paramagnetic resonance," *The Journal of Physical Chemistry C*, vol. 118, no. 40, pp. 23126–23138, 2014.

[231] S. C. Larsen, A. Aylor, A. T. Bell, and J. A. Reimer, "Electron paramagnetic resonance studies of copper ion-exchanged ZSM-5," *The Journal of Physical Chemistry*, vol. 98, no. 44, pp. 11533–11540, 1994.

[232] J. Chen, Y. Zhan, J. Zhu, C. Chen, X. Lin, and Q. Zheng, "The synergetic mechanism between copper species and ceria in NO abatement over Cu/CeO2 catalysts," *Applied Catalysis A: General*, vol. 377, no. 1–2, pp. 121–127, 2010.

[233] A. Mart\inez-Arias, M. Fernández-Garc\ia, J. Soria, and J. Conesa, "Spectroscopic study of a Cu/CeO2catalyst subjected to redox treatments in carbon monoxide and oxygen," *Journal of Catalysis*, vol. 182, no. 2, pp. 367–377, 1999.

[234] P. G. Harrison, I. K. Ball, W. Azelee, W. Daniell, and D. Goldfarb, "Nature and surface redox properties of copper (II)-promoted cerium (IV) oxide CO-oxidation catalysts," *Chemistry of materials*, vol. 12, no. 12, pp. 3715–3725, 2000.

[235] A. Mart'\inez-Arias, R. Cataluña, J. C. Conesa, and J. Soria, "Effect of copper-ceria interactions on copper reduction in a Cu/CeO2/Al2O3 catalyst subjected to thermal treatments in CO," *The Journal of Physical Chemistry B*, vol. 102, no. 5, pp. 809–817, 1998.

[236] M. Chiesa, M. C. Paganini, S. Livraghi, and E. Giamello, "Charge trapping in TiO2 polymorphs as seen by Electron Paramagnetic Resonance spectroscopy.," *Phys Chem Phys*, vol. 15, no. 24, pp. 9435–47, 2013.

[237] Y. Xiong, L. Li, L. Zhang, Y. Cao, S. Yu, C. Tang, and L. Dong, "Migration of copper species in Ce x Cu 1- x O 2 catalyst driven by thermal treatment and the effect on CO oxidation," *Physical Chemistry Chemical Physics*, vol. 19, no.

32, pp. 21840–21847, 2017.

[238] M. Moreno-González, B. Hueso, M. Boronat, T. Blasco, and A. Corma, "Ammonia-Containing Species Formed in Cu-Chabazite As Per In Situ EPR, Solid-State NMR, and DFT Calculations," *The journal of physical chemistry letters*, vol. 6, no. 6, pp. 1011–1017, 2015.

[239] Z. Qu, Z. Wang, X. Zhang, and H. Wang, "Role of different coordinated Cu and reactive oxygen species on the highly active Cu-Ce-Zr mixed oxides in NH 3-SCO: a combined in situ EPR and O 2-TPD approach," *Catalysis Science \& Technology*, vol. 6, no. 12, pp. 4491–4502, 2016.

[240] T. Yu, T. Hao, D. Fan, J. Wang, M. Shen, and W. Li, "Recent NH3-SCR Mechanism Research over Cu/SAPO-34 Catalyst," *The Journal of Physical Chemistry C*, vol. 118, no. 13, pp. 6565–6575, 2014.

[241] A. Mart'\inez-Arias, A. Hungr'\ia, A. Iglesias-Juez, M. Fernández-Garc'\ia, J. Anderson, J. Conesa, G. Munuera, and J. Soria, "Redox and catalytic properties of CuO/CeO2 under CO+ O2+ NO: Promoting effect of NO on CO oxidation," *Catalysis today*, vol. 180, no. 1, pp. 81–87, 2012.

[242] C. Liang, X. Li, Z. Qu, M. Tade, and S. Liu, "The role of copper species on Cu/γ-Al2O3 catalysts for NH3-SCO reaction," *Applied Surface Science*, vol. 258, no. 8, pp. 3738–3743, 2012.

[243] A. Beale, J. Hoffman, M. Sankar, E. Schrojenstein-Lantman, and B. Weckhuysen, "Heterogeneous Catalysts for Clean Technology," 2013.

[244] G. MacZura, "Aluminum Oxide (Alumina), Calcined, Tabular, and Aluminate Cements," *Kirk-Othmer Encyclopedia of Chemical Technology*, 2000.

[245] A. R. Ferreira, E. Küçükbenli, A. A. Leitão, and S. de Gironcoli, "Ab initio 27 Al NMR chemical shifts and quadrupolar parameters for Al 2 O 3 phases and their precursors," *Physical Review B*, vol. 84, no. 23, p. 235119, 2011.

[246] X. Zhou, L. Li, Z. Li, L. Fan, W. Kang, and B. Cheng, "The preparation of continuous CeO2/CuO/Al2O3 ultrafine fibers by electro-blowing spinning (EBS) and its photocatalytic activity," *Journal of Materials Science: Materials in Electronics*, pp. 1–11, 2017.

[247] Q. Ye, L. Wang, and R. T. Yang, "Activity, propene poisoning resistance and hydrothermal stability of copper exchanged chabazite-like zeolite catalysts for SCR of NO with ammonia in comparison to Cu/ZSM-5," *Applied Catalysis A: General*, vol. 427, pp. 24–34, 2012.

[248] M. Bediako, S. Gawu, A. Adjaottor, and J. S. Ankrah, "Early and late strength characterization of Portland cement containing calcined low-grade kaolin clay,"

Journal of Engineering, vol. 2016, 2016.

[249] K. Kanehashi and J. F. Stebbins, "In situ high temperature 27Al NMR study of structure and dynamics in a calcium aluminosilicate glass and melt," *Journal of Non-Crystalline Solids*, vol. 353, no. 44–46, pp. 4001–4010, 2007.

[250] T. Yokoi, H. Mochizuki, S. Namba, J. N. Kondo, and T. Tatsumi, "Control of the Al Distribution in the Framework of ZSM-5 Zeolite and Its Evaluation by Solid-State NMR Technique and Catalytic Properties," *The Journal of Physical Chemistry C*, vol. 119, no. 27, pp. 15303–15315, 2015.

[251] J. D. Albarracin-Caballero, I. Khurana, J. R. Di Iorio, A. J. Shih, J. Schmidt, M. Dusselier, M. E. Davis, A. Yezerets, J. T. Miller, F. Ribeiro, and others, "Structural and Kinetic Changes to Small-Pore Cu-Zeolites After Hydrothermal Aging Treatments and Selective Catalytic Reduction of NOx with Ammonia," *Reaction Chemistry \& Engineering*, 2016.

[252] I. A. Kasyanov, A. A. Maerle, I. I. Ivanova, and V. I. Zaikovskii, "Towards understanding of the mechanism of stepwise zeolite recrystallization into micro/mesoporous materials," *Journal of Materials Chemistry A*, vol. 2, no. 40, pp. 16978–16988, 2014.

[253] T. A. Nijhuis, A. E. Beers, T. Vergunst, I. Hoek, F. Kapteijn, and J. A. Moulijn, "Preparation of monolithic catalysts," *Catalysis Reviews*, vol. 43, no. 4, pp. 345–380, 2001.

[254] H. Bouwmeester and A. Burggraff, "Fundamentals of Inorganic Membrane Science and Technology," 1996.

9   Annex

9.1   Support material

The properties of the support material are defined in accordance to the requirements of the filter.

Table 9-1. Chemical composition

Composite	Content %	Analysis method
SiO_2	70 - 75	DIN EN ISO 26845
Na_2O	10 - 15	DIN EN ISO 12677
CaO	7 - 11	
Al_2O_3	0,5 - 5	
MgO	0 - 5	
K_2O	0 - 4	
Ignition Loss	0,2	

9.2 Biofuel composition

TECOSOL

liquid organic energy

Tecosol GmbH

Verwaltung:		Jahrstr. 97199 Ochsenfu
Telefon:		09331 / 98 15
Werk:		Marktbreiter Str. 7 97199 Ochsenfu
Telefon:		09331 / 87 61 -
Telefax:		09331 / 87 61-1
Geschäftsführer:		Michael Long Dr. Ralf Türo
Registergericht:		AG Würzbur HRB 1001
Sitz der Gesellschaft:		Ochsenfu
Ust-IdNr.:		DE 24584618

Analysenzertifikat

Produkt:	Campa-Biodiesel gemäß DIN EN 14214
Verladetank:	B0256
Chargennummer:	0777-28072015
Probenahmedatum:	27.07.2015
Verladenummer:	10777-114064
Verladedatum:	28.07.2015
Kunde:	Fraunhofer Institut für Umweltsicherheit & Energietechnik

Generell anwendbare Anforderungen und Testmethoden DIN EN 14214:2012

Qualitätsparameter	Einheit	Istwert	Grenzwert	Prüfverfahren
Ester-Gehalt	% (m/m)	98,4	min. 96,5	DIN EN 14103
Dichte bei 15 °C	kg/m³	883,0	860 - 900	DIN EN ISO 3675
Kinematische Viskosität bei 40 °C	mm²/s	4,510	3,50 - 5,00	DIN EN ISO 3104
Flammpunkt	°C	183	min. 101	DIN EN ISO 3679
CFPP (Grenze der Filtrierbarkeit)	°C	-10	max. -10	DIN EN 116
Cloudpoint	°C	-4	max. -3	EN 23015
Schwefelgehalt	mg/kg	7,7	max. 10,0	DIN EN ISO 20884
Cetanzahl	-	54,4	min. 51,0	DIN EN ISO 5165
Asche-Gehalt (Sulfatasche)	% (m/m)	<0,01	max. 0,02	ISO 3987
Wassergehalt	mg/kg	181	max. 500	DIN EN ISO 12937
Gesamtverschmutzung	mg/kg	9	max. 24	DIN EN 12662
Korrosionswirkung auf Kupfer (3 h bei 50 °C)	Korrosionsgrad	1	Klasse 1	DIN EN ISO 2160
Oxidationsstabilität, 110 °C	Stunden	11,3	min. 8,0	DIN EN 14112
Säurezahl	mg KOH/g	0,256	max. 0,500	DIN EN 14104
Iodzahl	g Iod/100g	112	max. 120	DIN EN 14111
Gehalt an Linolensäure-Methylester	% (m/m)	9,3	max. 12,0	DIN EN 14103
Gehalt an mehrfach ungesättigten Methylestern (4 oder mehr Doppelbindungen)	% (m/m)	<1	max. 1	DIN EN 14103
Methanolgehalt	% (m/m)	0,02	max. 0,20	DIN EN 14110
Monoglycerid-Gehalt	% (m/m)	0,41	max. 0,70	DIN EN 14105
Diglycerid-Gehalt	% (m/m)	0,16	max. 0,20	DIN EN 14105
Triglycerid-Gehalt	% (m/m)	0,09	max. 0,20	DIN EN 14105
Gehalt an freiem Glycerin	% (m/m)	0,015	max. 0,020	DIN EN 14105
Gehalt an Gesamt-Glycerin	% (m/m)	0,15	max. 0,25	DIN EN 14105
Gehalt an Alkali-Metallen (Na + K)	mg/kg	0,8	max. 5,0	DIN EN 14538
Gehalt an Erdalkali-Metallen (Ca + Mg)	mg/kg	0,2	max. 5,0	DIN EN 14538
Phosphor-Gehalt	mg/kg	0,4	max. 4,0	DIN EN 14107

Figure 9-1. Biofuel Specifications.
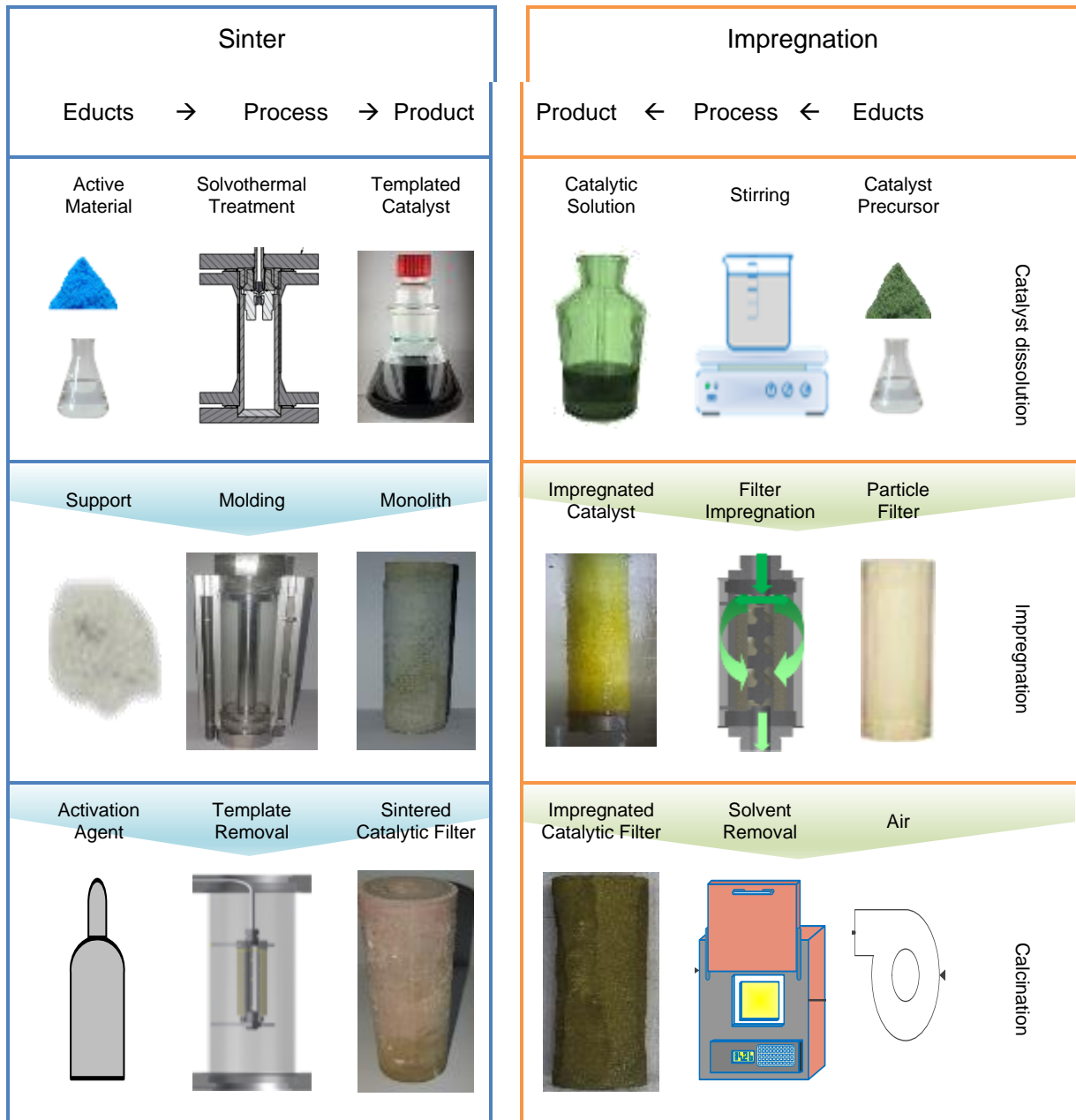
9.3   Comparison of catalyst synthesis

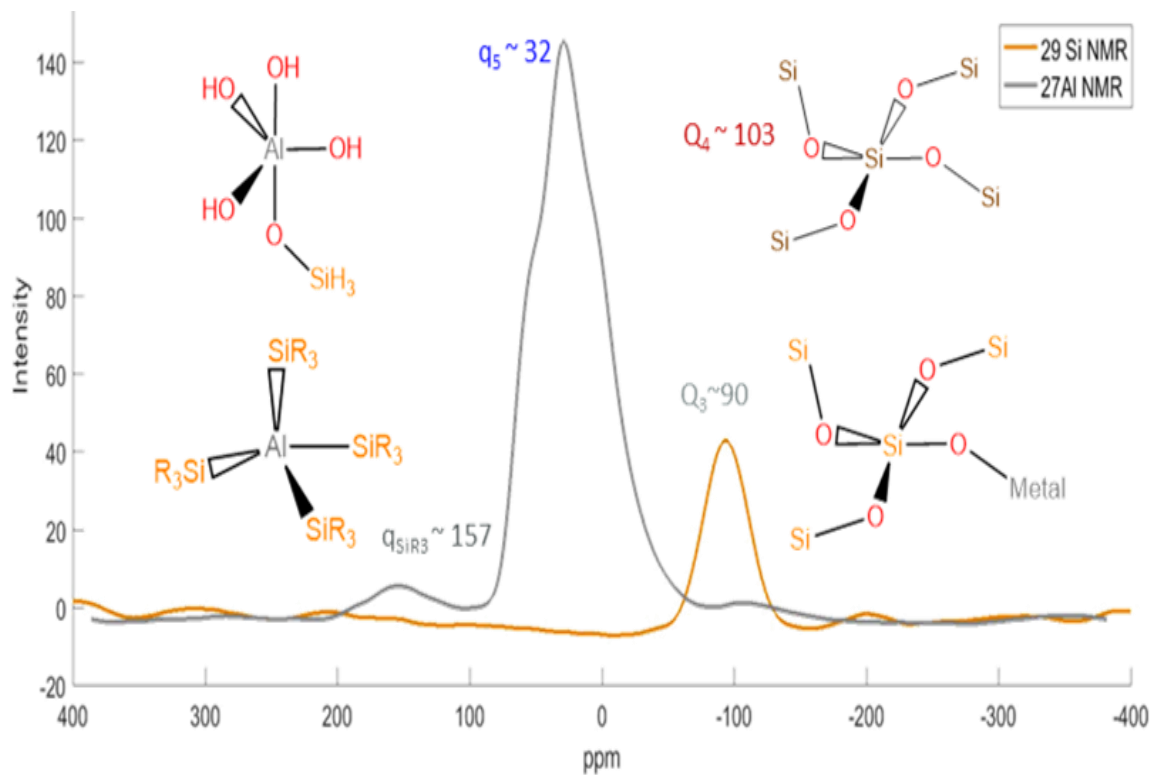Figure 9-2. Comparison of impregnation and sintering fabrication process.

9.4 ^{27}Al and ^{29}Si NMR analysis

Figure 9-3. *^{29}Si and ^{27}Al NMR of the catalytical filter.*